Modelling and development of a resonator-based noise mitigation system

Yaxi Peng

Master of Science Thesis

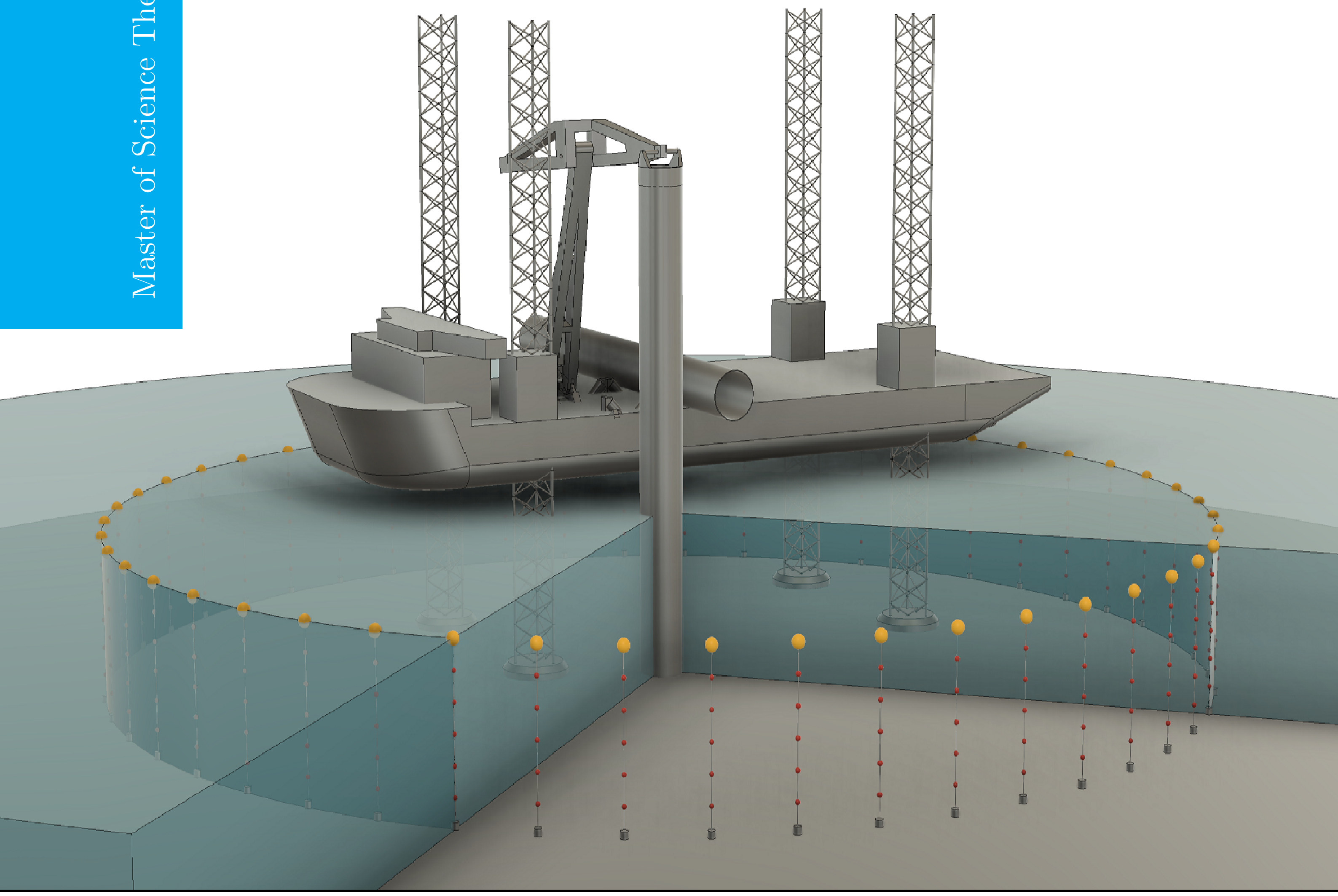

Offshore and Dredging Engineering

Modelling and development of a resonator-based noise mitigation system

MASTER OF SCIENCE THESIS

For the degree of Master of Science in Offshore and Dredging
Engineering at Delft University of Technology
to be defended publicly on Tuesday October 17, 2017.

Yaxi Peng

Supervisor: Dr.ir. A. Tsouvalas
Committee chairman: Prof.dr. A.V. Metrikine

Thesis committee:
Prof.dr. A.V. Metrikine
Dr.ir. A. Tsouvalas
Dr.ir. K.N. van Dalen
Ir. E. Belderbos

Faculty of Mechanical, Maritime and Materials Engineering (3mE) · Delft University of Technology

The work in this thesis was supported by Seastate5. Their cooperation is hereby gratefully acknowledged.

Abstract

Anthropogenic underwater noise generated by pile driving has been an issue of serious concern for a long period of time. The underwater noise pollution from pile driving could pose a threat to marine mammals. To reduce the low-frequency noise, many offshore companies develop various treatments and alternatives for pile driving. In this study, the focus is placed on a resonator-based noise mitigation technique.

The first part of the thesis focuses on the investigation of the existing resonator-based noise mitigation systems. A mathematical expression for the resonance frequency of an individual open-ended resonator is derived. To validate this expression, a finite element model is built in COMSOL. To compare the acoustic performance with the HSD, a finite element model is also built for the HSD mitigation system. To describe the acoustic performance of the resonators for generic use, the frequency response function of an open-ended resonator is analytically derived based on the assumption that the resonator behaves as a linear SDoF system. The derivation of the parameters of the equivalent SDoF system representing each individual resonator is based on appropriate fitting of numerical results obtained in COMSOL.

The second part of the thesis deals with the development of a new design of a resonator system named *Qiu*. To install the resonator system in a more flexible way, the air is encapsulated in the resonator. A finite element model is also developed in COMSOL for the *Qiu* resonator.

In the last part of the thesis, a three-dimensional vibroacoustic model is developed in order to find the optimal properties of the underwater resonator and to improve the existing noise mitigation techniques. The model requires the proper description of the noise source, the resonator and the acoustic waveguide. The normal mode method is used to compose the Green's function of the waveguide. The boundary element method is then employed in order to obtain the total pressure field. The frequency response functions derived in the first part of the thesis are subsequently used to describe the acoustic behaviour of the resonators. A parametric study is presented in order to define the principal factors for effective noise mitigation. In addition, the several cases are investigated in order to obtain the optimal properties of the resonator and the optimum configuration of the array of resonators surrounding the sound source to maximise noise reduction.

Table of Contents

List of Figures

List of Tables

Preface

This graduation project, titled ”Modelling and development of a resonator-based noise mitigation system for pile driving”, is proposed and supported by both Seastate5 and the Delft University of Technology. The thesis aims to fulfill the graduation requirements for the Master degree in Offshore and Dredging Engineering at the Delft University of Technology.

I would like to take this opportunity to thank the people who support me during this process. First, I would like to thank my company supervisor, Edward Belderbos. You always encourage me and support my different ideas from the very beginning to the end of this project. You are always positive and patiently lead me to the right direction whenever I have doubts. I benefit a lot from every meeting and conversation with you.

Secondly, I would like to thank my university supervisor, Apostolos Tsouvalas. Every meeting with you is so inspiring and very pleasant. Thank you for introducing me to this underwater acoustics world. This is such an interesting research field and is worthwhile for further study. Through this graduation project, I learned a lot of new knowledge from you and gained the insight of many fundamental physical phenomena.

I also would like to thank Prof. Metrikine for your guidance through the project. You always look into details and point out where the problem comes from. Through every meeting, I can receive many feedbacks from both you and Apostolos, which give me a new insight for solving the problem.

I also want to thank Willem for providing me this great opportunity to work on such a wonderful project. You are so creative and productive on many projects. The working experience in Seastate5 is unique for me, where I met so many intelligent and creative people. Thank you, Marco, for your company over the past year in Seastate5. Thank you, Jeroen, for together working on this interesting resonator project.

In the end, I would like to give the deepest thanks to my parents and friends. My parents always support and encourage me through these two years across the distance. Thank my boyfriend, Rui. Whenever I need you, you will always be there. Thank all my friends for supporting me.

I hope when you read this thesis, you could find something useful and interesting, that would be my best pleasure.

Delft, University of Technology Yaxi Peng
to be defended publicly on Tuesday October 17, 2017.

”Dedicated to my parents, Chunxia Liu and Fei Peng.”
— *Yaxi Peng*

Chapter 1

Introduction

1.1 Problem statement and motivations

Anthropogenic noise from offshore pile driving has become a serious issue for the marine environment. With the growing demand for renewable energy, the construction work of offshore wind farms tends to have a larger scale by using foundation piles with larger diameters. When driving these large foundation piles into the soil, a great deal of noise could be radiated from the pile-water and pile-soil interface at low acoustic frequencies, i.e. usually below 400 Hz. The underwater noise pollution generated by this percussive piling threatens marine mammals, especially the low-frequency noises, which could severely interfere with their foraging and migrating behaviour, and damage their hearing [9, 10].

In the light of the significant research on noise propagation and noise prediction, the mitigation of the underwater noise could be achieved in the following two ways; either control the noise at the source or block the noise transmission path. Many offshore companies provide various treatment and alternatives to pile driving. Based on the primary noise path in the water region, several noise mitigation techniques have been developed. By forming a freely rising bubble curtain around the pile, a significant impedance mismatch can be created so that the radiated sound waves are reflected, refracted and scattered along the interface between two mediums leading to noise reduction. A sound reduction prediction model with the use of Air Bubble Curtain (ABC) was proposed earlier by Tsouvalas and Metrikine [11]. Whereas the resonance of individual bubbles [12, 13] stimulated by the sound waves do not contribute to the absorption of the energy. This is due to the resonance frequencies of free individual bubbles are usually above 1 kHz, which is out of the target frequency range in most practical cases. The degree of contribution of each mechanism, i.e. reflection or absorption, to the final noise reduction depends on the frequency content of the radiated sound in relation to the size of the released air-bubbles in the mixture. By using nets of air-filled balloons and PE-foam elements, the Hydro-Sound Damper (HSD) can absorb the energy through the resonance of balloons, dissipation and material damping of foam elements [14]. The open-ended resonator is another promising way to mitigate the noise. It works in the same way as Helmholtz resonators, since the encapsulated air can undergo driven oscillations and the sound can be re-radiated from the air-water interface at the opening [6].

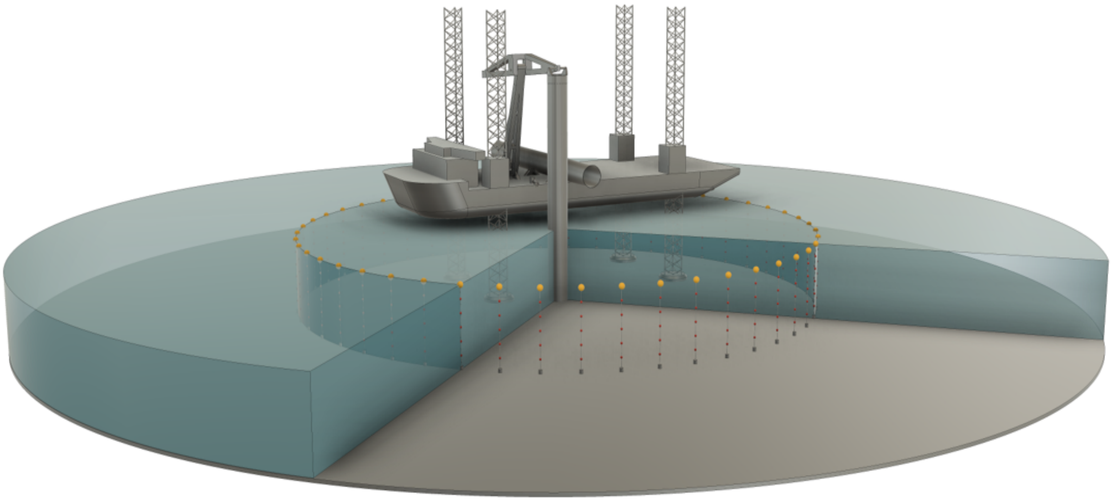

Figure 1.1: The resonator-based noise mitigation system

Besides the approaches, in this study, a new resonator-based noise mitigation technique is proposed capable of effectively blocking the primary noise path in water region, as shown in Figure 1.1.

1.2 Scope of the study and research questions

To answer this central research question: **how to mitigate the noise from pile driving by using an underwater resonator system?** There are a series of objectives and research steps need to be taken.

In the light of the noise mitigation techniques developed by offshore practitioners, the first objective is to investigate the principle mechanism of the underwater resonators. This goal can be achieved by answering the following sub-questions:

1. How does a free air bubble, an encapsulated air bubble and an open-ended resonator attenuate the sound?
2. How to determine the resonance frequency from the underwater resonator?
3. What are the advantages and disadvantages of the current noise mitigation techniques?
4. In what aspect can we improve the design of marine resonators?

The next step is to propose a new design and implement it in a finite element model (COMSOL Multiphysics). By answering the following questions, we will be able to achieve the second objective:

1. How to tune the new resonator to the target resonant frequency?
2. What type of the material we prefer to use for the resonator?
3. What is the response of the resonator in frequency domain?

Then, a critical step is to develop a 3-D acoustically coupled model for the prediction of noise reduction by the resonator-based noise mitigation system. To obtain this objective, we have the following question:

1. How to describe the sound source?
2. How to determine the frequency response of the resonator?
3. How to couple the resonators into the field containing the noise source?
4. What are the critical parameters for the design of a resonator-based noise mitigation system?

Finally, the objective that cannot be neglected is to provide recommendations for the future development of the model and advice for the offshore practitioners.

1. How to improve the acoustically coupled model?
2. How to describe the behaviour of the resonator more precisely?
3. How to improve the design of noise mitigation system?
4. What are the other application extensions that can be applied to the present model?

1.3 Thesis outline

This study first aims to propose a new type of resonator for mitigating underwater noise and develop a finite element underwater acoustic model for a single resonator.

In Chapter 2, the state of art in noise mitigation techniques is introduced to have a solid theoretical background for this study. The main mechanisms behind a free air bubble curtain, an encapsulated air bubble and the open-end resonators are investigated. The strength and drawbacks of those noise reduction systems are analysed.

In Chapter 3, the underlying physics of the noise reduction by the application of the open-ended resonator is investigated into depth. The theory of the resonance frequency for the underwater open-ended resonator is presented. Also, a finite-element model in COMSOL Multiphysics is developed for the open-ended resonator, which is used to validate the theory of the resonant frequency of this new type of resonators. A parametric study for the open-ended resonator and the encapsulated air bubble was conducted to find the optimum configuration for the targeted frequency range. The frequency response functions are derived analytically for the various open-ended resonators. The derivation is based on appropriate fitting of numerical results obtained in COMSOL. This could provide us the acoustic performance of the individual resonator for the construction of the analytical model in Chapter 6.

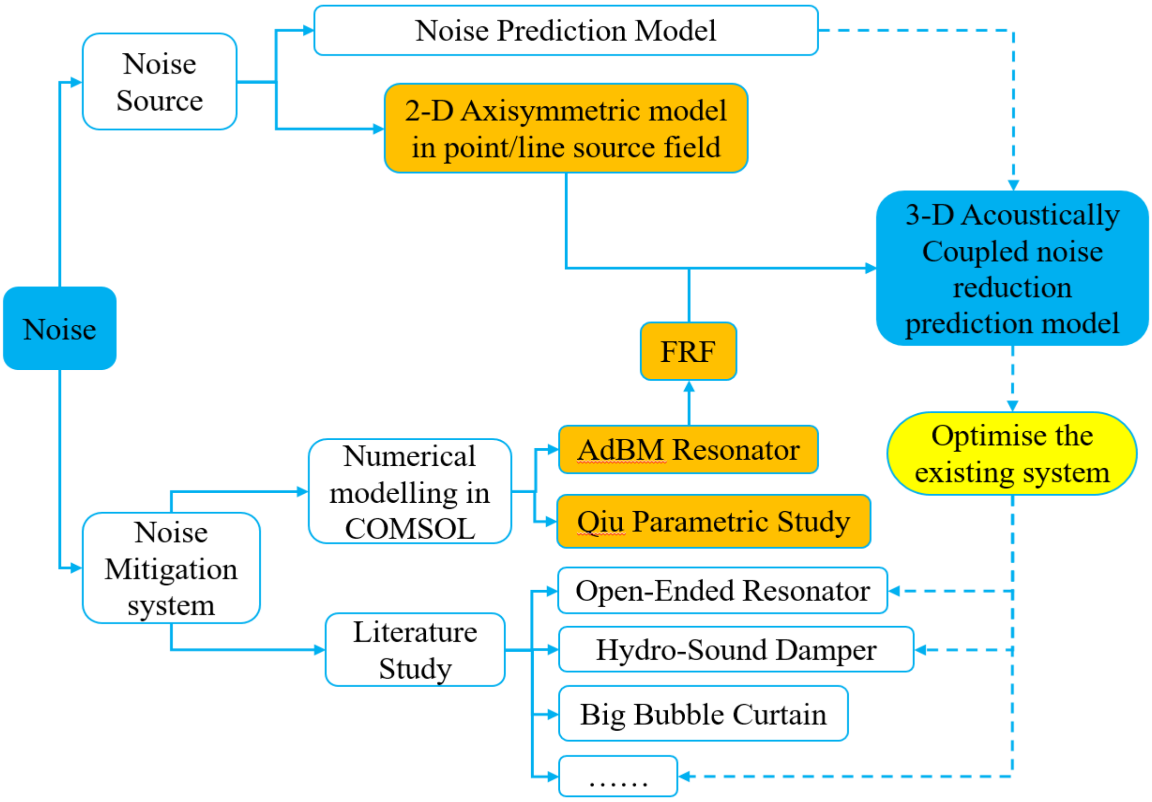

Figure 1.2: The thesis structure

In Chapter 4, a new design of resonator, named *Qiu* is proposed, and a finite element model is developed for the prediction of the effective noise reduction. The acoustic performance of the *Qiu* resonator is investigated by using software package COMSOL. Subsequently, the noise reduction for varying opening radius of the *Qiu* resonator is analysed.

In Chapter 5, a 2-D axisymmetric sound propagation model is developed for the well-known benchmark case for the field containing a point source and a line source, respectively. The derivation of the Green's function and the boundary conditions are presented. The solutions are verified through a finite-element model in COMSOL Multiphysics, which is based on the same configuration of the domain.

In Chapter 6, a 3-D acoustically coupled model for the prediction of the noise reduction by the application of a resonator-base noise mitigation system is developed. In this model, a monopole point source is used for the noise source. At this stage, we assume that the frequency response function of the resonators is given by the underwater open-ended resonator.

In Chapter 7, a parametric study based on the 3-D noise reduction prediction model is presented for the individual resonator and the arrays of resonators. This study provides insight on the determination of the optimal parameters for the design of the system.

In Chapter 8, the application of the 3-D noise reduction model is presented for several cases. Finally, in Chapter 9, the conclusion of findings and the recommendations from the academic and the industrial point of view are summarised. Also, the remaining challenges for the future development of noise mitigation techniques are discussed.

Chapter 2

The state of the art in noise mitigation

As we discussed in Chapter 1, the underlying physics of the noise generation from pile driving and various noise reduction techniques provide the basis for the further investigation in this thesis. Therefore, the theme of this chapter will focus on the noise radiated from pile driving and noise mitigation techniques. In the first section, the principal mechanism of noise generated from impact hammering are discussed and several noise prediction models for offshore pile driving are presented. In the second section, the main mechanism of present noise mitigation systems is analysed. The advantages and limits of individual noise abatement techniques are discussed. In addition, some recommendations are proposed by the author.

2.1 Underwater noise from offshore piling

On the background of increasing demand for the construction of large-scale offshore wind farms (OWF), anthropogenic noise emission has been a serious issue urgent for solutions. The tremendous investigations for the mechanism of underwater noise from offshore pile driving have been achieved in recent years. Due to the complexity of the shallow water environment, i.e. scattering at the sea surface, reflections, refractions and the influence of the soil conditions, the sound wave propagation in shallow water has always been a challenging topic. In addition, the investigation of offshore pile driving requires a reliable description incorporating the interactions between three mediums, pile, water and soil. This increases the complexity to the problem even further.

In 2011, a numerical model for the prediction of underwater noise generated by impact pile driving was developed by Reinhall and Dahl [1]. The model was created by using FE technique in COMSOL Multiphysics and was simulated in an axisymmetric shallow water waveguide. Both water and sediment were described as linear acoustic fluids in this study. In addition, to save the computational effort for the prediction of sound propagation in the far-field, a parabolic equation model was also developed.

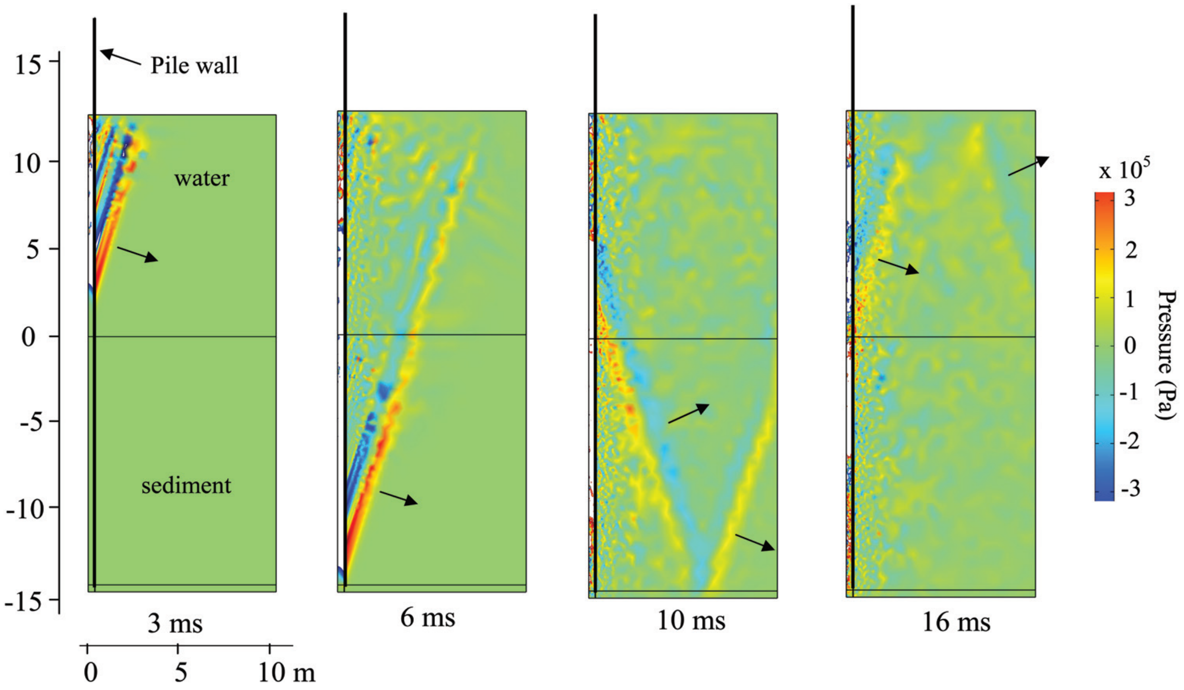

Figure 2.1: Sould radiation process from the pile simulated by Reinhall and Dahl [1]: the graphs are after 3,6,10 and 16 ms after the hammering.

This study has shown that the dominant underwater noise from pile driving is due to radially expanding wavefronts caused by the radial displacement motion of the pile in the form of a *Mach cone* in the water and sediment region. Following the hammer strike at the top of the pile, the waves move down to the bottom of the pile at a supersonic speed around 5015 m/s. Subsequently, the waves are reflected upwards after reaching the tip of the pile. The acoustic radiation of the sound is shown in Figure 2.1 [1] at a series of time after impact hammering.

Based on the research method introduced by Reinhall and Dahl [1], many investigations of noise prediction by offshore pile driving have done in recent years. Although the noise prediction model mentioned above could simulate the water region with proper acoustic properties, the acoustic description of the soil region is not always justified. To predict the underwater noise for a more generic system, a linear semi-analytical model for the prediction of the underwater noise from offshore pile driving was introduced by Tsouvalas and Metrikine [15]. It is worth to mention that the seabed is modeled as springs and dashpots in all directions, which requires an accurate estimation of the equivalent spring and dashpot coefficients for the soil.

Following on the model above, Tsouvalas and Metrikine continued their investigation with a three dimensional pile-water-soil interaction model to provide a more generic description of the soil region by using only basic soil properties, as shown in Figure 2.2 [2]. In the new model, the soil is described as a three dimensional elastic continuum. Based on the validation by offshore measurements, the results of the study show that the model can achieve a reliable prediction of the sound pressure level in the fluid and the vibration in the sediment. Scholte waves are found to be generated in the vicinity of the seabed-water interface which carry energy in the low-frequency range.

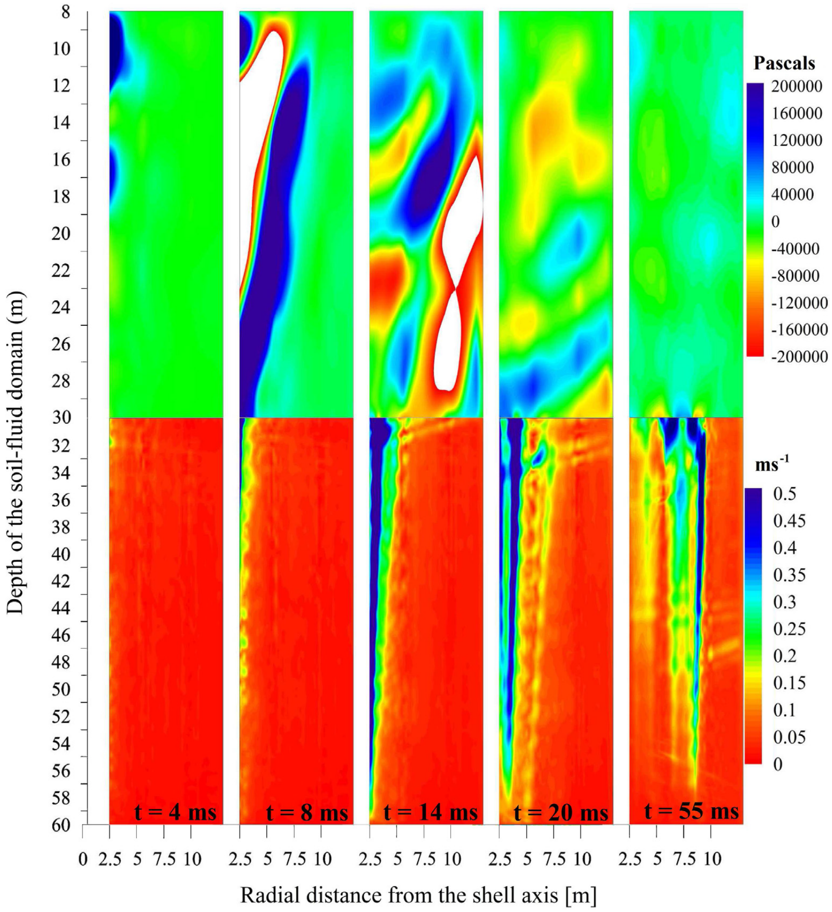

Figure 2.2: Sould radiation process from a pile with a dsameter of 5 m and a soil with $E_s = 100MPa$ simulated by Tsouvalas and Metrikine [2]: the graphs are after 4, 8, 14, 20 and 55 ms after the hammering.

The above-discussed findings provide the solid understanding of the underlying physics of the underwater noise from impact pile driving. The results from these studies could help us, in a large extent, design more efficient noise mitigation systems. This is what this thesis aims to achieve.

2.2 Underwater noise mitigation

Following the discussions in the last section, it is important first to understand the underlying physics of how the acoustic energy from a noise source can be radiated into the underwater environment. With the knowledge of the noise generation mechanism by offshore pile driving, we realize that there are two principal ways to mitigate underwater noise. One is to control the sound generation at the noise source, and the other is to block the primary sound transmission path in the water region.

To mitigate the noise at the source, there are multiple alternatives for the traditional hammer, i.e. vibratory piling and blue piling. Typical radiation patterns resulting from vibratory

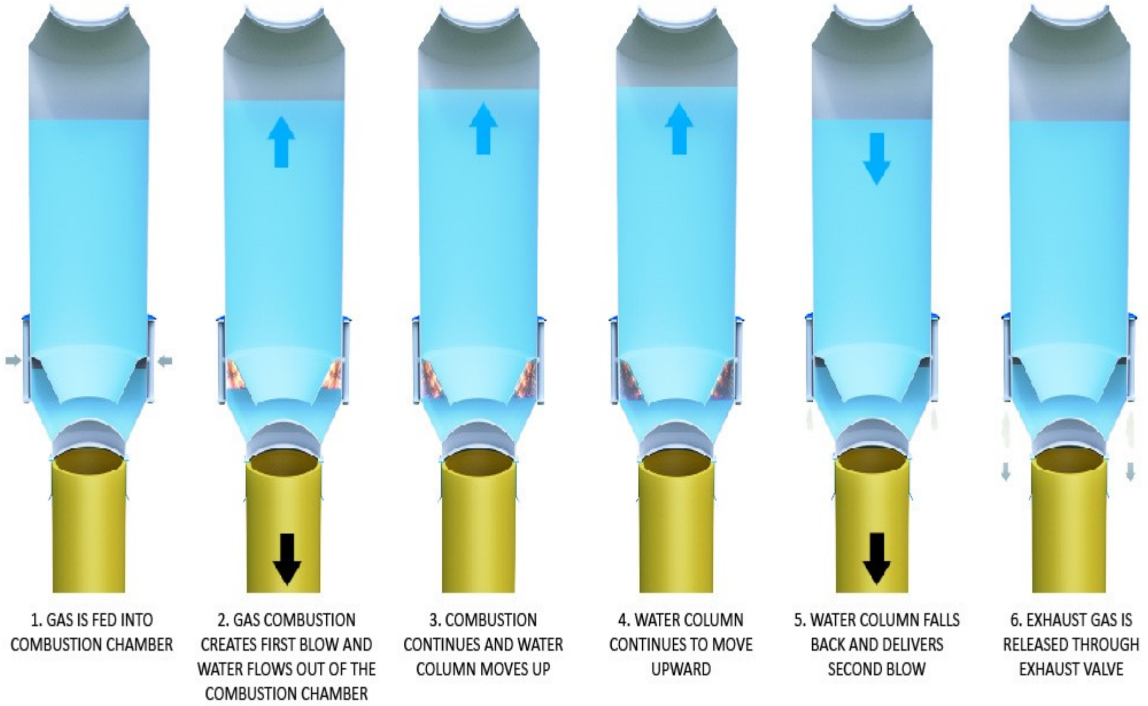

Figure 2.3: Fistuca BV: Undergoing different phases of the piling cycle

hammering are introduced by Tsouvalas and Metrikine [16]. The Blue Piling technology was developed by Fistuca BV aiming to achieve silent installation without the use of a noise mitigation system. Being different from the conventional hammers, a large water column is used to drive the pile into the soil. A gas combustion could effectively drive the water column up and fall automatically given the force of gravity. The detailed process of the working mechanism is shown in the Figure 2.3. In addition, the control of the sound at the source can be achieved by modifying the duration of the impact.

The second critical method is by blocking the primary noise path in the water region. This study aims to achieve the noise reduction based on this principal method. In the remaining part of this section, we are going to analyse the following noise mitigation techniques: (1) the air bubble curtain; (2) the noise mitigation screen; (3) the hydro-sound damper system; (4) the open-ended resonator system.

The *secondary sound path* at the seabed-water interface [2] is through Scholte waves carrying significant acoustic energy in the low frequencies. In the existing noise mitigation techniques, there is still no evidence that could prove the effectiveness of the absorption of the acoustic energy from the Scholte waves. But it also provides a new insight into the investigation of improving the mitigation techniques for the low-frequency sound waves through targeting the Scholte waves at the seabed interface. This is not in the scope of this thesis.

Figure 2.4: Hydrotechnik Lübeck: the Big Bubble Curtain with a jack-up vessel by at the OWF Borkum West II (Photo: Trianel / Hero Lang)

2.2.1 Air-bubble curtain

The Big Bubble Curtain (BBC) has been one of the most widely-used noise mitigation systems. As shown in the Figure 2.4, a BBC is formed by free rising bubbles generated by compressed air injected from the perforated tube pre-installed at the seabed. As the *acoustic impedance* can be expressed as $Z = \rho c$, the use of the air-bubble curtain will create a significant impedance mismatch between the water and the bubbly liquid by modifying the density and sound speed in the mixture. The air-bubble curtain aims at enclosing the noise source in the interior domain and therefore reduce the sound pressure level in the exterior fluid domain. Whereas the resonance of the individual bubble plays a negligible role for the contribution to the sound reduction. The reason is that the target frequency range is away from the resonance frequencies of the free air bubbles. If we consider air bubbles with large-range radii from about $5\mu m$ to $3mm$, the resonance frequency of the bubble in the mixture can range from 20Hz to 10 MHz [12]. However, for a typical air bubble with radii of 1000 μm in the mixture, the resonance frequency varies from 3.25 kHz to 6 kHz, provided a 30 meter water-depth field is given [3], which is way beyond the target frequency of about $f < 500Hz$ for the installation of large monopiles.

There are abundant theoretical investigations on the acoustic behaviour of air bubbles in water. Among those studies, to predict the noise reduction by the application of air-bubble curtain in offshore pile driving, Tsouvalas and Metrikine [3] developed a three-dimensional semi-analytical model. Their study aims to investigate the physical mechanism of the noise reduction and examine the influence of key parameters of the system. Therefore, it could provide a solid theoretical background for the improvement of the air-bubble curtain. In this model, the air bubble curtain is modelled as the homogeneous fluid layer with modified compressibility and density as shown in the Figure 2.5 [11]. The results of this study show that this method largely depends on how much air is supplied and the bubble size, which

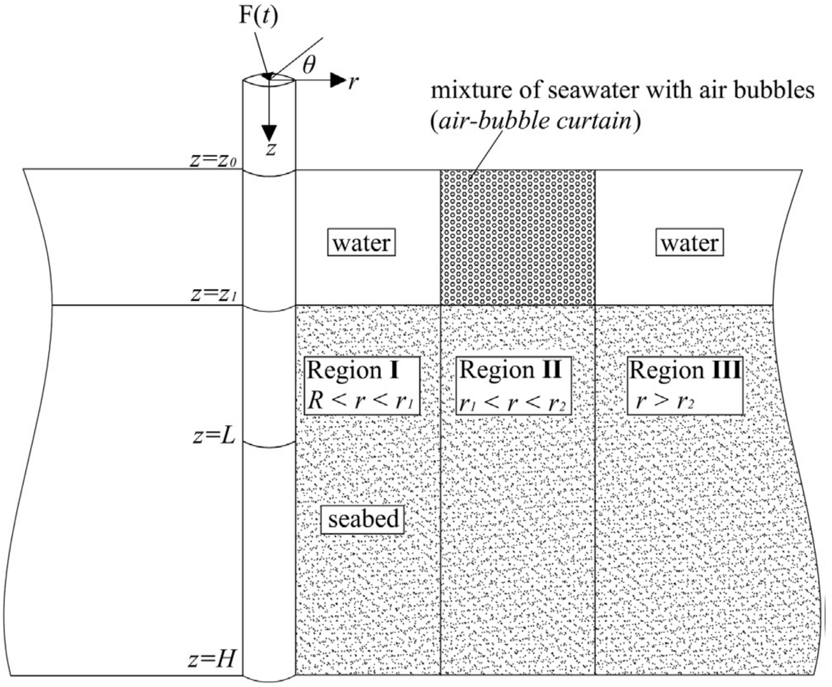

Figure 2.5: The geometry of the model by Tsouvalas and Metrikine [3], which consist of four domains, the pile, the interior fluid and sediment domain, the region containing air bubble curtain and underlying soil and the exterior domain.

can be costly and more efficient for high-frequency waves. In addition, the contribution of this mechanism to the noise reduction is still questionable during the installation of large monopiles.

2.2.2 Noise mitigation screen

The principal mechanism of Noise Mitigation Screen (NMS) is a shielding effect created by using a double-walled cylindrical shell around the pile, as shown in Figure 2.6 [4]. The relatively low-density air could fill in the space between the two walls. By doing this, the outer wall of the screen would remain much less affected by the vibration of the inner wall. The system is developed by IHC offshore systems and has been used in several commercial projects.

However, in the present design, soil vibrations are not blocked by NMS. This method is relatively costly and not flexible enough for different size piles. Also, based on the structure of the noise mitigation screen, the installation for NMS itself is quite challenging [3].

2.2.3 Hydro-sound damper

Hydro-Sound Damper (HSD) was developed by Offnoise-Solution GmbH between 2007 and 2010 to reduce the offshore piling noise, as shown in Figure 2.7. The system consists of encapsulated air balloons and PE-foam with high dissipation on the impact sound. The resonance frequency can be determined by using the proper sized elastic balls. The damping ratio can

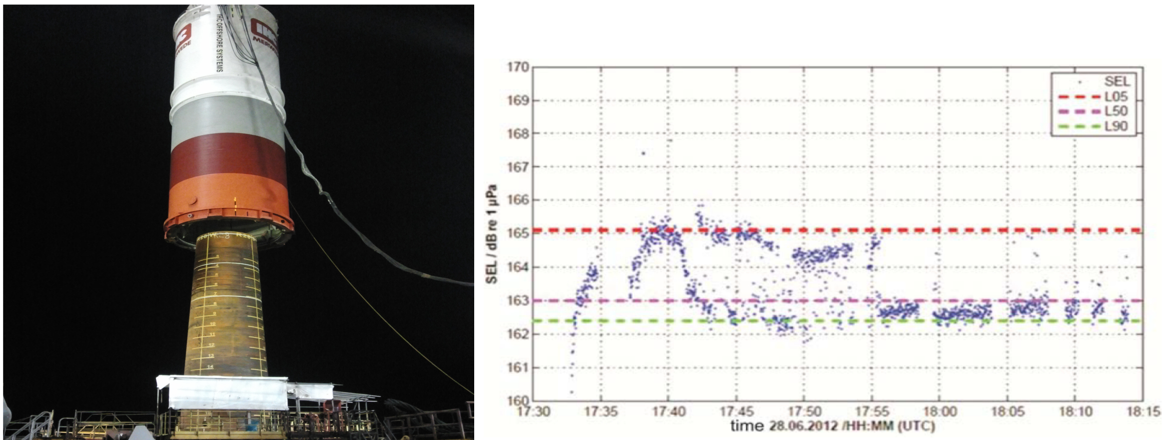

(a) The IHC noise mitigation screen (NMS) for noise mitigation at the OWF Riffgat

(b) Broadband noise sum level measured at 750m during piling at the OWF Riffgat

Figure 2.6: IHC: Noise Mitigation Screen [4].

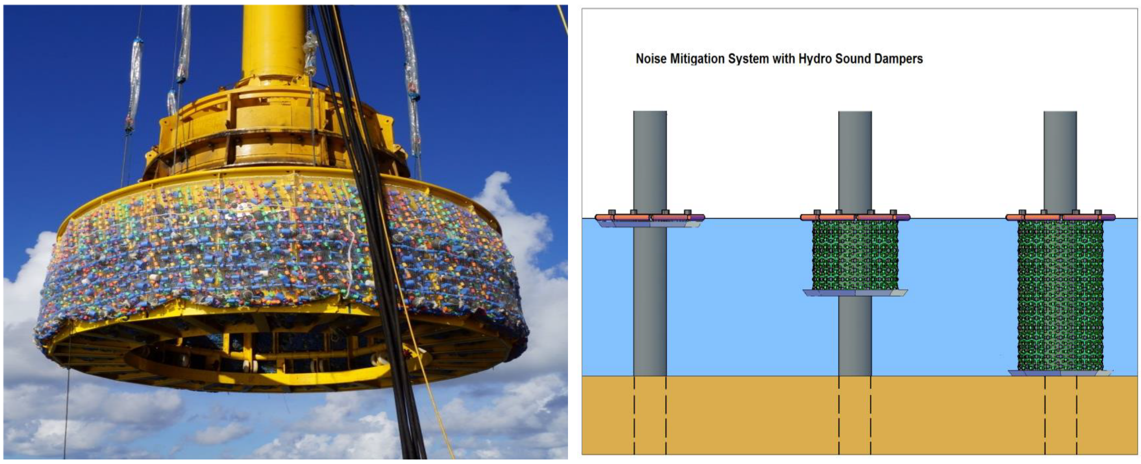

(a) The hydro-sound damper system for noise mitigation at OWF Amrumbank West

(b) The schematic for the deployment of HSD-system

Figure 2.7: Offnoise-Solution GmbH: HSD-system [5].

be well-controlled through the PE-foam elements. The energy can be absorbed through the resonance of balloons, dissipation and material damping of foam elements. Compared with Air-Bubble Curtain, HSD-system is independent on the compressed air. Therefore, there is no need to supply air-compressor from the installation vessel. Besides, with the use of nets of air-filled balloons, the system will not be influenced by tidal currents. This provides an efficient alternative for the air-bubble curtain.

The studies based on HSD has been discussed by Elmer and Savery mainly through measurements and offshore tests, which already shows that the noise reductions between 10 dB(SEL) and more than 20 dB(SEL) have been achieved from Figure 2.8 [5]. It is also worth to be mentioned that the HSD-system could be considered as a potential noise mitigation technique

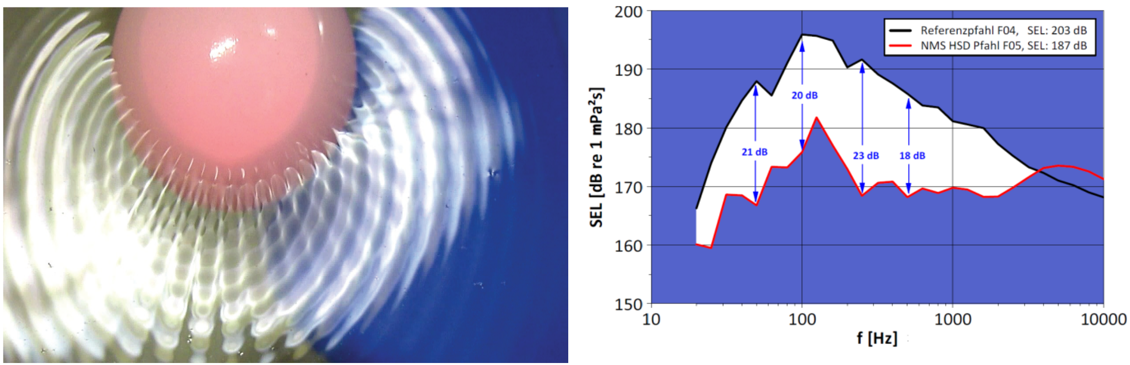

(a) A vibrating air-filled HSD

(b) 1/3 SEL spectra of underwater piling noise with and without HSD-system

Figure 2.8: Offnoise-Solution GmbH [5]: measurement and offshore test using HSD.

for the Scholte waves at the seabed interface due to its nets configurations and is easy to be deployed on the seabed [3]. However, compared with Air-Bubble Curtain and Noise Mitigation Screen (developed by IHC Offshore Systems), HSD-system is still lack of rich experience gained in offshore commercial projects.

2.2.4 Open-ended resonator

The innovative open-ended resonators were developed by AdBm Technologies and the University of Texas at Austin[6]. The acoustic behaviour of both the open-ended resonators and the encapsulated air bubbles was investigated through laboratory tests and open-water tests. This aims to compare the performance of two noise mitigation techniques and provide a resonator-based noise mitigation system for offshore pile driving.

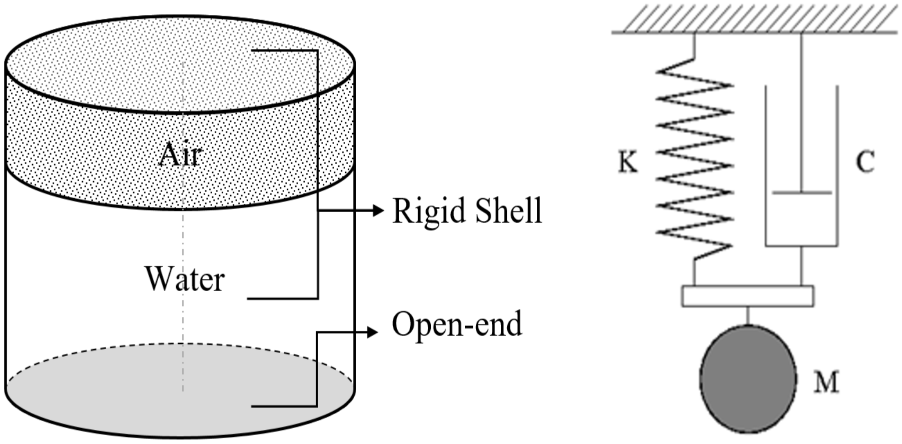

Figure 2.9: The geometry for general underwater Helmholtz resonator and 1DOFS [6].

The open-ended resonators have the same primary mechanism as the Helmholtz resonators that have been widely used in airborne noise reduction. In the 1850s, the first Helmholtz resonator is created by Hermann von Helmholtz, a German physicist who made the significant contributions in acoustics and other scientific fields. The phenomenon of traditional Helmholtz resonator can be described as follows: provided that you have a specific volume rigid bottle with an open-end and a small neck, when you blow the bottle, the air column at the neck of the bottle will resonate at a particular frequency and you could hear it clearly. Therefore, a particular frequency from the complex sound is picked up through a certain configuration of the Helmholtz resonator.

Nowadays, the application of Helmholtz resonators can be used in architectural acoustics to mitigate the undesirable sound or be used as exhaust resonators to alter the note of the sound of motorcycle and car exhaust. Although the application of the Helmholtz resonator is rather limited to be used in the mitigation of the underwater noise, the primary working mechanism is based on the same fundamental physics. As shown in Figure 2.9, the resonator is schematically depicted as a rigid cylinder tube with an opening end. When the open-ended resonator is deployed into the water with the open end facing the seabed, the air will be encapsulated and compressed in the container. This creates an analogous single-degree-of-freedom system. By using the specific shape and volume of the resonator, one can tune the resonator to the target frequency. For low-frequency sound waves (f<500 Hz), the dimension of the open-ended resonator is relatively small compared with the wave length above 3 m. Therefore, the air will play the role of the massless spring in the ideal single-degree-of-freedom system. The point mass can be seen as the water column in the open-ended resonator.

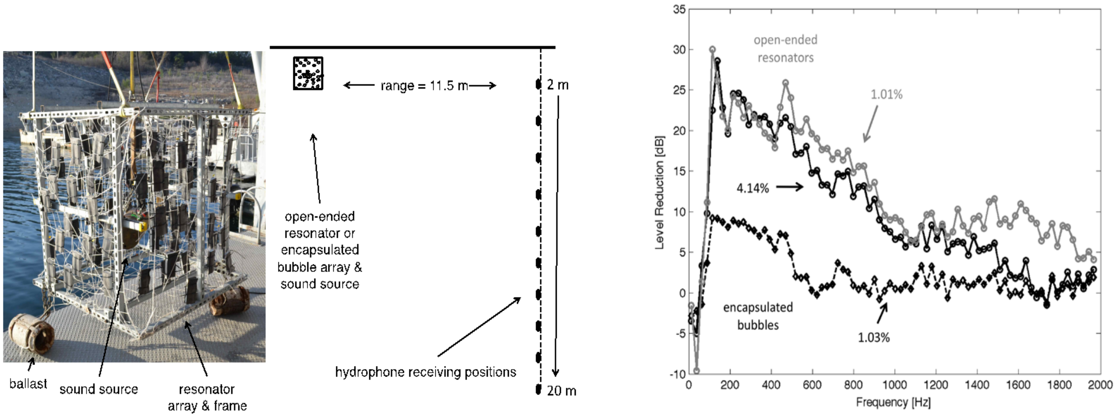

(a) The geometry of the lake measurements

(b) Depth averaged noise reduction for arrays of resonator with various void fractions depicted in thr graph

Figure 2.10: AdBm Technologies [6]: Lake tests in Austin, Texas.

In order to compare the acoustic behaviour of an individual open-ended resonator and encapsulated air bubble, a laboratory test was first made to measure the resonance frequency and the quality factor. The results showed that acoustic performance is well-predicted by Church's model [13]. The open-ended resonator has the similar primary resonance frequency with the encapsulated bubble, but only with $1/12th$ of the volume of the air encapsulated, compared with the encapsulated bubble. This indicates that the use of open-ended resonators could mostly save the amount of ballast to compensate for the buoyancy of the air. In addition, the open-ended resonator has a secondary, lower resonance frequency and both the primary and secondary resonance frequencies have a higher Q factor compared with encapsulated air bubbles. A resonator with a higher Q is considered to be a better oscillator and attenuator. However, the appearance of two resonance peaks still need further investigation to have a solid physical explanation [6].

Other open-water measurements were also made by AdBm Technologies in Lake Travis, near Austin, Texas. Arrays of both open-ended resonators and encapsulated air bubbles were attached to the steel frame with a noise source placed in the middle of the frame. The results from this tests show that with the same void fraction of two resonators, the open-ended resonators have better performance for the noise reduction. Therefore, to achieve the same level of noise reduction, the open-ended resonators will need approximately four times less ballast. The results also indicate a broadband reduction from 100 Hz to 1000 Hz as shown in Figure 2.10 [6].

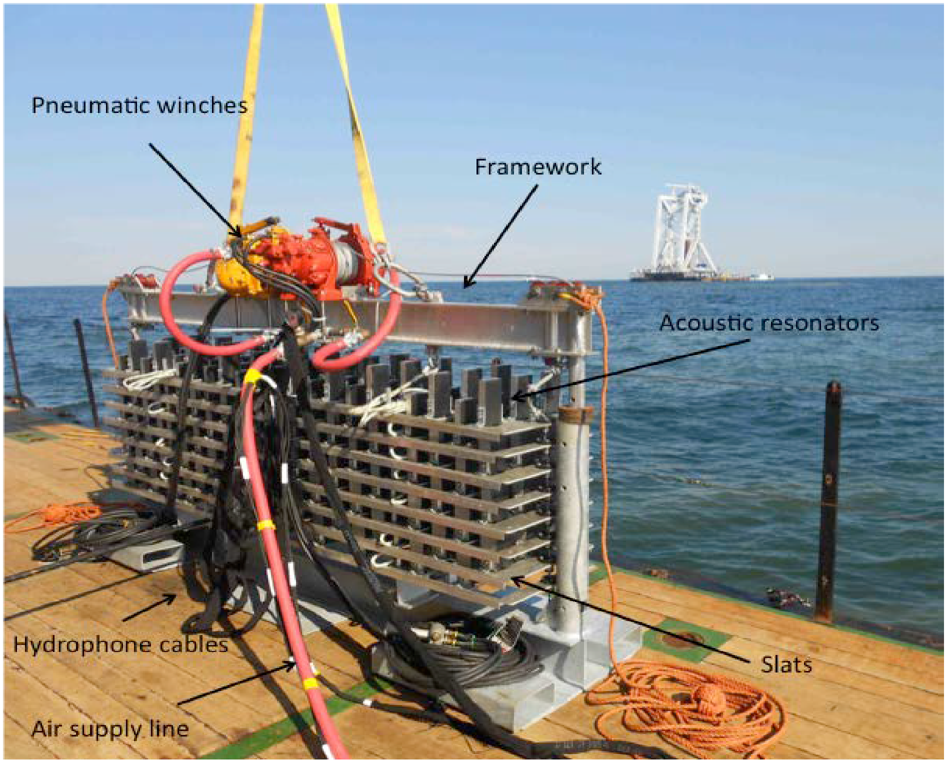

Figure 2.11: The photo of the open-ended resonator panel in offshore demonstration tests [7].

An offshore demonstration test of the open-ended resonator based noise abatement system was conducted by AdBm Technologies in cooperation with Ballast Nedam, during pile driving operations for the Butendiek Offshore Wind Farm. The tests aimed to demonstrate the deployment in the North sea environment and the acoustic performance of the open-ended resonators for offshore pile driving.

As shown in the Figure 2.11[7], the demonstration panel consists of 240 open-ended resonators was deployed at the location of 385 m away from monopile BU-32 and 285 m and 750 m away from monopile BU-21. The results shown in the Figure 2.12 [7] were for the monopile BU-21. The one-third-octave band level reduction at both sites indicates an adequate acoustic

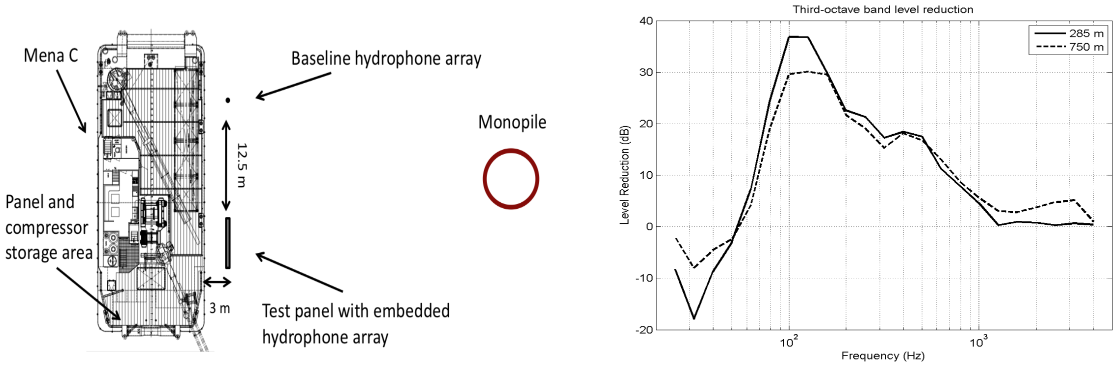

(a) The configuration of the offshore demonstration tests.

(b) Depth averaged noise reduction for arrays of resonator with various void fractions depicted in thr graph

Figure 2.12: AdBm Technologies: Offshore demonstration tests for monopile BU-21 at Butendiek Offshore Wind Farm [7].

performance of noise reduction, which demonstrates the open-ended resonator as a potential alternative to the present noise mitigation techniques. It is worth mentioning that, compared with the traditional noise abatement techniques, the resonator-based noise mitigation system can mitigate broadband underwater sound, especially the low-frequency sound waves below 400 Hz. This indicates the new noise mitigation technique can be used for large scale construction of the wind farm.

However, compared with the aforementioned noise mitigation techniques, the open-ended resonator system is still lacking experience in commercial projects. In the opinion of the author, further theoretical and numerical investigations are needed in order to optimise the configuration of the system and develop more effective deployment methods. Full-scale tests for the complete system can be conducted to verify the applicability of the system for the commercial projects.

From the discussion above, the open-ended resonator is proved to be a promising way to mitigate the noise. Apart from using individual noise mitigation techniques, combinations of two different noise mitigation systems can be exploited to provide a *multi-barrier* [3]. Such a composite noise mitigation system consists of an open-ended resonator system in the vicinity of the pile and an air-bubble curtain at larger distance from the pile.

Chapter 3

Modified Helmholtz Resonator and Hydro-Sound Damper

In Chapter 3, the underlying physics of the noise reduction by the application of the open-ended resonator is investigated. The theory of the resonance frequency for the underwater open-ended resonator is presented. In addition, a finite-element model in COMSOL Multiphysics is developed for the open-ended resonator, which is used to validate the theory of the resonant frequency of this new type of resonators. A parametric study for the open-ended resonator and the encapsulated air bubble was conducted to find the optimum configuration for the targeted frequency range. The frequency response function for the open-ended resonators with various resonant frequencies was derived.

3.1 Underwater Helmholtz resonator

In Chapter 2, we already discussed the underlying physics of noise reduction by open-ended resonators, which follows the same primary mechanism of absorbing the energy from the sound waves into oscillations of the resonators. In order to tune the resonance at our target frequency, the rigorous mathematical derivation of the resonance frequency from the particular configuration of the resonator is presented. The calculation is based on the classical formula for the resonance frequencies of a Helmholtz resonator, which was derived a hundred years ago. The traditional formula for the calculation of resonant frequency of a Helmholtz resonator is as follows [8]:

$$f = \frac{c}{2\pi}\sqrt{\frac{A}{V(L_{neck} + \alpha)}} \tag{3.1}$$

where c is sound speed in the air, A is the area of an aperture, V is the volume of the resonator, α is the end correction factor, L_{neck} is the length of the neck of the resonator.

In order to verify the theoretical expression of the resonance frequency and obtain the acoustic performance of the open-ended resonators, a finite element model was developed in the software package COMSOL. Assuming a linear behaviour of the fluid-resonator system, it suffices to examine the response in the frequency domain. The numerical results of the calculation of the resonance frequencies will be verified by the comparison with analytical solutions for the open-ended resonator.

3.1.1 Classical formula

Before we derive the resonance frequency of open-ended resonator, it is advisable to briefly review the derivation of the resonance frequency for Helmholtz resonator. This can be found in many books dealing with an introduction to acoustics.

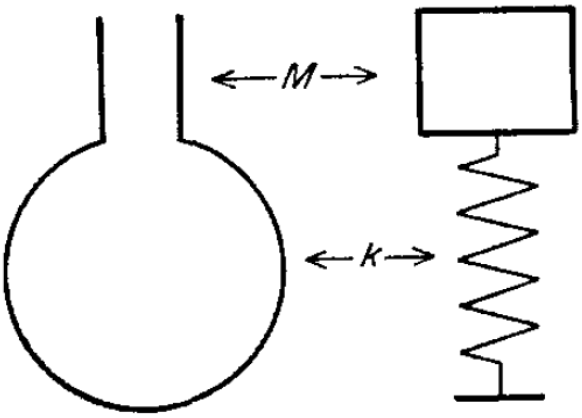

Figure 3.1: Mechanical and acoustical analogy of a Helmholtz resonator[8]

First, let us consider a basic force balance:

$$\vec{F} = m\vec{a} \tag{3.2}$$

where m is mass $m = \rho V_{neck} = \rho A L_{neck}$, and $\vec{a}$ is accelaration. One can therefore write

$$\frac{d^2x}{dt^2} = \frac{F}{m} \tag{3.3}$$

According to Laplace, when sound travels in a gas, there is no time for heat conduction in the medium and so the propagation of sound is adiabatic. For an adiabatic process, the mathematical equation for the ideal gas can be expressed as:

$$\frac{P}{P_0} = -\gamma\frac{\Delta V}{V} \tag{3.4}$$

where P_0 is atmosphereric pressure, γ is the ratio of specific heats under constant pressure and volume, ΔV is the increment for the volume $\Delta V = -Ax$, where A is the cross-sectional area and x is displacement. Solving for P yields:

$$P = \gamma\frac{AxP_0}{V} \tag{3.5}$$

where $x(t) = Im(e^{i\omega t})$ or $Re(e^{i\omega t})$, and ω is angular frequency. By substition of the above relation into F, we have

$$F = PA = \gamma \frac{AxP_0}{V} A = \gamma \frac{A^2 x P_0}{V} \tag{3.6}$$

Now, Eq. (3.3) becomes

$$\frac{d^2x}{dt^2} = \frac{\gamma \frac{A^2 x P_0}{V}}{\rho A L_{neck}} \tag{3.7}$$

$$-\omega^2 Im(e^{i\omega t}) = \frac{\gamma A P_0}{\rho V L_{neck}} Im(e^{i\omega t}) \tag{3.8}$$

$$-\omega^2 = \frac{\gamma A P_0}{\rho V L_{neck}} \tag{3.9}$$

$$-4\pi^2 f^2 = \frac{\gamma A P_0}{\rho V L_{neck}} \tag{3.10}$$

$$f^2 = -\frac{1}{4\pi^2} \frac{\gamma A P_0}{\rho V L_{neck}} \tag{3.11}$$

Hence, the resonance frequency is obtained as:

$$f = \frac{1}{2\pi} \sqrt{\frac{\gamma A P_0}{\rho V L_{neck}}} \tag{3.12}$$

The sound of speed is defined as $c = \sqrt{\gamma \frac{P_0}{\rho}}$:

$$f = \frac{1}{2\pi} \sqrt{\frac{\gamma A P_0}{\rho V L_{neck}}} = \frac{1}{2\pi} \sqrt{\gamma \frac{P_0}{\rho}} \sqrt{\frac{A}{V L_{neck}}} = \frac{c}{2\pi} \sqrt{\frac{A}{V L_{neck}}} \tag{3.13}$$

Hence, the classical formula for resonance frequency of Helmholtz resonator without end correction is obtained.

3.1.2 End correction

It is worth to mention the importance of the end correction, since without considering α, it could lead to a certain discrepancy between the theoretical resonance frequency and the measured one. Let us focus on the interaction of the fluid and the resonator.

As the fluid exits the neck of the resonator, the acoustic waves disperse, and the acoustic pressure drops. Because the waves will continue to move along the neck and remain its initial motion, physically they will not disperse immediately. Therefore, the fluid still occupies the region downstream of the neck. In order to compensate for this end correction, an additional factor will be added to the length of the neck. We consider that the additional inertia could lead to an effective increase in L_{neck} by γa, where a is the radius of the opening end [17]. Thus, the total length of the lumped-parameter inertance L_{neck} will be

$$L'_{neck} = L_{neck} + \gamma a \tag{3.14}$$

The value of γ has the following range as:

$$0.61 < \gamma < 0.85 \tag{3.15}$$

The lower limit corresponds to an unflanged pipe while the upper limit corresponds to a pipe end with an infinite baffle (flanged).

Thus, in our case, we choose $\gamma = 0.61$. Now, the theoretical expression for the resonance frequency of the open-ended resonator is derived as:

$$f = \frac{c}{2\pi}\sqrt{\frac{A}{V(L_{neck} + \gamma a)}} \tag{3.16}$$

3.1.3 Derivation of the resonance frequency for underwater resonators

Under atmospheric pressure, at sea level and at 15°C, the density of air is approximately 1.225 kg/m^3. However, since the air column encapsulated in the resonator is under static hydraulic pressure and plus atmosphere pressure (unit of Pa), as:

$$P = \rho g h + 10^5 \tag{3.17}$$

According to the relationship between density, pressure and temperature, we have the density of air modified as:

$$\rho_{air} = \frac{P}{R \cdot T} \tag{3.18}$$

where R is specific gas constant, for dry air R is equal to $287J/(K * kg)$, T is the temperature in the unit of K. We could assume the temperature is 15°C, that is $288K$.

In vibrations that give rise to sound, however, the changes are fast and so the temperature rises on compression, giving a larger change in pressure. Physically it can be considered as an adiabatic process, meaning that heat has no time to move, and the resulting equation involves a constant γ, the ratio of specific heats, which is about 1.4 for air.

As a result, the pressure change p produced by a small volume change δV is just:

$$\frac{P}{P_0} = -\gamma \frac{\Delta V}{V_a} \tag{3.19}$$

Now the mass m is moved by the difference in pressure between the top and bottom of the neck, i.e. a nett force $P \cdot S$, so we write Newton's law for the acceleration a:

$$\vec{F} = m\vec{a} \tag{3.20}$$

$$\frac{d^2x}{dt^2} = \frac{F}{m} = \frac{P \cdot S}{m_w} \tag{3.21}$$

where m_w is the mass of water column inside the resonator, or the acoustic mass:

$$m_w = \rho_w S L \tag{3.22}$$

where L is the length of the water column. It is worth mentioning that due to the static pressure, $L(h)$ is a depth-dependent value, a function of h. Thus, by substituting $\vec{F}$, P and m_w, we have

$$\frac{d^2x}{dt^2} = \frac{P \cdot S}{\rho_w L} = -\frac{\gamma P_0 S}{V_a \gamma_w L} x \tag{3.23}$$

Assume $x(t) = Im(\tilde{A} \cdot e^{i\omega t})$, substitute into the upper equation, we obtain:

$$-\omega^2 Im(\tilde{A} \cdot e^{i\omega t}) = -\frac{\gamma(P_0 S}{V_a \rho_w L} Im(\tilde{A} \cdot e^{i\omega t}) \tag{3.24}$$

Thus,

$$\omega^2 = \frac{\gamma P_0 S}{V_a \rho_w L} \tag{3.25}$$

$$f = \frac{1}{2\pi}\sqrt{\frac{\gamma P_0 S}{V_a \rho_w L}} \tag{3.26}$$

Since $c = \sqrt{\frac{\partial P}{\partial \rho}}$, we obtain that:

$$f = \frac{c_{air}}{2\pi}\sqrt{\frac{\gamma S}{V_a L}} \tag{3.27}$$

Because $\rho_{air} = P_0 / R \cdot T$, by substituting it into the volume of air, we obtain that

$$V_a = \frac{m_a}{\rho_a} = \frac{m_a R T}{P_0} = \frac{\rho_a R T}{P_0} V_r \tag{3.28}$$

where $\rho_a = 1.225 kg/m^3$, V_r is the volume of the resonator, we could also add a factor to compansate for the loss of air during the installation process.

After substitution. we obtain that:

$$f = \frac{1}{2\pi}\sqrt{\frac{\gamma P_0 S}{V_a \rho_w L}} \tag{3.29}$$

$$= \frac{1}{2\pi}\sqrt{\frac{\gamma P_0^2 S}{\rho_a R T \rho_w L V_r}} \tag{3.30}$$

$$= \frac{P_0}{2\pi}\sqrt{\frac{\gamma S}{\rho_a R T \rho_w L V_r}} \tag{3.31}$$

$$\tag{3.32}$$

Considering the influence of the end correction, we could rewrite the expression as:

$$f = \frac{\rho_w g h + 10^5}{2\pi}\sqrt{\frac{\gamma S}{\rho_a R T \rho_w (L + \alpha) V_r}} \tag{3.33}$$

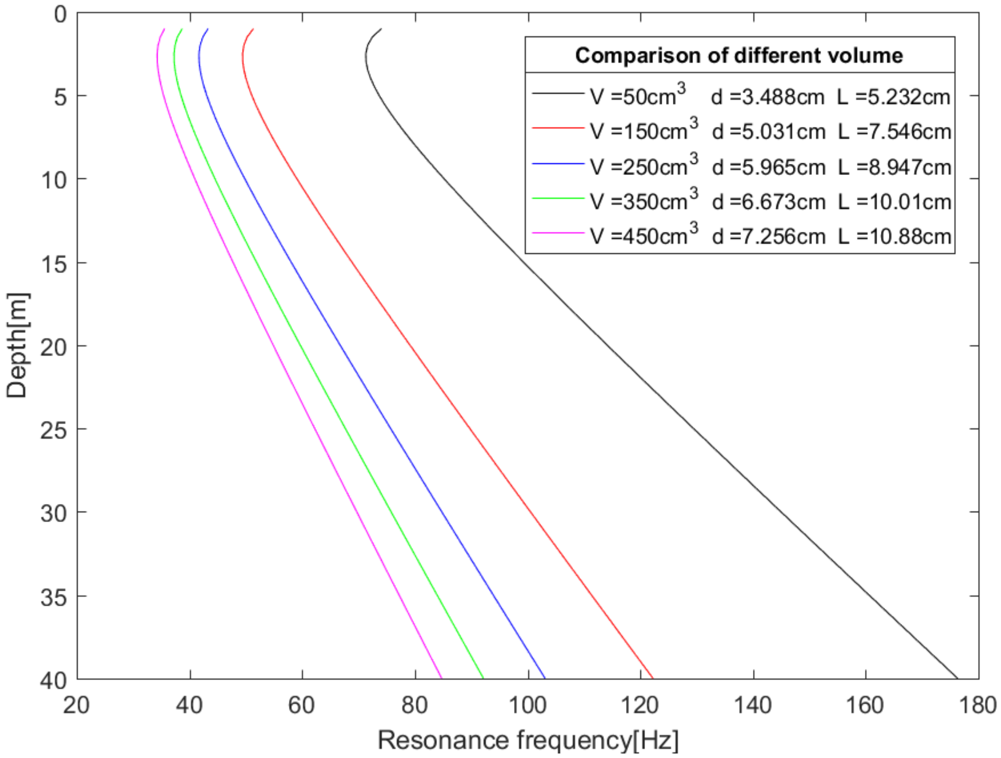

Figure 3.2: The influence of the volume for the open-ended resonator

Hence, the resonance frequency of underwater open-ended resonator is obtained.

Before the discussion, first we need to define a factor for the configuration of the resonator, which is slenderness ratio and is define as:

$$\beta = \frac{Length}{Diameter} \tag{3.34}$$

In order to investigate the sensitivity of the configuration on the resonance frequency of Helmholtz resonator. We plotted the resonance frequency of the open-ended resonator at water depth from 0 m to 40 m. Given the form of Eq. (3.33), we realize that L is also a function of h, we have

$$\begin{aligned} L &= \frac{V_{water}}{S} = \frac{V_r - V_a}{S} & (3.35)\\ &= \frac{(1 - \frac{\rho_a RT}{P_0})V_r}{S} & (3.36)\\ &= \frac{V_r}{S}(1 - \frac{\rho_a RT}{P_0}) & (3.37)\\ &= \frac{V_r}{S}(1 - \frac{\rho_a RT}{\rho_w gh + 10^5}) & (3.38) \end{aligned}$$

In order to have a clear view of the tendency of the curve, we could define the following two

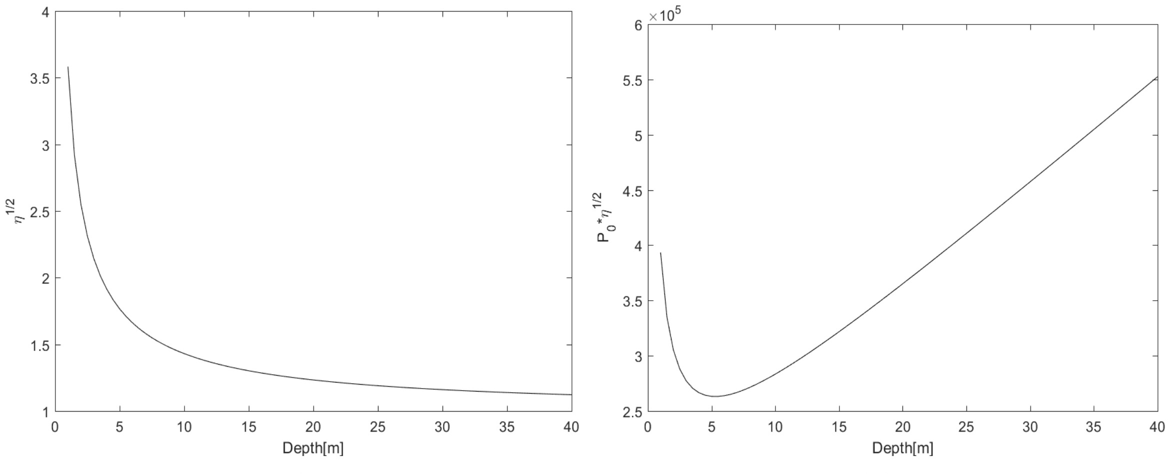

(a) **(b)**

Figure 3.3: Sensitivity of water depth to the solutions: (a) $\eta^{-\frac{1}{2}}(h)$; (b)$P_0(h) \cdot \eta(h)$.

variables and plot them by assuming $\beta = 1.5, V = 50cm^3$ for as shown in Figure 3.3:

$$\eta = 1 - \frac{\rho_a RT}{\rho_w gh + 10^5} \tag{3.39}$$

$$P_0 \cdot \eta = (\rho_w gh + 10^5) \cdot \eta^{-\frac{1}{2}} \tag{3.40}$$

It shows that due to the influence of the static pressure, when the water depth is above 5 meters, the compression of the air column has a significant influence on the $\eta^{-\frac{1}{2}}(h)$. Therefore it causes a turning point on the curve around $h = 5m$. When the water depth is below 5 meters, $\eta^{-\frac{1}{2}}(h)$ changes steadily and converge to 1 as shown in Figure 3.3(a). Therefore, when P_0 is relatively large, the resonance frequency - depth curve is nearly in a linear relationship as shown in the Figure 3.2.

The volume of resonator mainly influences the frequency range of the resonator. The graph shows that the resonators with higher volume can give lower resonance frequency. The potential reason can be that by an increase of the size of the resonator air volume, the water mass inside the resonator can move more freely. Physically, the density of the air encapsulated in the resonator remains the same, in deeper water, the stiffness of the air has a positive correlation with the air density. However, the mass of the water column in the resonator increases with the volume of the resonator. From the definition of the resonance frequency $\omega_0 = \sqrt{\frac{k}{m}}$, it is not difficult to find that the resonant frequencies shift to lower range.

Another dominating factor for tuning the resonance frequency is the slenderness ratio β(=L/2a) as shown in Figure 3.4. By changing the β from 0.3 to 1.1, the shape of a resonator is stretched under the same volume $216.8cm^3$. We could observe from Figure 3.4 that the increase of β will cause the resonance frequency more consistent in depth.

Figure 3.4 also shows that the higher the slenderness ratio is, the lower the resonance frequency will be. The partial reason can be the end correction γa. For small β, the resonator has a relatively large cross-sectional area, which leads to a larger end correction influence. Thus, physically, for resonators with a large cross-sectional area, more additional fluid will set into motion due to the inertia.

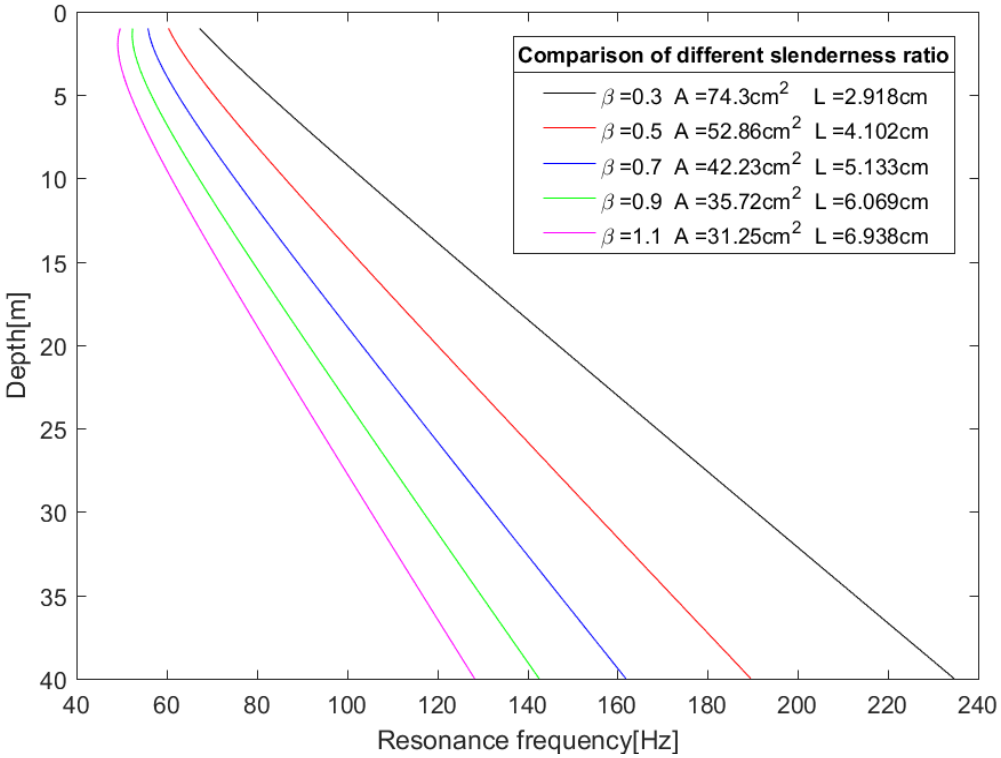

Figure 3.4: The influence of the lenderness ratio for the open-ended resonator

We could also find the reason directly from the analytical solution for the resonance frequency. By increasing the slenderness ratio, $\alpha = \frac{Area}{Length}$ decreases, which lead to the decrease of the resonance frequency as shown in Figure 3.5.

3.1.4 A 3-D finite element model for an Open-Ended Resonator

A 3-D finite element model for a single Open-Ended Resonator was developed in COMSOL Multiphysics. The resonator has the same cylindrical configuration with an opening end as shown in Figure 3.8. The detailed geometrical parameters are given in Table 3.1. The air volume can be directly determined by the water depth. The waveguide consists of four rigid surface boundaries as shown in Figure 3.6. The plane wave radiation condition is adopted on both inlet and outlet boundary, which could allow the incoming plane wave travel through the inlet to outlet and allow the sound waves leave the domain with minimal reflections. The shell of the open-ended resonator is modelled as the perfectly rigid boundary.

The incident Sound Pressure Level in this section is defined as:

$$SPL = 10 \log \frac{p^2}{{p_r}^2} \tag{3.41}$$

where p_r is the presently accepted reference sound pressure level equal to $1 \mu Pa$ or $10^{-6} Pa$. Since we are dealing with harmonic waves, the rms value of a sinusoidal process is $1/\sqrt{2}$ of

Table 3.1: Material properties and geometrical parameters for Open-Ended Resonator model

Parameter	Value	Unit	Description
d	10	m	Water depth
W_d	0.5	m	Y-Width of the fluid domain
H_d	0.5	m	Z-Height of the fluid domain
L_d	6	m	X-Length of the fluid domain
V	216.18×10^{-6}	m^3	Volume of the resonator
SF	0.539	-	Slenderness ratio
a	$\frac{V}{2\pi SF}^{1/3}$	-	Radius of the resonator
c_w	1485	m/s	Speed of sound in the water
ρ_w	1×10^3	kg/m^3	Density of water
c_a	343	m/s	Speed of sound in the air
P_a	1	atm	Absolute pressure /Atmosphere
ρ_a	1.225	kg/m^3	Density of air
p_0	1	P_a	Incident wave pressure
θ	pi/2	rad	Angle of incident wave
k_x	0	-	x-wave propagation direction
k_y	sin(theta)	-	y-wave propagation direction
k_z	cos(theta)	-	z-wave propagation direction
x_0	0.2	m	x center coordinate
y_0	5	m	y center coordinate
z_0	0.2	m	z center coordinate
f_{min}	1	Hz	Minimum value for frequency sweep
f_{max}	300	Hz	Maximum value for frequency sweep

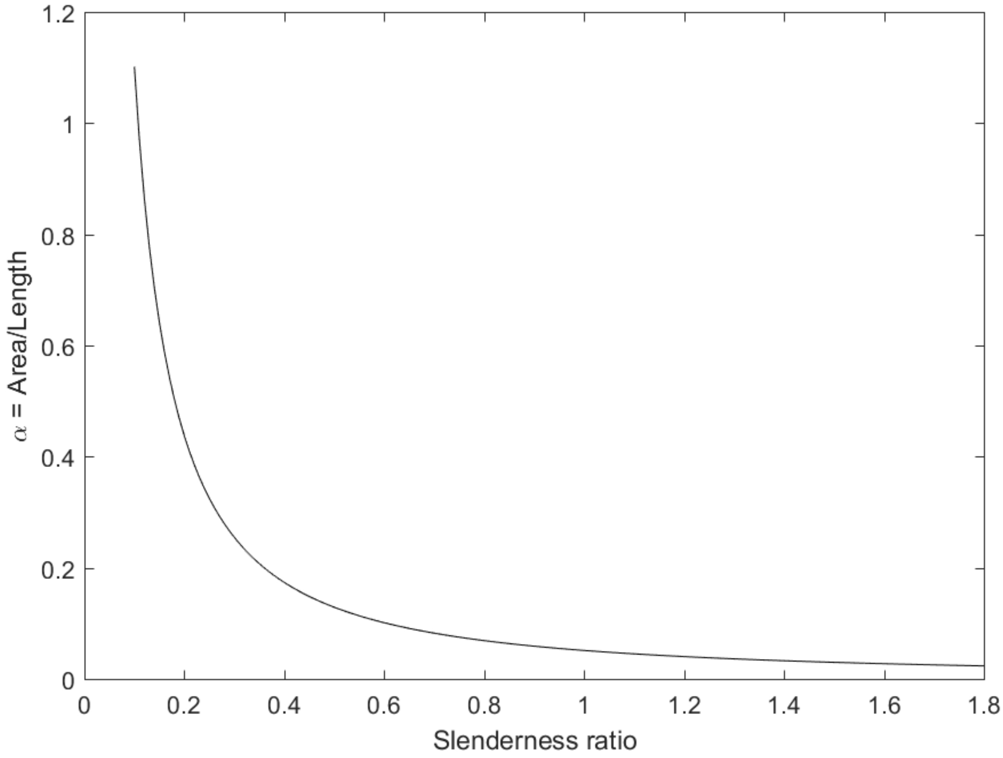

Figure 3.5: The influence of the slenderness on α

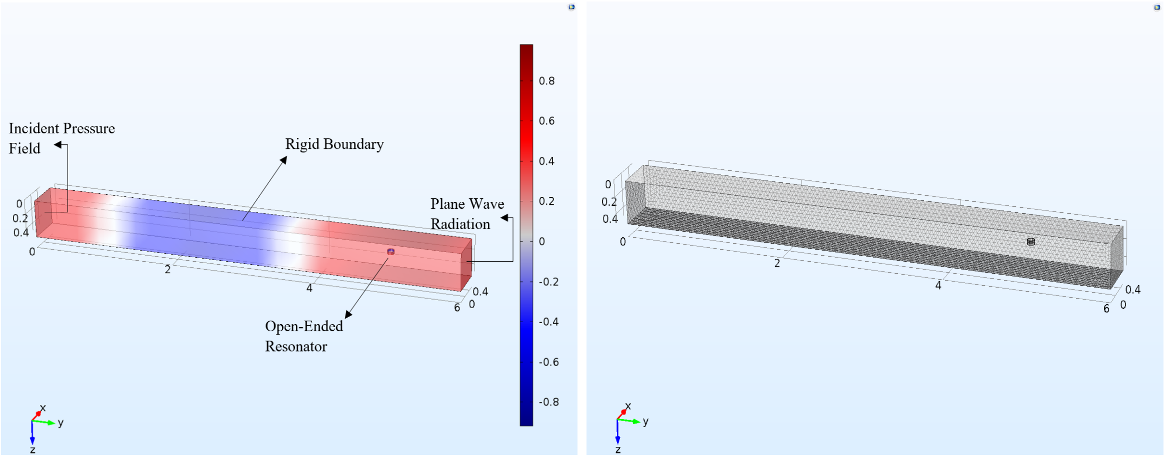

(a) **(b)**

Figure 3.6

the its amplitude, so that the SPL can be expressed as:

$$SPL = 10\log\frac{p_{rms}^2}{{p_r}^2} = 10\log\frac{0.5{P_{in}}^2}{{p_r}^2} = 10\log(0.5\times1\times10^{12}) = 117dB \tag{3.42}$$

Table 3.2: Case study for the resonance frequencies at various water depth

Case	Water depth (m)	Resonance frequency in 3-D COMSOL model (Hz)	Theoretical resonance frequency without end correction (Hz)	Theoretical resonance frequency with end correction(Hz)
1	10	85	123.4	83.7
2	25	136	178.9	132.8
3	40	187	240.6	183.2

Table 3.3: Case study for the resonance frequencies at various volumes of open-ended resonators

Case	Volume (cm^3)	Resonance frequency in 3-D COMSOL model (Hz)	Theoretical resonance frequency with end correction(Hz)
1	100	250	245.36
2	216	190	189.76
3	400	161	154.6
4	600	136	135
3	800	130	122.68

3.1.5 Results and discussion

The first simulation test is to investigate the influence of the water depth to the open-ended resonator. Based on the same configuration of the resonator, the calculation of the resonance frequency also is given by using the theoretical solution with end correction and without end correction, respectively. As seen in Table 3.2, the results show that there is a large discrepancy between the COMSOL simulation and the theoretical model without considering the end correction. When the theoretical solution includes the end correction factor, the analytical results provided a reasonable agreement with the numerical results recording to the predicted resonance frequency. In the second numerical test with resonators of various volumes as shown in Table 3.3, the prediction of the resonance fequency is closely related to the one based on the theoretical expression.

In order to check the accuracy of the analytical solution of the resonance frequency, the error between the numerical solutions and the analytical solutions can be defined as:

$$\Delta f_{error} = \frac{|f_{analytical} - f_{numerical}|}{f_{numerical}} \tag{3.43}$$

As shown in Figure 3.7, Δf_{error} shows that the deviation is within the acceptable margin. Therefore, Eq. (3.16) can be considered accurate on the basis of the discussions above.

3.2 Hydro-sound Damper

In this section, the theory of the hydro-sound damper will be discussed. The Church's model will be introduced in order to compare the numerical results from COMSOL. To have a

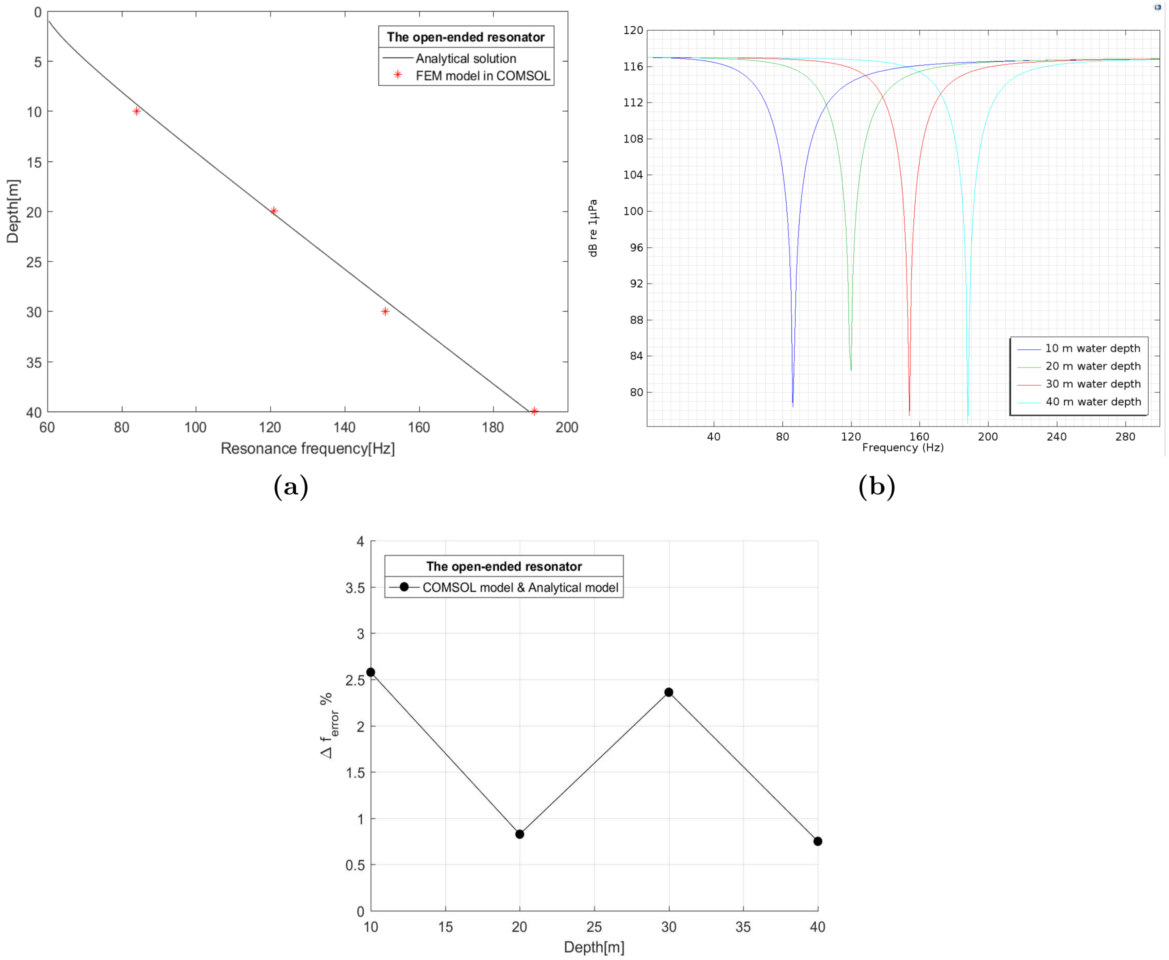

(a) (b)

(c)

Figure 3.7: Open-Ended Resonator model: the average sound pressure level (dB re 1μPa) at the outlet boundary for water depth at 10 m, 20 m, 30 m, 40m, respectively.

better understanding of Hydro-sound damper system, a FE model for a single hydro-sound damper was built in COMSOL. The acoustic behaviour of the resonators is strongly frequency dependent. Hence, the discussion will be based on frequency-domain simulations only. The numerical results of the calculation of the resonance frequencies are verified by comparison with several analytical solutions for both the open-ended resonator model and the hydro-sound damper model.

3.2.1 Church model

To develop a new noise abatement system, it is advisable to investigate the existing resonator-based noise mitigation techniques. Thus, except for the open-ended resonators, the study of encapsulated air bubbles or hydro-sound dampers is another preliminary step for the development of the new design. This section aims to study the acoustic behaviour of an air bubble enclosed by an elastic surface layer.

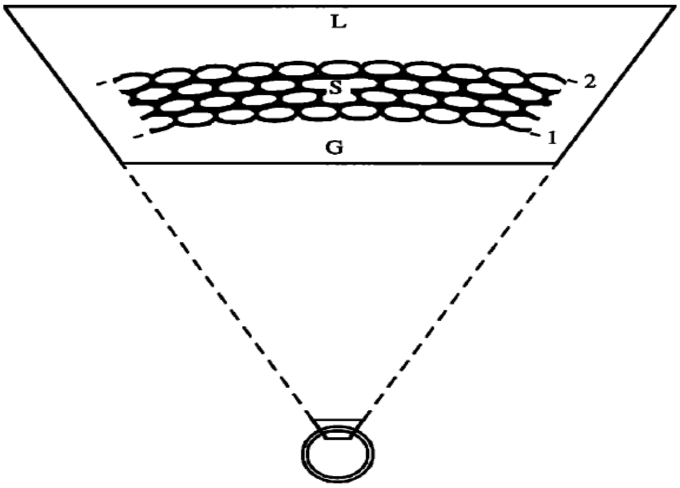

Figure 3.8: The schematic of an encapsulated air bubble with an elastic surface layer

The rigorous theoretical model proposed by Church describes the sound propagation in bubbly liquids, where the bubbles are encapsulated by the solid elastic shell. In the Figure 3.8, it shows the composition of a gas bubble, where G =gas, L =liquid, S =shell, 1 and 2 indicate the interfaces between gas and shell, and shell and liquid, respectively. Although the model was originally developed to describe the acoustic behaviour of the micro bubbles, it seems reasonable to assume that Church theory should equally apply to very large encapsulated bubbles with radii greater than a few centimeters when certain conditions are met.

In this paper, an analytical solution to the equation that describes the behaviour of a gas bubble surrounded by a layer of elastic, damped solid is obtained. The prediction for the resonance frequency and the propagation of the sound waves are presented. The detailed discussion and expressions can be found in [13].

The velocity in the complex sound mixture is given by $c_m = \omega/k_m$, where k_m is the wave number in the bubbly mixture, which it can be expressed as:

$$\frac{c^2}{c_m^2} = 1 + \frac{4\pi c^2 \rho_L}{\alpha \rho_S} \int \frac{R_{01} f(R_{01}) dR_{01}}{\omega_0^2 - \omega^2 + i\delta_t \omega} \tag{3.44}$$

where ρ_L is the density of the liquid, ρ_s is the density of the solid, α is defined as $[1 + (\frac{\rho_L - \rho_s}{\rho_s})\frac{R_{01}}{R_{02}}]$, R_s represents the initial thickness of the solid layer, $R_s = R_{02} - R_{01}$, R_{02} and R_{01} is the outer and inner radius, respectively. The damping contant can be expressed as $\delta_t = \delta_d + 2(b_t + b_a), \delta_d = 4[\frac{V_S \mu_S + R_{01}^3 \mu_L}{R_{02}^3}](\rho_S R_{01}^2 \alpha)^{-1}$. The term $f(R_{01})dR_{01}$ is the number of bubbles per unit volume with radii between R_{01} and $R_{01} + dR_{01}$.

The results of Church model presented below are for individual resonators, and are compared with the results from the finite element model in COMSOL Multiphysics. Thus, the resonance frequency and attenuation are obtained as:

$$\omega_0^2 = (\rho_S R_{01}^2 \alpha)^{-1} \left(3\kappa P_0 - \frac{2\sigma}{R_{01}} - \frac{2\sigma_2 R_{01}^3}{R_{02}^4} + 4\frac{V_s G_s}{R_{02}^3}[1 + Z(1 + \frac{3R_{01}^3}{R_{02}^3})] \right) \tag{3.45}$$

$$A = 20 log_{10} e I_m(k_m) \tag{3.46}$$

where V_s is $R_{02}^3 - R_{01}^3$, σ is the interfacial tension, κ is the polytropix exponent, G_s is the modulus of rigidity.

The results from this study [13] show that the both the resonance frequencies and the attenuation coefficient of an individual encapsulated air bubble can be influenced by the rigidity of the shell. For an encapsulated bubble with a higher stiffness, the resonance frequency will increase while the attenuation will decrease.

The shell material properties that affect acoustic behaviour are taken into account in the model [13] as the shell density, thickness, shear modulus, viscous damping and interfacial tension. The discussion of the calculation of the resonance frequencies will be found in 3.1.5.

3.2.2 Commander and Prosperetti model

Besides the Church model, Commander and Prosperetti [12] developed a rigorous mathematical model for the prediction of the propagation of the pressure waves in bubbly liquids. The complex sound speed in the bubbly liquid can be expressed as[12]:

$$\frac{c^2}{c_m^2} = 1 + 4\pi c^2 \int_0^\infty \frac{af(a)da}{\omega_0^2 - \omega^2 + 2ib\omega} \tag{3.47}$$

Where c is the sound speed in the liquid, c_m is the complex sound speed in the mixture, ω_0 is the natural frequency ,a is the equilibrium radius of the bubble, f is the bubble population distribution function for the per unit volume , the damping constant is given as $b = b_v + b_a + b_t$, which arises from viscous effects, acoustic effects and thermal damping, respectively. Then the attenuation coefficient A in dB per unit length can be given by [12]:

$$A = 20(log_{10}e)\frac{\omega v}{c} \approx 8.68589\frac{\omega v}{c} \tag{3.48}$$

where v is derived from $c/c_m = u - iv$.

3.2.3 A 3-D finite element model for a Hydro-Sound Damper

The hydro-sound damper is modelled as an air bubble surrounded by an elastic surface layer. The elastic material we use here is latex rubber, because it is one of the most widely used elastic materials for encapsulated air-bubbles. For the offshore environment, a stronger material is often used in order to avoid the explosion due to the large static pressure in deep water. Hydro-Sound Dampers of different radii are modelled in the comparison study with the open-ended resonator. The size of the hydro-sound damper will depend on the rigidity modulus of the material and the water depth. The PE-foam is not taken into account for this study. However, in the chapter 7, we will discuss the importance of the damping to the absorption of the energy from the sound waves.

Similar to the boundary and radiation conditions in the open-ended resonator model, the conditions are schematically depicted in the Figure 3.9.

We have the incident harmonic pressure wave with the applitude of 1 Pa equal tothe SPL as $117dB$ as we derived in Eq. (3.42).

Table 3.4: Material properties and geometrical parameters for Hydro-Sound Damper model

Parameter	Value	Unit	Description
d	1	m	Water depth
W_d	0.5	m	Y-Width of the fluid domain
H_d	0.5	m	Z-Height of the fluid domain
L_d	1	m	X-Length of the fluid domain
x_d	0	m	x location of the domain
ρ_w	1×10^3	kg/m^3	Density of water
c_w	1485	m/s	Speed of sound in the water
p_0	1	P_a	Incident wave pressure
θ	pi/2	rad	Angle of incident wave
k_x	0	-	x-wave propagation direction
k_y	sin(theta)	-	y-wave propagation direction
k_z	cos(theta)	-	z-wave propagation direction
P_a	1	atm	Absolute pressure /Atmosphere
ρ_a	1.225	kg/m^3	Density of air
ρ_b	1.476×10^3	kg/m^3	Density of latex bubble
c_a	343	m/s	Speed of sound in the air
E_b	9×10^5	P_a	Young's modulus
ν	0.5	-	Poisson ratio
G_s	$E_b/(2(1+\nu))$	P_a	Shear modulus
tt	1.6×10^{-3}	m	Thickness of rubber
x_0	0.2	m	x center coordinate
y_0	0.2	m	y center coordinate
z_0	0.2	m	z center coordinate
f_{min}	1	Hz	Minimum value for frequency sweep
f_{max}	300	Hz	Maximum value for frequency sweep

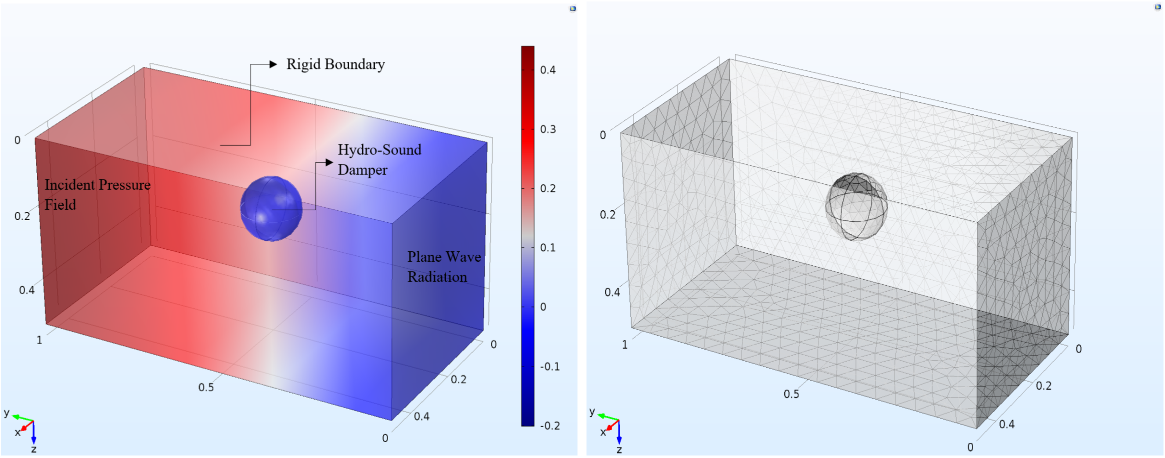

(a)

(b)

Figure 3.9

3.2.4 Results and discussion

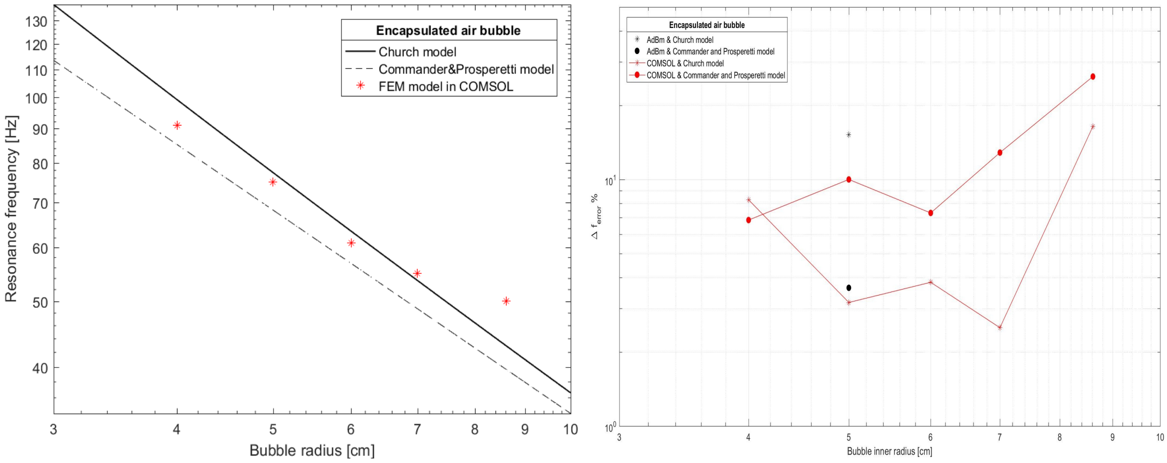

(a)

(b)

Figure 3.10: Comparison results between analytical solutions and numerical solutions for the encapsulated air-bubbles with different radius.

For encapsulated air-bubble, Church model and Commander and Prosperetti model were considered in order to compare with FEM model in COMSOL Multiphysics. The thickness of the bubble is chosen equal to 1mm. Figure 3.10 in logarithm scale shows a comparable agreement between the analytical solution and the numerical solution, meaning that the acoustic behavior is well predicted by both models.

The errors between the numerical solutions and the analytical solutions can be defined as:

$$\Delta f_{error} = \frac{|f_{analytical} - f_{numerical}|}{f_{numerical}} \tag{3.49}$$

As shown in Figure 3.10, Δf_{error} shows that the deviation is within the acceptable margin.

Therefore, both Church model and Commander and Prosperetti model can be proven to be accurate on the basis of the discussions above.

The attenuation of the various resonators is not considered in this section. The derivation of the attenuation coefficients of the resonators will require an accurate description on the boundary conditions, radiation conditions and the sound source as well. Therefore, we need to build an analytical model for the complete field containing resonators and noise source. In order to build a more generic model for various resonators and for the purpose of developing an optimal parameter design for the resonator-based noise mitigation system, we need to find the frequency response function for the acoustic behaviour of the resonator. We will discuss how to derive the transfer function for an open-ended resonator in the next section. The method also can be applied to the other resonators, the behaviour of which can be approximated by the theory of SDoF oscillators.

3.3 Frequency response function

In order to describe the acoustic behaviour of the resonators, we need to derive the frequency response function, which is defined as:

$$\mathbf{X}(\vec{r},\omega) = \mathbf{H}(\omega) \cdot \mathbf{P}(\vec{r},\omega) \tag{3.50}$$

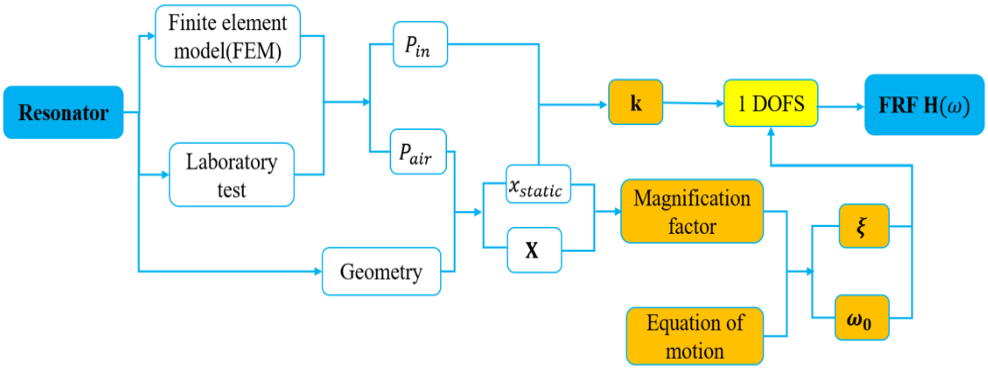

Figure 3.11: The derivation of frequency response fuction

Then given the pressure applied on the the resonator, we could obtain the motion of the resonator in frequency domain. For a single resonator simulated in software package COMSOL, we could describe the performance of the resonator by comparing it with an analogous single-degree-of-freedom system. Because this study mainly focuses on low frequency sound waves generated by pile driving, the water column in the resonator can be treated as a point mass. Therefore, one can assume that the pressure on the opening end of the resonator is equally distributed.

By extracting the average pressure on the air-water interface in the resonator computed in COMSOL, we could derive the displacement amplitude based on the ideal gas law for an adiabatic process. When the displacement amplitude - frequency characteristic is determined, the frequency response function can be found by extracting the coefficient from the analogous mass-spring-dashpot system, which can be used to develop the analytical model for the whole resonator system.

3.3.1 Equation of motion

It is assumed that there are M resonators located at the point $\vec{r}_1^R, \vec{r}_2^R, ..., \vec{r}_M^R$. For a single resonator of mass m, the water column is simplified as a lumped mass and its motion follows the Newton's second law as follows:

$$m\ddot{x}_m^R(t) + c\dot{x}_m^R(t) + kx_m^R(t) = -p(\vec{r}_m^R, t)A_m^R \tag{3.51}$$

where $x_m^R(t)$ is the particle displacement, A_m^R is the cross sectional area of the opening end, $p(\vec{r}_m^R, t)$ is the average sound pressure over the opening area, which is assumed positive when it points towards the fluid domain.

Applying Fourier Transform to Eq. (3.51) we obtain:

$$(-\omega^2 m + i\omega c + k)\tilde{x}_m^R(\omega) = -\tilde{p}(\vec{r}_m^R, \omega)A_m^R \tag{3.52}$$

where the tilde denotes a quantity in frequency domain. The frequency-time Fourier transform pair we use in this study is:

$$f(t) = \frac{1}{2\pi}\int_{-\infty}^{\infty} f(\omega)e^{i\omega t}d\omega \tag{3.53}$$

$$f(\omega) = \int_{-\infty}^{\infty} f(t)e^{-i\omega t}dt \tag{3.54}$$

Thus, $\tilde{x}_m^R(\omega)$ can be expressed by the pressure at the opening end as:

$$\tilde{x}_m^R(\omega) = \frac{-\tilde{p}(\vec{r}_m^R, \omega)A_m^R}{-\omega^2 m + i\omega c + k} \tag{3.55}$$

or alternatively,

$$\tilde{x}_m^R(\omega) = \frac{-A_m^R}{-\omega^2 + 2i\xi\omega\omega_n + \omega_n^2} \cdot \frac{\omega_n^2}{k} \cdot \tilde{p}(\vec{r}_m^R, \omega) \tag{3.56}$$

In the equation above, the term $(-A_m^R\omega_n^2)/k(-\omega^2+2i\xi\omega\omega_n+\omega_n^2)$ can be determined by finding the proper value of ξ, ω_n and k. This will be obtained when the pressure - displacement relation and the pressure spectrum are known.

3.3.2 Ideal gas law

Given ideal gas law, we know that the absolute pressure exerted by a given mass of an ideal gas is inversely proportional to the volume to the power γ, provided that the process is adiabatic and the amount of gas remain constant. For air, we can approximately choose γ being equal to 7/5. Hence, the displacement of the water column in the resonator can be derived by:

$$P_0V_0^{7/5} = |\widetilde{P}_{air}|(V_0 + \Delta V)^{7/5} \tag{3.57}$$

$$P_0V_0^{7/5} = |\widetilde{P}_{air}|(V_0 - |\widetilde{X}|A)^{7/5} \tag{3.58}$$

$$|\widetilde{X}| = \frac{V_0}{A}(1 - [\frac{P_0}{|\widetilde{P}_{air}|}]^{5/7}) \tag{3.59}$$

in which $\widetilde{X}(\omega)$ is the displacement amplitude, P_0 is the underwater static pressure (which is equal to $\rho_w gh + 1[atm]$) and V_0 is the corresponding initial air volume, $|\widetilde{P}_{air}|$ is the average absolute pressure at the air - water interface, which consist of P_0 and p'. In the finite element model in COMSOL, P_0 is used as the background pressure.

In ideal mass-spring-dashpot system, we could read out the static displacement $\tilde{x}_{static}$ from X - intercept when frequency approaches zero. Thus, we could obtain the dynamic amplification factor for the displacement as:

$$|\frac{\widetilde{X}}{\tilde{x}_{static}}| = G(\omega) \tag{3.60}$$

$$= ((1-\frac{\omega^2}{\omega_n^2})^2 + 4\xi^2\frac{\omega^2}{\omega_n^2})^{-\frac{1}{2}} \tag{3.61}$$

in which the factor $G(\omega)$ for single-degree-of-freedom-system has a well-known solution.

The term on left side of the equation is what we could obtain from the COMSOL simulation. While the term on the right side of the equation needs to be determined by finding the proper parameters. Through curve fitting procedure in matlab, we could achieve this directly.

In order to fit the two terms, the least-squares method is applied as:

$$\min(f_1(x)^2 + f_2(x)^2 + f_3(x)^2 + ... + f_N(x)^2) \tag{3.62}$$

Using nonlinear least-squares solver, we could find the unknowns in the function which best fits the data from COMSOL, the results will be shown in the next section. This equivalence provides the two vital parameters to determine the frequency response function, which is the damping ratio ξ and the natural frequency ω_n.

Then, we could determine the stiffness coefficient and the point mass. Given the input pressure P_{in}, we have:

$$k = \frac{F}{\tilde{x}_{static}} \tag{3.63}$$

$$= \frac{P_{in}A_m^R}{\tilde{x}_{static}} \tag{3.64}$$

Hence, the frequency response function can be computed as:

$$H(\omega) = \frac{-A_m^R}{-\omega^2 + 2i\xi\omega\omega_n + \omega_n^2} \cdot \frac{\omega_n^2}{k} \tag{3.65}$$

Using the frequency response function $H(\omega)$ and the excitation from the pressure at the point of resonator , the displacement amplitude at the neck of the resonator can be obtained as:

$$\widetilde{X} = H(\omega) \cdot \tilde{p}(\vec{r}_m^R, \omega) \tag{3.66}$$

3.3.3 Result and discussion

The derivation of the frequency response function(or transfer function) needs to follow the main three steps through the numerical simulation. In reality, the system parameters can

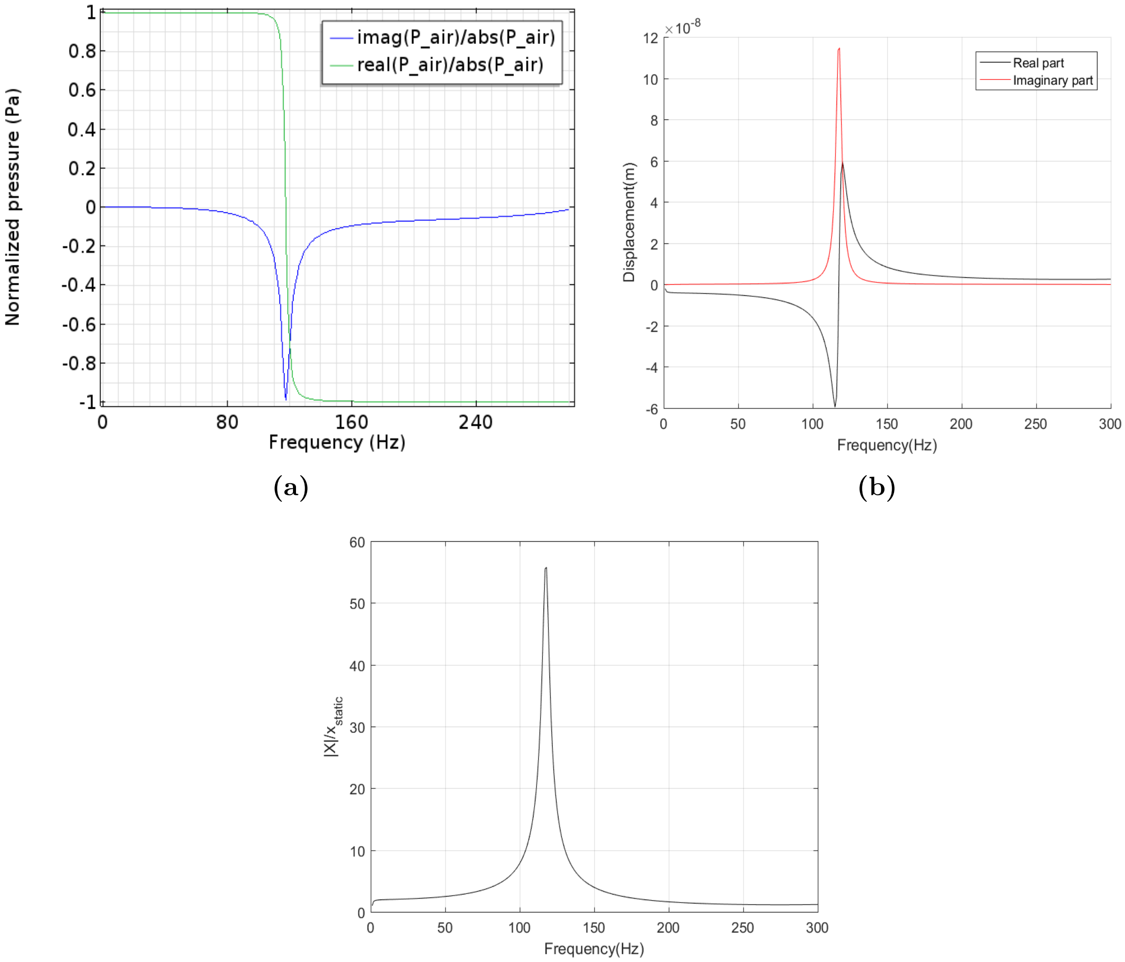

(a) **(b)**

(c)

Figure 3.12: Compute the magnification factor from the pressure data in COMSOL

be derived from experiment tests as well. And the results from the numerical model (i.e. COMSOL Multiphysics) also need to be verified through experiment in order to determine the damping coefficient for certain material.

The first step of deriving the FRF is to obtain the pressure at the air-water interface from the COMSOL simulation. Given the pressure applied on the air-water interface, we could plot the relation between the P_{air} and frequency as shown in Figure 3.12 (a). The obtained complex-valued results show that the phase shift take place at the resonance frequency.

Through ideal gas law, we obtain the relation between the displacement amplitude of the water column and the pressure at the air-water interface. Based on the relation, the displacement amplitude can be derived as shown in Figure 3.12 (b). Therefore, we could derive the magnification factor based on the numerical results from COMSOL in Figure 3.12 (c).

The second step of deriving the FRF is to find the appropriate parameter, damping ratio ξ and natural frequency ω_n by fitting the numerical results from COMSOL model as shown in Figure 3.13.

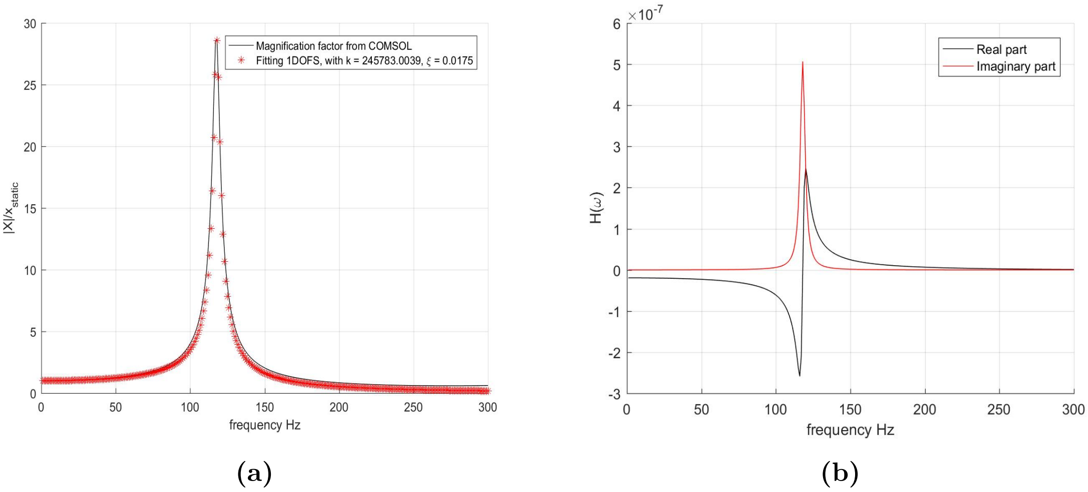

(a) **(b)**

Figure 3.13: Fitting the line and compute Frequency Response Function

Finally, by substituting the critical parameters back into the expression for the frequency response function, now we could obtain the FRF for individual resonator. The results also show that the mass we derived from the fitting have a good agreement with the mass of water column in the resonator, which also confirm our assumption that the resonator works as a linear SDoF system.

Chapter 4

Qiu Resonator

Based on the previous study of the existing resonator-based noise mitigation systems, a new structure called "*Qiu*" resonator is proposed, which aims to make the deployment of the resonator system easier and be able to handle marine environment. Thus, the *Qiu* resonator exploits a layer of membrane to encapsulate the air in the resonator. By using a layer of rigid shell on the outer surface, it makes the resonator more robust and durable.

To have a better understanding of the acoustic performance of the *Qiu* resonator, a finite element model was built in COMSOL Multiphysics. The parametric study was used to investigate the dominating factors for this new technique. Based on the results of this preliminary study, some recommendations for the existing noise mitigation techniques are made.

This study does not aim to propose the most optimal design of underwater resonators, but to provide one possibility of many potential designs. In order to achieve the "optimal" design, a 3-D acoustically coupled noise reduction prediction model is developed by the author, which could find the optimal parameters of the resonator and to improve the design of existing systems. This will be discussed further in Chapter 6 and 7.

4.1 Modelling method

4.1.1 Geometry

The model was created in COMSOL and exercised over a range of parameters. The resonator consists of an outer shell, cylindrical inlet and an inner ball made from rubber (schematically depicted in Figure 4.1). The resonator is acoustically coupled to the waveguide driven by a harmonically oscillating plane pressure wave $p_0(t) = p_0 e^{i\omega t}$ at the inlet of the domain.

The air is encapsulated in the interlayer by the outer shell and inner rubber ball. Because the air can be seen as weightless in this case (its mass is considerably less compared to the water mass), it works as the spring element in the ideal SDoF system as shown in Figure 4.1. In this study, the focus is placed on the pressure waves in the low-frequency range, i.e. $< 300Hz$.

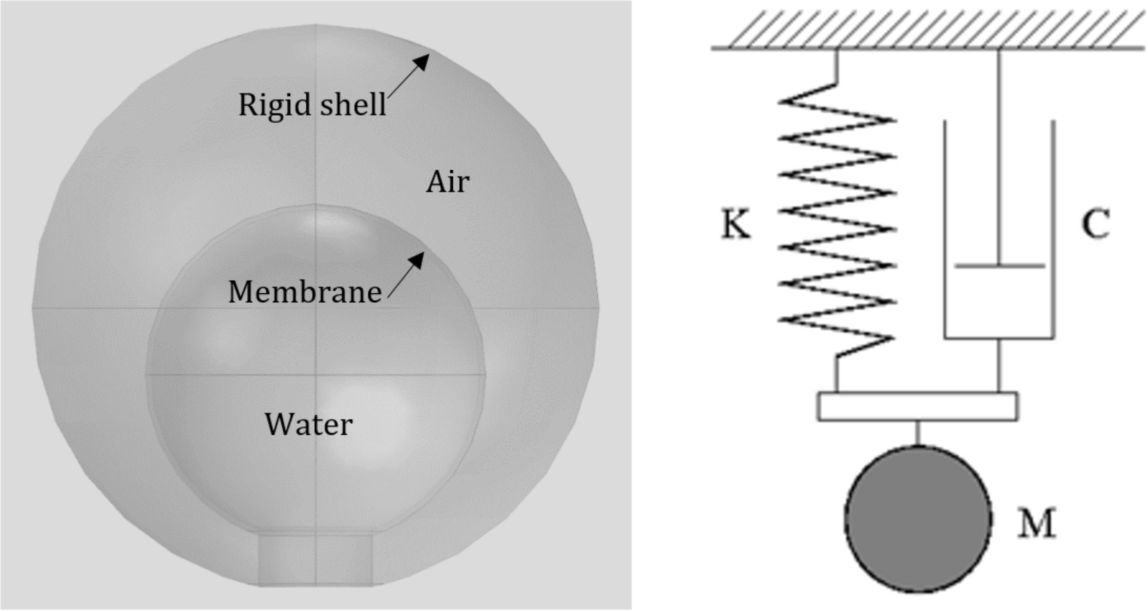

Figure 4.1: *Qiu* Resonator

So, the wave lengths are much longer ompared to the size of the resonator. The water filled inner ball can act as the point mass in the system excited by the oscillating pressure at the inlet. The membrane is used for enclosing the air and is flexible enough to allow the water to move as freely as possible. With the use of a membrane, the deployment of the resonator system can be simple and convenient compared to the open-ended resonator. Note that the model is defined by a series of geometric parameters. This makes it easy to quickly include parametric sweeps in the geometry, which could be used to tune the resonator to the target frequency. In this study, the generated pressure field for different resonator configurations is analysed. The inner rubber ball is defined as a hyperelastic membrane in which nonlinear behaviour dominates.

4.1.2 Model Solvers

The Pressure Acoustics, Frequency Domain interface is used to compute the pressure variation for the propagation of acoustic waves in fluids at quiescent background conditions. It is suited for this frequency-domain simulation with harmonic variations of the pressure field.

The physics interface can be used for linear acoustics described by a scalar pressure variable. It includes domain conditions to model losses in a homogenised way. Domain features also include radiation conditions, incident acoustic fields, as well as domain monopole and dipole sources. In this study, the plane wave radiation of the acoustic waves is used into this model, and an incident pressure field is added on the inlet boundary.

The Frequency Domain solver, solves the situation in which the acoustic domain is subjected to harmonic excitation at a set of specified excitation frequencies. While this can be time-consuming for larger frequency sweeps, the numerical solution is calculated explicitly at every frequency. So the solutions obtained by this solver can always be expected to be correct by assuming convergence of the model and appropriate meshing.

4.1.3 Mesh

It is widely accepted that the element size in element-based acoustic computations should be related to the wavelength. The idea of using a fixed number of elements per wavelength is most likely a consequence of Shannon's sampling theorem. This theorem is of fundamental importance in vibration and acoustics for experimental measurements and frequency detection. As a commonly applied rule of thumb, at least five quadratic elements should be used to capture accurately each wave length. Therefore, the maximum mesh size is set to 1/5 of the shortest wavelengths present, $\lambda_{water} = c_{water}/f_{max}$ or $\lambda_{air} = c_{air}/f_{max}$.

4.2 Model description and governing equations

4.2.1 Fluid domain

In reality, the ocean environment consists of different layered media with properties that change abruptly at the seabed level while the sound speed varies more or less continuously in the water column. However, in this study we simplify the ocean environment to a homogeneous fluid domain as shown in Figure 4.2 in order to focus on the behaviour of a single resonator element. The homogeneous layer is bounded by four rigid boundaries and two radiation boundaries. On the inlet boundary, the waveguide is exposed to a series of harmonically oscillating pressures over a frequency range. Sound leave the domain freely from the outlet boundary.

The environmental body forces such as gravity and magnetism are of no significance to acoustic propagation except for the effect of gravity on the sound speed variation in depth [18]. In this study, we assume that the sound speed is constant over depth as $1500 m/s$. The only body forces of importance are the acoustic sources.

Pressure Acoustic frequency domain interface was used for the entire domain, except for the membrane, which is defined on the boundary of the inner rubber ball. This interface is perfectly used to compute the pressure variation for the propagation of the acoustic waves in the quiescent fluid domain. The pressure acoustic interface solves the Helmholtz equation in the frequency domain for a given frequency.

$$\nabla(\frac{1}{\rho}(\nabla p_t)) - \frac{k^2 p_t}{\rho} = Q_m \tag{4.1}$$

in which $with \quad p_t = p + p_b, \quad k = |\mathbf{k}| = \frac{\omega}{c}$. The sound pressure p represents the acoustic variation or excess pressure. Based on the assumption of no fluid flow, the ambient pressure is the static absolute pressure, p_b is the background acoustic pressure. The total pressure p_t is the sum of the excess pressure p, i.e. dynamic component, and the background pressure p_b.

In this study, we simplify the waveguide to be bounded by four rigid boundaries while the

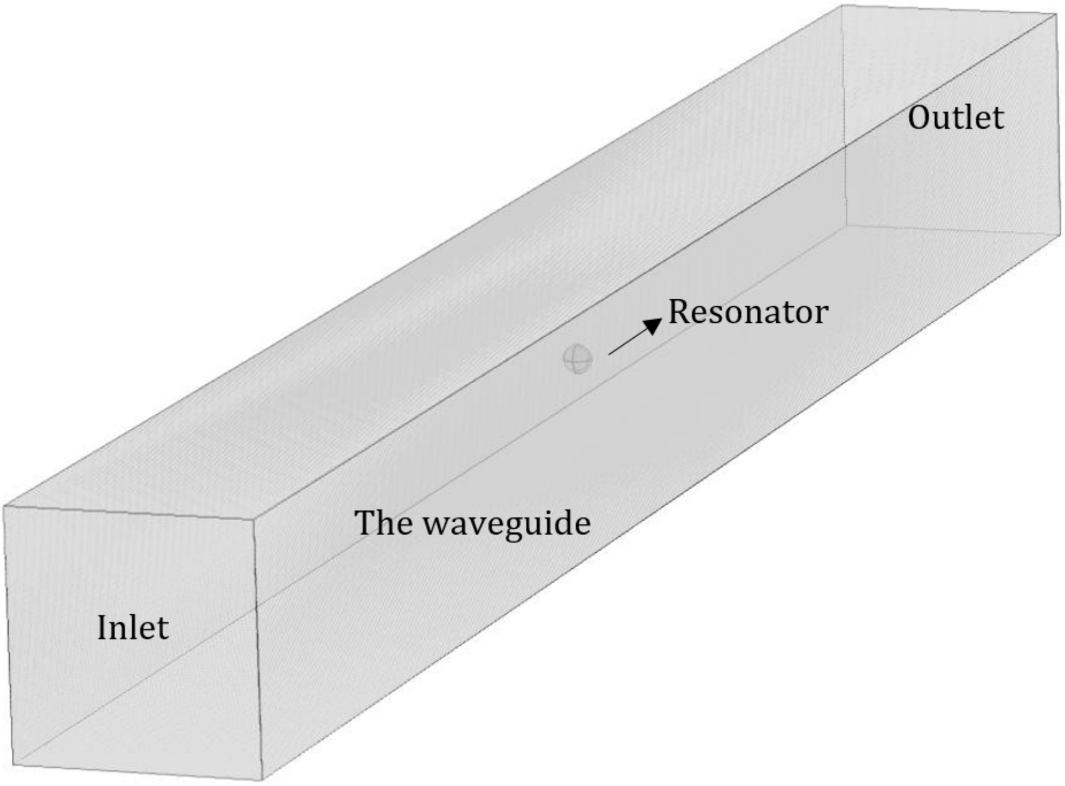

Figure 4.2: Geometry of the model

plane wave radiation condition is applied to the outlet boundaries and an incident pressure field is added on the inlet. This implies the following boundary conditions for the fluid domain:

1. Rigid boundary condition at four faces parallel with the waveguide, a Neumann boundary condition is imposed as:
$$\frac{\partial p}{\partial n} = 0 \tag{4.2}$$
2. Outlet boundary condition: Plane wave radiation condition allows an outgoing plane wave to leave the modelling domain with minimal reflections when the angle of incidence is near to normal. The second-order radiation boundary conditions in the frequency domain are defined below:
$$-n(-\frac{1}{\rho}(\nabla p_t)) + i\frac{k}{\rho}p + \frac{i}{2k\rho}\Delta_T p = n(\frac{1}{\rho}(\nabla p_i)) + i\frac{k}{\rho}p_i + \frac{i}{2k\rho}\Delta_T p_i \tag{4.3}$$
in which Δ_T at a given point on the boundary denotes the Laplace operator in the tangent plane at that particular point.
3. Inlet boundary condition, an incident pressure field is added on one of the plane wave radiation boundaries as:
$$p_i = p_0 e^{-i\mathbf{kr}} \tag{4.4}$$
where p_0 is the wave amplitude, $\mathbf{k}$ is the wave vector and $\mathbf{r}$ is the location of the boundary.

4.2.2 *Qiu* resonator

The *Qiu* resonator is modelled by together using membrane and pressure acoustics in the frequency domain. The outer rigid shell is defined by an interior sound hard boundary in pressure acoustics node, and the inner rubber sheet is defined as linear elastic material or hyperelastic material in membrane node. The hyperelastic material subnode adds the equations for hyper-elasticity at large strains. Hyperelastic materials can be suitable for modelling rubber and other polymers. This material is available in the Solid Mechanics and Membrane interfaces. By using Mooney-Rivlin model for the rubber, the model parameters $C10$ and $C01$, the initial bulk modulus κ are determined based on the rubber material.

This implies the conditions for the resonator boundaries as the following:

1. Rigid shell: the Interior Sound Hard Boundary adds a boundary condition for a sound hard boundary or wall on interior boundaries. This implies the normal component of the acceleration is zero:
$$\nabla(\frac{1}{\rho}(\nabla p_t))_1 = 0 \tag{4.5}$$
$$\nabla(\frac{1}{\rho}(\nabla p_t))_2 = 0 \tag{4.6}$$
where the subscripts 1 and 2 represent the two sides of the boundary.
2. Membrane: For a linear elastic material, Hooke's law relates the stress tensor to the elastic strain tensor. While for hyperelastic material, nonlinear behaviour will dominate. This condition could be defined under membrane node with different material parameters.

4.2.3 Multiphysics Interfaces

The Multiphysics interface was defined as acoustic-structure boundary coupling. The coupling includes the fluid load on the structure and the structural acceleration as experienced by the fluid. For thin interior structures like shells or membranes with fluid on both sides, a slit is added to the pressure variable and care is taken to couple the interior and exterior sides. This mathematically implies the boundary conditions as:

1. Interior boundary: the acoustic load is given by the pressure drop across the thin membrane as

$$-n\cdot(-\frac{1}{\rho}(\nabla p_t))_1 = n\cdot u_{tt} \tag{4.7}$$

$$-n\cdot(-\frac{1}{\rho}(\nabla p_t))_2 = -n\cdot u_{tt} \tag{4.8}$$

$$F_A = (p_{t,1} - p_{t,2})\cdot n \tag{4.9}$$

   where u_{tt} is the structural acceleration, n is the surface normal, p_t is the total acoustic pressure and F_A is the unit load on the membrane.

2. Exterior boundary condition reads:

$$-n\cdot(-\frac{1}{\rho}(\nabla p_t)) = -n\cdot u_{tt} \tag{4.10}$$

$$F_A = p_t\cdot n \tag{4.11}$$

4.3 Parametric Study of the *Qiu* resonator

In this section, the response of the resonator and the generated wave field are analysed for a given incident pressure field. The set of material properties and geometric parameters are shown in Table 4.1. The water depth, opening radius and membrane thickness are considered separately for determining the behaviour of the resonator. For design purposes, the target resonance frequency and noise reduction for varying parameters are investigated in this study.

The incident Sound Pressure Level in this section is the same as Eq. (3.42).

4.3.1 Influence of the water depth of the resonator

Assume that in initial condition there is no pressure difference on the two side of membrane, both under 1 atm. Given the following conditions:

$$P_0 = 1atm = 1\times 10^5 P_a \tag{4.12}$$

$$P_{in} = P_{water} = \rho_w g h + P_0 \tag{4.13}$$

$$P_{out} = P_{air} = \rho_a(r)\cdot R\cdot T \tag{4.14}$$

Table 4.1: Material properties and geometrical parameters

Parameter	Value	Unit	Description
d	1	m	Water depth
W_d	1	m	Y-Width of the fluid domain
H_d	1	m	Z-Height of the fluid domain
L_d	1	m	X-Length of the fluid domain
x_d	0	m	x location of the domain
ρ_w	1×10^3	kg/m^3	Density of water
c_w	1485	m/s	Speed of sound in the water
p_0	1	P_a	Incident wave pressure
θ	pi/2	rad	Angle of incident wave to y positive direction
k_x	0	-	x-wave propagation direction
k_y	sin(theta)	-	y-wave propagation direction
k_z	cos(theta)	-	z-wave propagation direction
T	293.25	K	Temperature
P_a	1	atm	Absolute pressure /Atmosphere
R_o	0.10	m	Outer radius
R_i	0.04	m	Inner radius
L_s	0.01	m	Depth of indentation
dd	0.02	m	Open ended radius
x_0	0.2	m	x center coordinate
y_0	0.2	m	y center coordinate
z_0	0.2	m	z center coordinate
ρ_a	1.225	kg/m^3	Density of air
ρ_b	1.1×10^3	kg/m^3	Density of latex bubble
c_a	343	m/s	Speed of sound in the air
E_b	9×10^5	P_a	Young's modulus
ν	0.5	-	Poisson ratio
G_s	$E_b/(2(1+\nu))$	P_a	Shear modulus
tt	1×10^{-3}	m	Thickness of rubber
f_{min}	1	Hz	Minimum value for frequency sweep
f_{max}	500	Hz	Maximum value for frequency sweep

Table 4.2: Parametric sweep for various water depth

Case	Outer Radius (cm)	Inner Radius (cm)	Water depth (m)
1	10	8.38	10
2	10	8.58	20
3	10	8.71	30
4	10	8.81	40

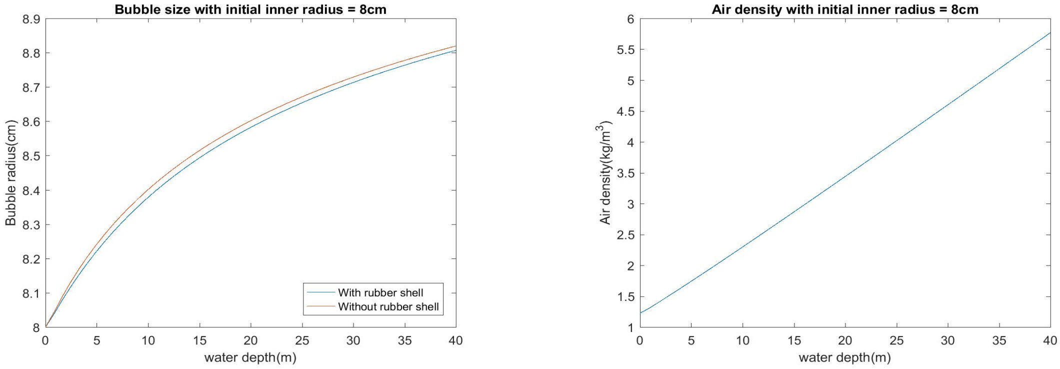

(a) Bubble radius **(b)** Air density

Figure 4.3: Bubble radius and air density change with water depth

where R is specific gas constant, for dry air R is equal to 287 $J/(K{\cdot}kg)$, T is the temperature in the unit of K. We could assume the temperature is 10 °C that is 283 K.

$$P_{in} = P_{out} + P_B \tag{4.15}$$
$$P_{water} = P_{air} + P_B \tag{4.16}$$
$$P_B = P_{water} - P_{air} \tag{4.17}$$

With the increase of water depth Z, three terms will increase respectively. At the same time, P_B also satisfy the following condition:

$$P_B(r) = 2s_1\frac{d_0}{r_0}(\frac{r_0}{r} - (\frac{r_0}{r})^7)(1 - \frac{s_1}{s_{-1}}(\frac{r}{r_0})^2) \tag{4.18}$$

Thus, we could obtain the relation with two variables r and z as:

$$P_B(r) = P_{water}(z) - P_{air}(r)$$

By iteration both right term and left term, we could reach the equilibrium at a given water depth and find the exact radius satisfying the upper equation. The results for the cases examined here are summarised in Table 4.2.

From Figure 4.3a, we know that the size of rubber bubble changes with water depth, which could result in depth-dependent resonance frequency and behaviour. The density of air increases with water depth also shown in Figure 4.3b.

Table 4.3: Parametric sweep for various opening radius

Case	Opening Radius (cm)	Outer Radius (cm)	Inner Radius (cm)	Water Volume (m^3)	Air Volume (m^3)
1	1	5	4	2.48×10^{-4}	2.23×10^{-4}
2	2	5	4	2.48×10^{-4}	2.23×10^{-4}
3	2.5	5	4	2.48×10^{-4}	2.23×10^{-4}
4	3.5	5	4	2.48×10^{-4}	2.23×10^{-4}

Table 4.4: Parametric sweep for various thickness of membrane

Case	Membrane thickness (m)
1	5×10^{-4}
2	1×10^{-3}
3	2×10^{-3}
4	5×10^{-3}

4.3.2 Influence of the opening radius of the resonator

The opening radius have influence on the behaviour of the resonator by changing the contact area with the incoming waves and the motion of the inner water column. The chosen parameters are shown in Table 4.3. By changing the opening radius, the water volume, air volume and other parameters remain same. In this study, there are multi-peaks of resonance frequency with the increasing of the opening radius. The reason might be due to the fact that by increasing the opening area, the system no longer works as single degree of freedom system, thus multiple peaks appear in the computed frequency range.

In this study, the incident SPL is the 117 dB. In order to compare performance of the system for different opening radius, we kept the water and air volume constant by keeping outer and inner radius unchanged. Some damping is also included on the membrane to eliminate the multiple peaks in the frequency response function. The results, which are summarised in Figure 4.4, show that with the increase of the opening radius, the contact area with the incident pressure increase.

4.3.3 Influence of the membrane thickness of the resonator

The membrane works with air-volume together as spring in an ideal SDoF system. This is a critical parameter in the determination of the resonance frequency and the attenuation. Different thicknesses are investigated, while the material properties and the other geometrical parameters remain unchanged. With the increase of the thickness of the membrane, the resonance frequency shift to higher values and the attenuation significantly increases for a thicker membrane. The results in both linear and logarithmic scales are shown in the Figure 4.5.

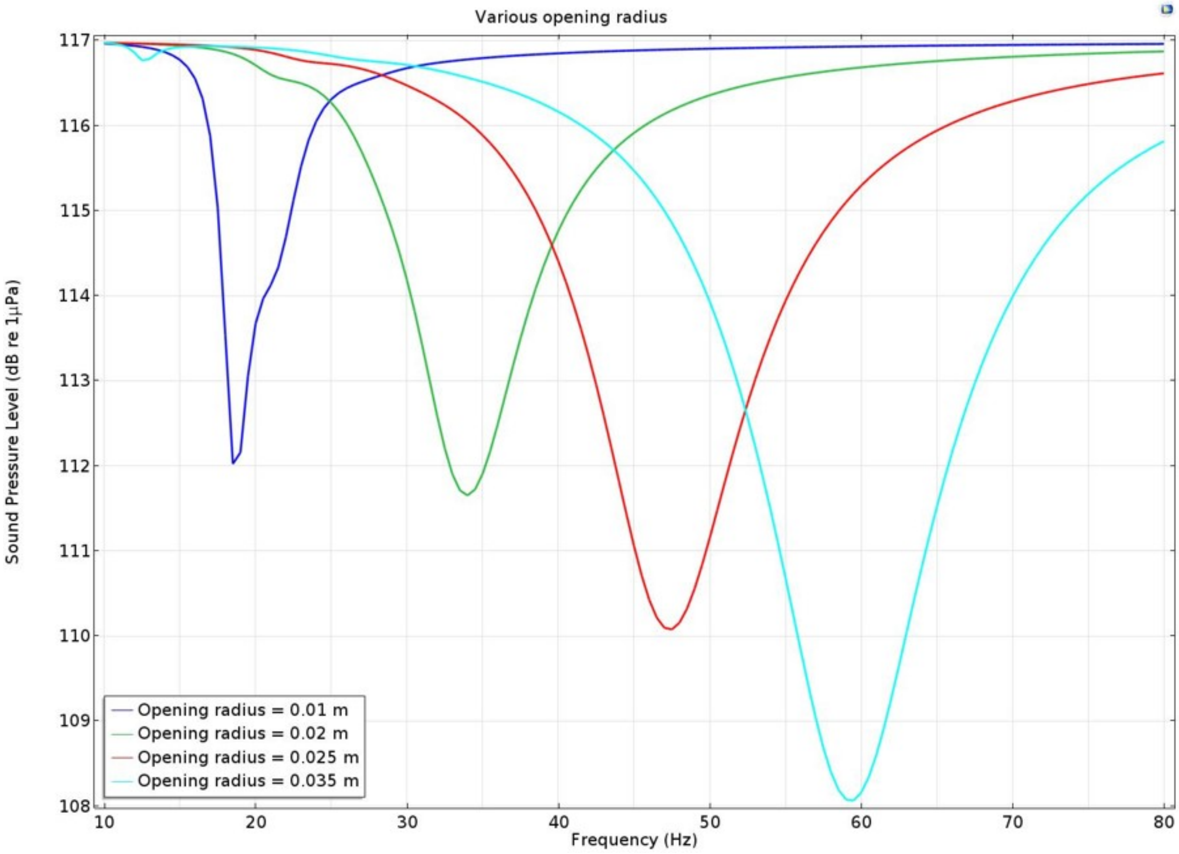

Figure 4.4: Sound Pressure Level(dB re $1\mu P_a$) as function of frequency on logarithmic scales for various opening radius 0.01m, 0.02m, 0.025m and 0.035m.

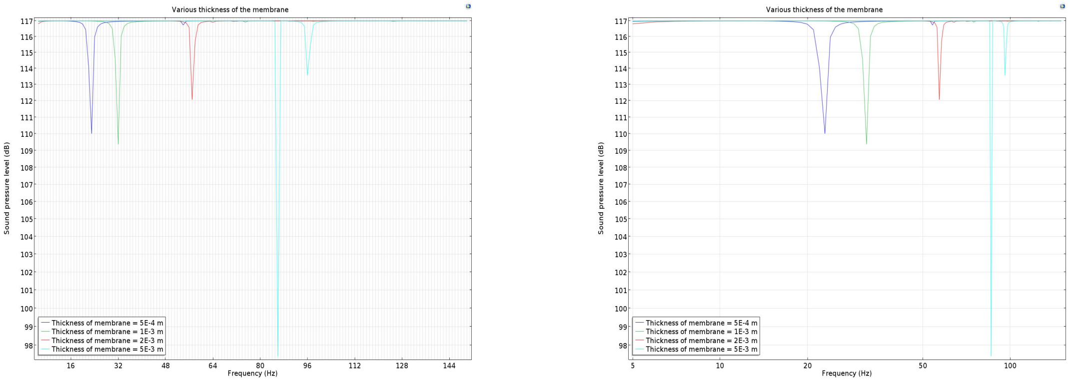

(a) linear scales **(b)** logarithmic scales

Figure 4.5: Sound Pressure Level(dB re $1\mu P_a$) as function of frequency for various membrane thickness 5E-4m, 1E-3m, 2E-3m, 5E-3m.

4.4 Conclusion and recommendations

In this chapter, we developed a new type of resonator, named *Qiu* resonator. This technique could absorb the energy into oscillating the resonator by using the resonance effect. Different from the open-ended resonator, the air is encapsulated by a layer of membrane by using hyperelastic materials. In this configuration, the resonance frequency does not depend solely on the air and water columns. The material of the membrane and the opening-end of the radius can also influence the behaviour of the *Qiu* resonator.

Based on the parametric study in this section, the following conclusions are drawn:

- Opening radius influences both noise reduction and resonance frequency. The contact surface area between the resonator and the incident waves increase with the opening radius. This could physically cause the increase of the noise reduction level. The reason of the change of the resonance frequency will need further investigation.
- Based on the configuration, we could find the resonant frequency can be tuned through the ratio of air and water volumes. With the increase of the air volume, the stiffness of the air column is reduced, and the resonance frequency shift to the lower values; with the increase in the water volume, the SDoF mass is increasing, which results in the decrease of the resonance frequency. The influence of the water depth is similar to the air volume; in deeper water, the air density increases, the stiffness of the air also increases, which makes the resonance frequency to rise.
- The behaviour depends also on the material properties of the membrane: by using a thicker layer, the resonance frequency can increase, this is physically attributed to the higher stiffness of the system. By adding the damping in the membrane, noise reduction is less efficient. However, a relatively broad band of attenuation is achieved.

Chapter 5

3-D cylindrically symmetric sound propagation model

To find the optimal properties of an underwater resonator, to be compatible with the different resonator-based systems and to optimise the design of the existing techniques, we develop a 3-D acoustically coupled prediction model for the noise reduction by the application of a resonator-based noise mitigation system. This model would require an accurate description of the noise source, the resonators and the waveguide. Because this study focuses on the behaviour of the resonators, we could simplify the model by using a point source or line source to replace the actual noise source.

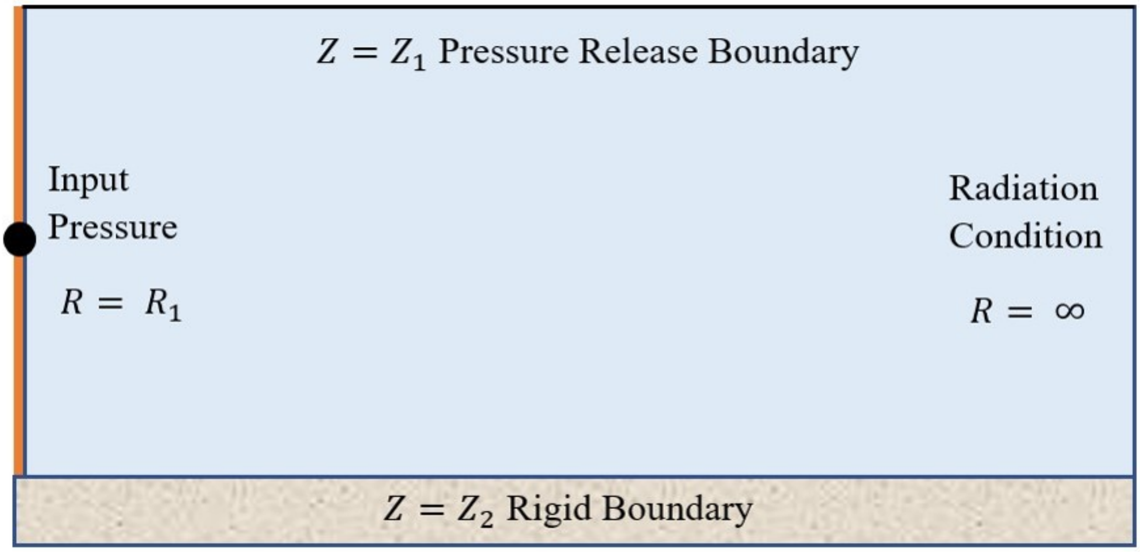

Figure 5.1: The waveguide for 3-D cylindrically symmetric point source and line source field

Hence, a 3-D cylindrically symmetric sound propagation model is proposed by the author first to describe the noise source, which is schematically depicted in Figure 5.1. In order to describe the point source in the waveguide, the Green's function is composed, which satisfies the pressure release boundary, rigid boundary and radiation conditions. The solution can be verified through finite element model in COMSOL Multiphysics by comparing the distribution of pressure field in the form of the sound pressure level in the frequency domain. The validation of the model for a line source is also presented in this section.

5.1 Governing eqaution

The homogeneous wave equations describe the motion of the fluid for the free field regarding velocity potential and displacement potential as the following equation,

$$\nabla^2\phi(r,z,t) - \frac{1}{c^2}\frac{\partial^2\phi(r,z,t)}{\partial t^2} = 0 \tag{5.1}$$

$$\nabla^2\psi(r,z,t) - \frac{1}{c^2}\frac{\partial^2\psi(r,z,t)}{\partial t^2} = 0 \tag{5.2}$$

in which $\phi(r,z,t)$ is the velocity potential, $\psi(r,z,t)$ is the displacement potential, $p(r,z,t)$ is the pressure, c is the sound speed at the fluid domain and ∇^2 is the Laplacian operator defined in the cylindrical coordinate system. We assume the sound speed and density of the water constant over the water depth.

The dimension of the wave equation can then be reduced by the use of the frequency-time Fourier transform pair,

$$f(t) = \frac{1}{2\pi}\int_{-\infty}^{\infty}\tilde{f}(\omega)e^{i\omega t}d\omega \tag{5.3}$$

$$\tilde{f}(\omega) = \int_{-\infty}^{\infty} f(t)e^{-i\omega t}dt \tag{5.4}$$

leading to the Helmholtz equation, or frequency domain wave equation, in which $f(t)$ is understood here as the examined quantity, i.e. the pressure of the fluid.

$$\nabla^2\tilde{\phi}(r,z,\omega) + k^2\tilde{\phi}(r,z,\omega) = 0 \tag{5.5}$$

$$\nabla^2\tilde{\psi}(r,z,\omega) + k^2\tilde{\psi}(r,z,\omega) = 0 \tag{5.6}$$

$$\nabla^2\tilde{p}(r,z,\omega) + k^2\tilde{p}(r,z,\omega) = 0 \tag{5.7}$$

with $k^2 = \omega^2/c^2$. From linearized Euler equations, we obtain the following expression for the pressure, velocity and displacement in terms of velocity potential and displacement potential,

$$p(r,z,t) = -\rho_w\frac{\partial\phi}{\partial t} = -\rho_w\frac{\partial^2\psi}{\partial t^2} \tag{5.8}$$

$$\vec{\mathbf{v}} = \nabla\phi \tag{5.9}$$

$$\vec{\mathbf{u}} = \nabla\psi \tag{5.10}$$

In frequency domain, the velocity and pressure fields are related to the scalar potential as follows:

$$\tilde{p}(r,z,\omega) = -i\omega\rho_w\tilde{\phi}(r,z,\omega) \tag{5.11}$$

$$\tilde{\mathbf{v}} = \nabla\tilde{\phi}, with: \nabla = \frac{\partial}{\partial r}\hat{r} + \frac{\partial}{\partial z}\hat{z} \tag{5.12}$$

In Eq. (5.11), $\hat{r}$ and $\hat{z}$ define the unit vectors along the radial and vertical directions respectively. The tilde over the pressure, velocity, velocity potential and displacement potential denotes the complex amplitude in the frequency domain.

5.2 Boundary and Interface conditions

The fluid motion must satisfy the homogeneous Helmholtz equation, the radiation condition at infinity, the boundary condition at the sea surface, the seabed and the interface condition at the fluid-shell contact surface.

5.2.1 Perfectly Free Boundary

The free surface condition is an approximation for the surface boundary condition at $z = 0$. Although there is the atmosphere above the ocean, the impedance contrast is so large that there is no need for modelling the atmosphere. For acoustic medium this yields an Dirichlet boundary condition as:

$$\tilde{p}(r,z_1,\omega) = 0 \tag{5.13}$$

Thus, both velocity potential and displacement potential must vanish:

$$\tilde{\phi}(r,z_1,\omega) = 0 \tag{5.14}$$

$$\tilde{\psi}(r,z_1,\omega) = 0 \tag{5.15}$$

5.2.2 Perfectly Rigid Boundary

The bottom boundary condition assume that the seabed at $z = z_2$ is perfectly rigid, which leads to a Neumann boundary condition as:

$$\tilde{v}_z(r,z_2,\omega) = 0 \tag{5.16}$$

$$\frac{\partial\tilde{\phi}}{\partial z} = 0 \tag{5.17}$$

Although the acoustic impedance of the seabed can be measured, we assume the rigid bottom as an approximation for the boundary condition to simplify the simulation.

5.2.3 Radiation Condition

The radiation condition at $r \rightarrow \infty$ read:

$$\lim_{r\rightarrow\infty} r(\frac{\partial\tilde{\phi}}{\partial r} + ik\tilde{\phi}) = 0 \tag{5.18}$$

5.2.4 Interface Condition

The velocity of the fluid at the any radius $r = r_1$ can be obtained from a 3-D noise prediction model for offshore pile driving given by Tsouvalas(2015). Thus, we obtain both the velocity and pressure at the interface as:

$$\tilde{v}(r_1, z, \omega) = V_0 \tag{5.19}$$

$$\tilde{p}(r_1, z, \omega) = P_0 \tag{5.20}$$

5.3 The Green's function

The Green's function should inherently satisfy the sea surface and seabed boundary conditions, and the radiation conditions. By doing this, the Green's function could provide us the contribution of the pressure at field point (or receiver point) $\vec{r}$ from a simple point source at $\vec{r}_0$. Therefore, the critical issue here is to find the analytical solution for Green's function which satisfies the afore mentioned boundary conditions. The derivation for the solution to this problem is discussed as below.

5.3.1 The modal equation

We introduce the general Green's function as:

$$G_\omega(\vec{r}, \vec{r}_0) = g_\omega(\vec{r}, \vec{r}_0) + H_\omega(\vec{r}) \tag{5.21}$$

where $H_\omega(\vec{r})$ is any function satisfying the homogeneous Helmholtz equation as:

$$[\nabla^2 + k^2]H_\omega(\vec{r}) = 0 \tag{5.22}$$

The Green's function satisfying the same inhomegenous Helmholtz equation as the particular solution $g_\omega(\vec{r}, \vec{r}_0)$:

$$[\nabla^2 + k^2]G_\omega(\vec{r}, \vec{r}_0) = -\frac{\delta(r)\delta(z - z_s)}{2\pi r} \tag{5.23}$$

Using the technique of **separation of variables**, we seek a solution of the homogeneous equation in the form of:

$$H_\omega(\vec{r}) = \Phi(r)\Psi(z) \tag{5.24}$$

substituting the Eq. (5.24) into the Eq. (5.23),

$$\Psi(z)\frac{1}{r}\frac{d}{dr}(r\frac{d\Phi(r)}{dr}) + \Phi(r)\frac{d^2\Psi(z)}{dz^2} + k^2\Phi(r)\Psi(z) = 0 \tag{5.25}$$

All the partial derivatives have become ordinary derivatives and dividing through by $\Phi(r)\Psi(z)$ we find,

$$\frac{1}{\Phi(r)}[\frac{1}{r}\frac{d}{dr}(r\frac{d\Phi(r)}{dr})] + \frac{1}{\Psi(z)}[\frac{d^2\Psi(z)}{dz^2} + k^2\Psi(z)] = 0 \tag{5.26}$$

The contents in the square brackets are function of r and z, respectively. Thus, the only way the above equation can be satisfied is that each term is equal to a constant. Denoting this separation constant by k_{rm}^2, we obtain the modal equation from the function of z,

$$\frac{1}{\Psi_m(z)}[\frac{d^2\Psi_m(z)}{\partial z^2} + k^2\Psi_m(z)] = k_{rm}^2 \tag{5.27}$$

$$\frac{d^2\Psi_m(z)}{dz^2} + (k^2 - k_{rm}^2)\Psi_m(z) = 0 \tag{5.28}$$

$$\frac{d^2\Psi_m(z)}{dz^2} + k_{zm}^2\Psi_m(z) = 0 \tag{5.29}$$

$$with \quad \Psi(z_1) = 0 \quad \frac{d\Psi(z)}{dz}|_{z=z_2} = 0 \tag{5.30}$$

in which the vertical wavenumber $k_{zm} = \sqrt{k^2 - k_{rm}^2} = \sqrt{(\omega^2/c^2) - k_{rm}^2}$. The modal quation is a classical Sturm-Liouville eigenvalue problem. Thus we could obtain the following properties of this problem:

- The $\Psi_m(z)$ is an eigenfunction and k_{rm}^2 is an eigenvalue
- There are infinite number of eigenvalues
- $\Psi_m(z)$ can be normalized by:
$$\int_{z_1}^{z_2} \frac{\Psi_m^2(z)}{\rho(z)}dz = 1 \tag{5.31}$$
- The eigenfunctions corresponding to different eigenvalues are orthogonal:
$$\int_{z_1}^{z_2} \frac{\Psi_m(z)\Psi_n(z)}{\rho(z)}dz = 0 \tag{5.32}$$

The principle problem is now to solve the Eq. (5.27) for the normal modes $\Psi_m(z)$. The general solution is

$$\Psi_m(z) = A\sin(k_{zm}(z-0)) + B\cos(k_{zm}(z-0)) \tag{5.33}$$

From section 5.2.1, the pressure release boundary condition implies that $\tilde{p}(r, z_1, \omega) = 0$, so

$$\Psi_m(z_1) = 0 \tag{5.34}$$

This yields $B = 0$. And the bottom boundary condition at $z = z_2$ in section 5.2.2 leads to

$$\frac{\partial\Psi}{\partial z} = 0 \tag{5.35}$$

$$Ak_{zm}\cos(k_{zm}(z_2 - z_1)) = 0 \tag{5.36}$$

$$Ak_{zm}\cos(k_{zm}D) = 0 \tag{5.37}$$

with D being the water depth. Thus, either A is zero (the trivial solution) or we must have

$$k_{zm}D = (m - \frac{1}{2})\pi, \quad m = 1, 2, ... \tag{5.38}$$

Because the modes are normalized, we have the Eq. (5.31) that:

$$\int_{z_1}^{z_2} \frac{\Psi_m^2(z)}{\rho(z)} dz = 1 \tag{5.39}$$

$$\int_{z_1}^{z_2} \frac{[A\sin(k_{zm}(z-z_1))]^2}{\rho(z)} dz = 1 \tag{5.40}$$

$$\int_{0}^{D} \frac{[A\sin(k_{zm}z')]^2}{\rho(z')} dz' = 1 \tag{5.41}$$

Since we assume the density of the fluid constant over the water depth, $\rho(z) = \rho$, thus we can obtain that:

$$\frac{A^2}{\rho} \int_0^D \sin^2(k_{zm}z')dz' = 1 \tag{5.42}$$

Given $\sin^2(\alpha) = \frac{1-\cos(2\alpha)}{2}$, we obtain that:

$$\frac{A^2}{\rho} \int_0^D \frac{1-\cos(2k_{zm}z')}{2} dz' = 1 \tag{5.43}$$

$$\frac{A^2}{\rho} \frac{D - \cos(2k_{zm}D)/2k_{zm}}{2} = 1 \tag{5.44}$$

in which due to $2k_{zm}D = (2m-1)\pi$. This leads to $\cos(2k_{zm}D) = 0$, thus, $A = \sqrt{\frac{2\rho}{D}}$. The corresponding eigenfunctions are given by

$$\Psi_m(z) = \sqrt{\frac{2\rho}{D}} \sin(k_{zm}(z-z_1)) \tag{5.45}$$

The function satisfy both boundary conditions.

5.3.2 The radial equation

We can represent an arbitrary function as a sum of the normal modes, thus, we have the Green's function as:

$$G_\omega(\vec{r}, \vec{r}_0) = \sum_{m=1}^{\infty} \Phi_m(R)\Psi_m(Z) \tag{5.46}$$

where $R = r - r_0$, and $Z = z - z_0$. The source is at $z_0 = z_s, r_0 = 0$, therefore, $R = r, Z = z - z_s$. From the starting point, the inhomogeneous Helmholtz Equation in cylindrical coordinate:

$$\frac{1}{r}\frac{\partial}{\partial r}(r\frac{\partial G_\omega(\vec{r}, \vec{r}_0)}{\partial r}) + \frac{\partial^2 G_\omega(\vec{r}, \vec{r}_0)}{\partial z^2} + \frac{\omega^2}{c^2} G_\omega(\vec{r}, \vec{r}_0) = -\frac{\delta(r)\delta(z-z_s)}{2\pi r} \tag{5.47}$$

After applying the separation of variables and substituting the function of z by k_{rm}^2, we obtain that:

$$\sum_{m=1}^{\infty} (\Psi_m(Z)\frac{1}{r}\frac{d}{dr}(r\frac{d\Phi_m(R)}{dr}) + k_{rm}^2 \Phi_m(R)\Psi_m(Z)) = -\frac{\delta(r)\delta(z-z_s)}{2\pi R} \tag{5.48}$$

Applying the operator:

$$\int_0^D (\cdot)\frac{\Psi_n(Z)}{\rho} dz \tag{5.49}$$

Due to the orthogonality of the Sturm-Liouville problems and normalized Eq. (5.31), only nth term in the sum remains, yielding:

$$\frac{1}{r}\frac{d}{dr}(r\frac{d\Phi_n(r)}{dr}) + k_{rn}^2\Phi_n(r) = \frac{\delta(r)\Psi_n(z_s)}{2\pi r\rho} \tag{5.50}$$

Now we have the above function as the Bessel function, the solution is given in terms of a Hankel function as:

$$\Phi_n(r) = \frac{i}{4\rho}\Psi_n(z_s)H_0^{(2)}(k_{rn}r) \tag{5.51}$$

with the time dependence of the form $exp(i\omega t)$, we take the Hankel function of the second kind for the outgoing waves, which is determined by the radiating condition as $r \to \infty$.

Using asymptotic approximation to the Hankel function,

$$H_0^{(1)}(kr) = \sqrt{\frac{2}{kr\pi}}e^{i(kr-\pi/4)} \tag{5.52}$$

$$H_0^{(2)}(kr) = \sqrt{\frac{2}{kr\pi}}e^{-i(kr-\pi/4)} \tag{5.53}$$

Now, we obtain the Green's function at $\vec{r_0} = \vec{r_s} = (0, z_s)$ as:

$$G_\omega(\vec{r}, \vec{r_s}) = \sum_{m=1}^{\infty} \frac{i}{2D}\sin(k_{zm}(z_s))\sin(k_{zm}(z))H_0^{(2)}(k_{rm}(r-0)) \tag{5.54}$$

$$G_\omega(\vec{r}, \vec{r_0}) = \sum_{m=1}^{\infty} \frac{i}{2D}\sin(k_{zm}(z_0))\sin(k_{zm}(z))H_0^{(2)}(k_{rm}(r-r_0)) \tag{5.55}$$

where $k_{zm} = \frac{2m-1}{2D}\pi$ and $k_{rm} = \sqrt{k^2 - k_{zm}^2}$.

5.4 Point source and line source in the free field

As a case of the use of Green's theorem to boundary value problem, we first apply it to the simple case of a point source in the field without the resonator system. The point source is uniform and equally strong in all directions. It is located on the axis of symmetry. Thus, the pressure Helmholtz equation in two dimension for the domain can be read as:

$$\nabla^2\tilde{p}(r,z,\omega) + k^2\tilde{p}(r,z,\omega) = \tilde{f}(r,z,\omega) \tag{5.56}$$

Now, we introduce the Green's function, which is a sum of a particular solution such as $g_\omega(\vec{r}, \vec{r_0})$ and a homogeneous solution $H_\omega(\vec{r})$, with the superposition of the two solutions satisfying the two boundary conditions as well as the radiation condition. Therefore, we have the general Green's function reads:

$$G_\omega(\vec{r}, \vec{r_0}) = g_\omega(\vec{r}, \vec{r_0}) + H_\omega(\vec{r}) \tag{5.57}$$

where $g_\omega(\vec{r}, \vec{r_0})$ is a particular solution satisfying the same in-homogeneous Helmholtz equation as, $G_\omega(\vec{r}, \vec{r_0})$,

$$[\nabla^2 + k^2]g_\omega(\vec{r}, \vec{r_0}) = -\delta(\vec{r} - \vec{r_0}) \tag{5.58}$$

$$[\nabla^2 + k^2]G_\omega(\vec{r}, \vec{r_0}) = -\delta(\vec{r} - \vec{r_0}) \tag{5.59}$$

and $H_\omega(\vec{r})$ is any function satisfying the homogeneous Helmholtz equation,

$$[\nabla^2 + k^2]g_\omega(\vec{r}, \vec{r}_0) = -\delta(\vec{r} - \vec{r}_0) \tag{5.60}$$

For a simple point source, the source term is expressed as:

$$\tilde{f}(\vec{r}) = S_\omega \delta(\vec{r} - \vec{r}_s) \tag{5.61}$$

in which $\vec{r}_s = (0, z_s)$ being the vector of the source location, S_ω is the source strength. Here we normalize the source to yield a unit pressure at $r = 1$ by using $S_\omega = -4\pi$, and we could modify the pressure amplitude by multiplying a constant on the source strength later on. Then we have:

$$\frac{1}{r}\frac{\partial}{\partial r}(r\frac{\partial g_\omega}{\partial r}) + \frac{\partial^2 g_\omega}{\partial z^2} + \frac{\omega^2}{c^2}g_\omega = -\frac{\delta(r-0)\delta(z-z_s)}{2\pi r} \tag{5.62}$$

After we solve the Green's function, the field can be determined as,

$$\tilde{p}(r, \omega) = -\int_V S_\omega G_\omega(\vec{r}, \vec{r}_0)dV_0 \tag{5.63}$$

This can be easily verified as:

$$[\nabla^2 + k^2]\tilde{p}(r, \omega) = -\int_V S_\omega[\nabla^2 + k^2]G_\omega(\vec{r}, \vec{r}_0)dV_0 \tag{5.64}$$

$$= \int_V S_\omega \delta(\vec{r} - \vec{r}_0)dV_0 = \tilde{f}(\vec{r}_0) \tag{5.65}$$

After we solve the Green's function, the field can be determined as,

$$\tilde{p}(r, \omega) = -\int_V \tilde{f}(\vec{r}_0)G_\omega(\vec{r}, \vec{r}_0)dV_0 \tag{5.66}$$

Similarly, the pressure filed for a line source is given as:

$$\tilde{p}((\vec{r}, \omega) = -\int_V \tilde{f}(\vec{r}_0)G_\omega(\vec{r}, \vec{r}_0)dV_0 \tag{5.67}$$

$$= -\int_{z_2}^{z_1} S_\omega G_\omega(\vec{r}, \vec{r}_s)dz_0 \tag{5.68}$$

5.5 Results and discussion

5.5.1 Point source and line source field

In the previous section, by using the Normal Mode (NM) method we have obtained the Green's function, which could satisfy the homogeneous Helmholtz equation given the boundary and radiation conditions. Because the field containing a point source or a homogeneous line source has a simple boundary geometry and homogeneous boundary conditions, the pressure field can be easily described by using Green's function in this study.

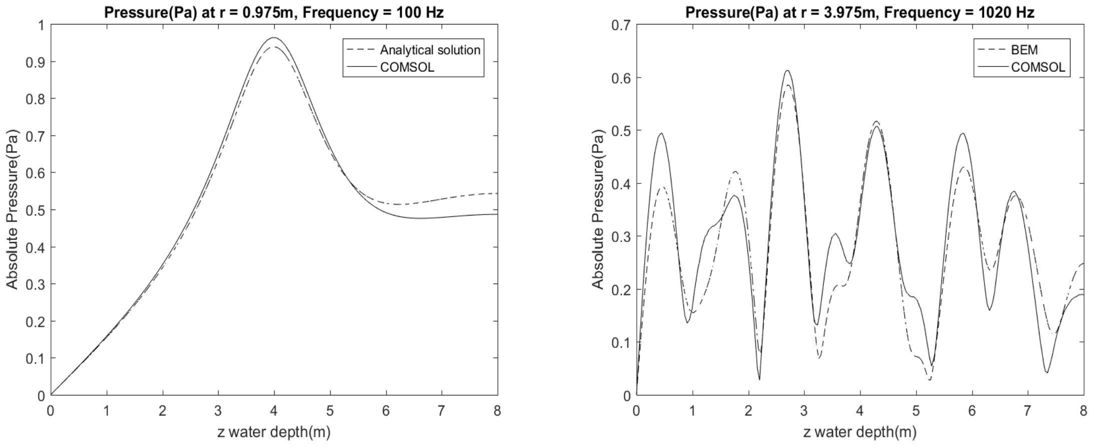

(a) **(b)**

Figure 5.2: Absolute pressure in the point source field

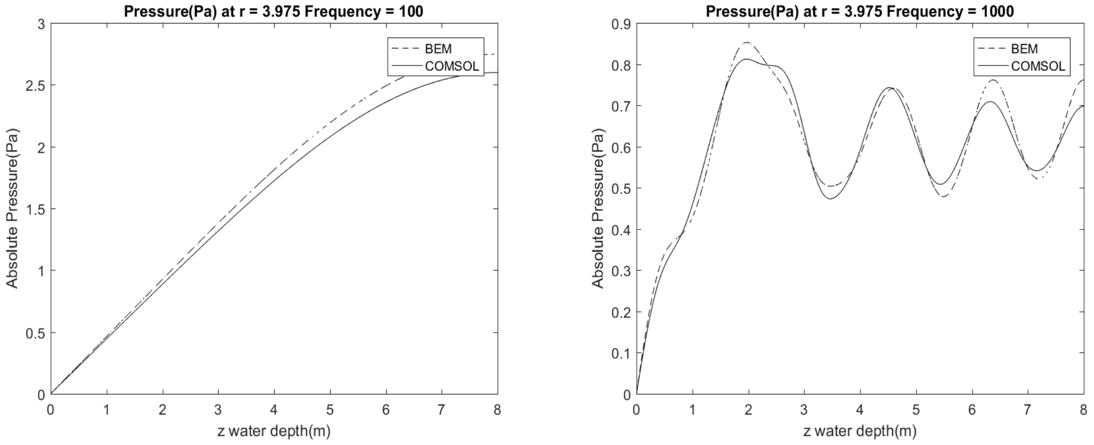

(a) **(b)**

Figure 5.3: Absolute pressure in the line source field

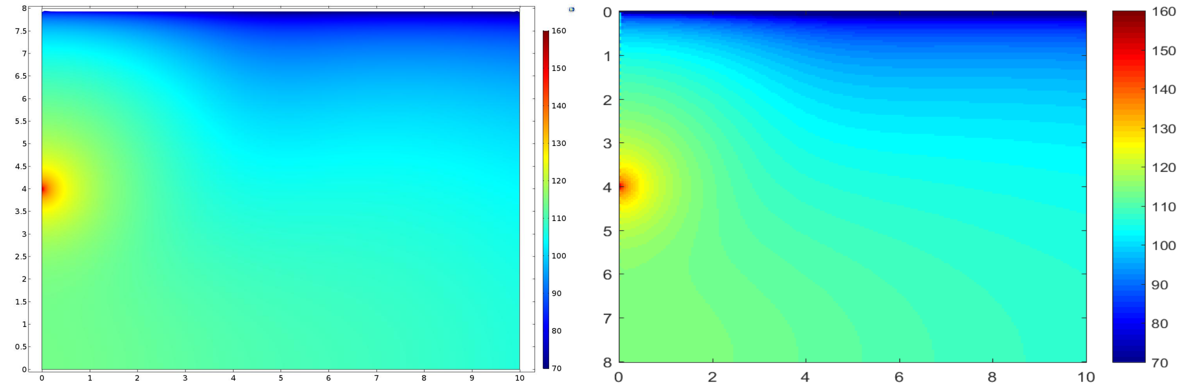

(a) COMSOL Model at 100 Hz **(b)** Analytical model at 100 Hz

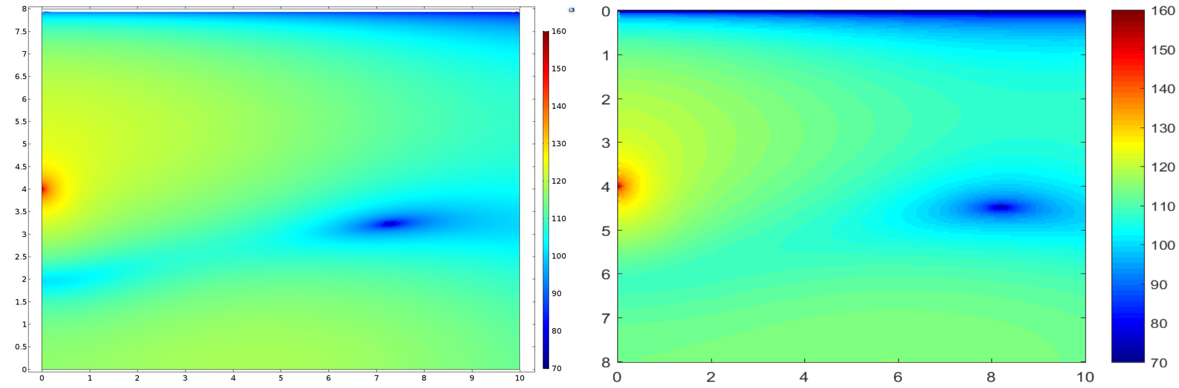

(c) COMSOL Model at 150 Hz **(d)** Analytical model at 150 Hz

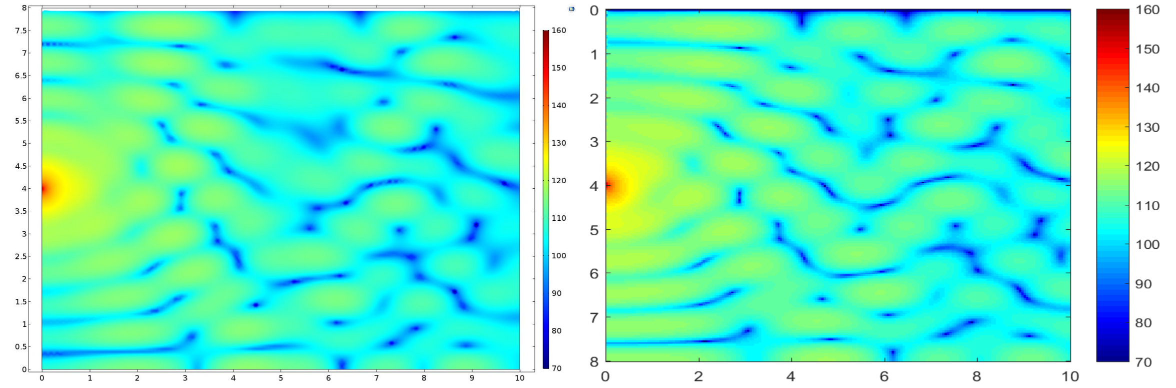

(e) COMSOL Model at 1000 Hz **(f)** Analytical model at 1000 Hz

Figure 5.4: Sound pressure level (dB re 1μ Pa) in the point source field

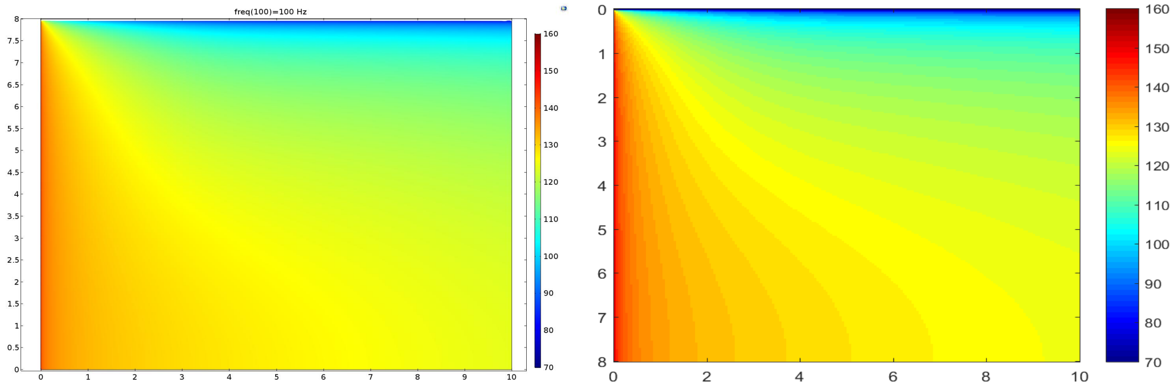

(a) COMSOL Model at 100 Hz **(b)** Analytical model at 100 Hz

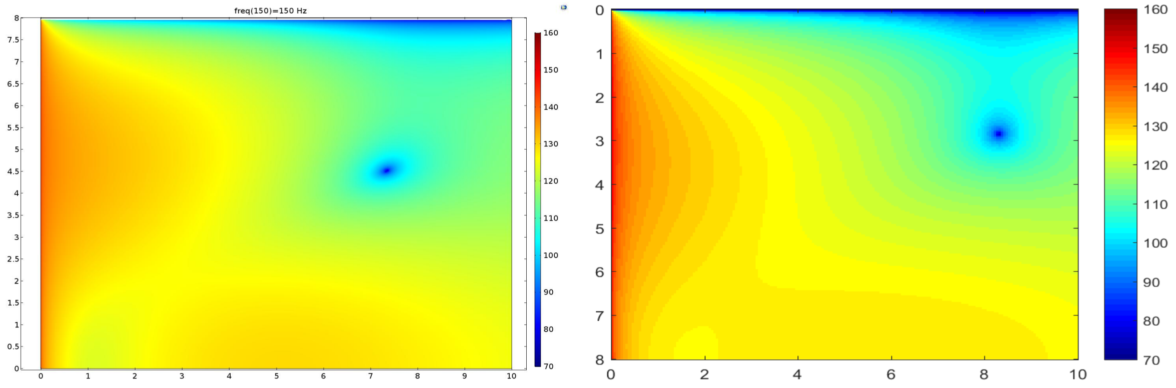

(c) COMSOL Model at 150 Hz **(d)** Analytical model at 150 Hz

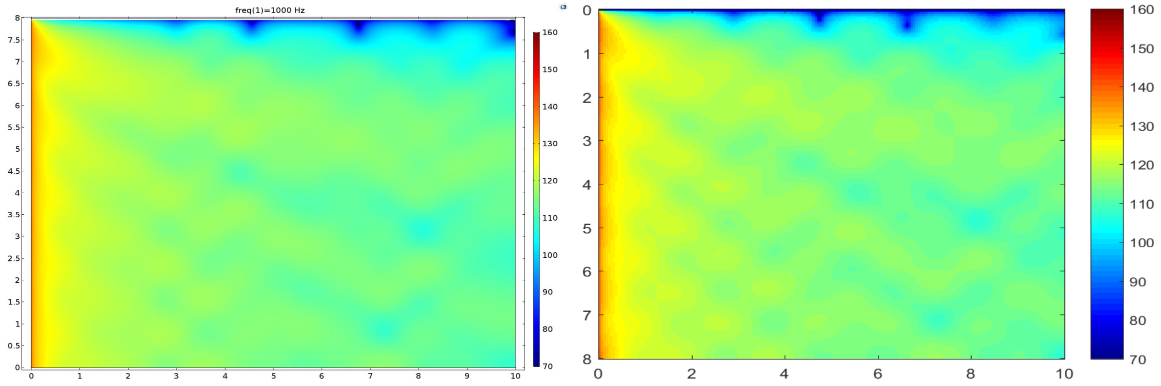

(e) COMSOL Model at 1000 Hz **(f)** Analytical model at 1000 Hz

Figure 5.5: Sound pressure level (dB re 1μ Pa) in line source field

Both the results from the analytical model and finite element model are obtained. The sound pressure level for two models are compared at different locations and different frequencies.

In this study, we built an analytical model with a dimension $(r, z) = (10m, 8m)$, the derivation of the governing equations has been discussed. A point source is located at the middle of the domain at 4-meter water depth. The results from the two models for the sound pressure level at the two points at the frequency as 100 Hz and 1020 Hz are compared. The margin of error indicates the reliability of the analytical model. Hence, the implementation of the analytical model in matlab for the point source could be validated through the finite element model. The same conclusion can be drawn from the plots of the sound pressure level distribution at the cross section of the 3-D cylindrically symmetric field. As shown in these three figures at different frequencies, the patterns of the pressure distribution have a excellent agreement between finite element model in COMSOL Multiphysics and analytical model.

The same validation cases are carried out for line source field. The line source is located along the z-axis coordinate from sea surface to the sea bottom. As shown in the Figure 5.3 and Figure 5.5, the results show that the analytical model could well describe the line source filed.

5.5.2 The dispersion relation

The dispersion relation relates the angular frequency ω to the horizontal wavenumber k_{rm} for this specific case as:

$$k_{rm} = \sqrt{(\frac{\omega}{c})^2 - [(m - \frac{1}{2})\frac{\pi}{D}]^2}, \quad m = 1, 2, ... \tag{5.69}$$

Thus, there are two groups of modes need to be considered. The propagating modes represent the real horizontal wavenumber, which are propagating horizontally away from the source. The evanescent modes represent the imaginary wavenumber, which are exponentially decaying in range.

$$\begin{aligned} &Propagating \quad modes: for \quad m < \frac{kD}{\pi} + \frac{1}{2}, \quad k_{rm} \quad is \quad real \\ &Evanescent \quad modes: for \quad m > \frac{kD}{\pi} + \frac{1}{2}, \quad k_{rm} \quad is \quad imaginary \end{aligned}$$

Thus, given the dispersion relation, we find the roots for the waveguide as the following Figure 5.6. It is evident that with the larger frequency, the propagating modes increase.

In addition, the wavenumbers relate to frquency in a nonlinear way with the strong frequency-dependent propagation. The relations are shown in the Figure 5.7 as frequency versus k_{rm}.

5.5.3 The number of modes

Given the form of the analytical solutions, we know that each normal mode can be viewed as a traveling wave in the horizontal direction and a standing wave along the depth. Therefore, the more modes one use in the model, the more accurate and convergent the results will be. However, the high dimensions of the system would require large computational effort. Thus,

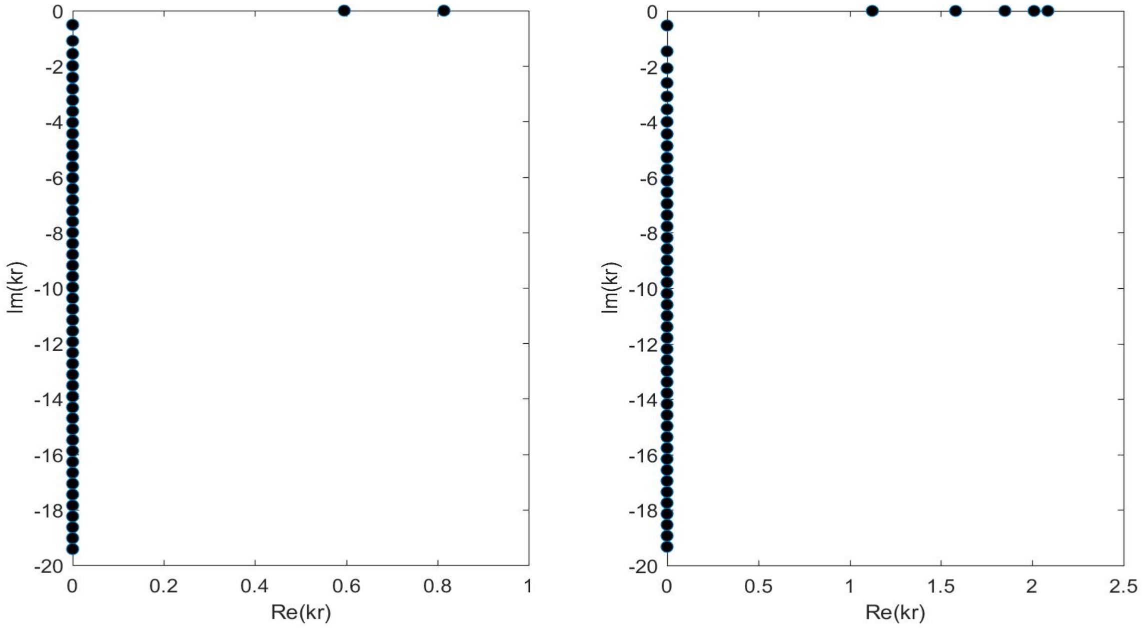

(a) **(b)**

Figure 5.6: Roots of the dispersion relation for the waveguide: (a) f = 200 Hz, (b) f = 500 Hz

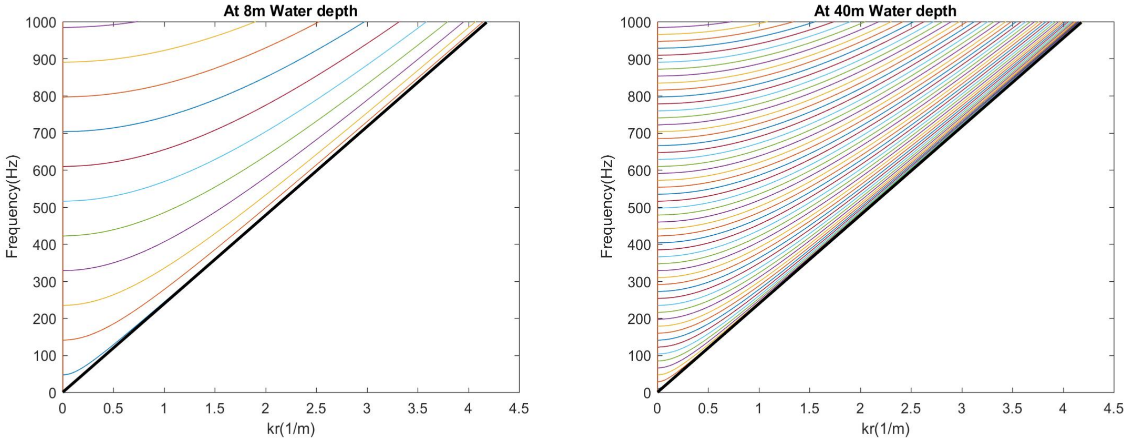

(a) **(b)**

Figure 5.7: $f - k_{rm}$ diagram for the waveguide corresponding to the propagating modes: (a) 8 m water depth, (b) 40 m water depth

in order to save the computational time, we need to determine the minimum number of modes that could achieve the sufficient accuracy for the results.

Based on the several case studies shown in Figure 5.8, we found that the convergence of the results will depend on the frequency, water depth and the number of modes we use. In this study, we focus on the low-frequency sound waves(below 500 Hz) and shallow water

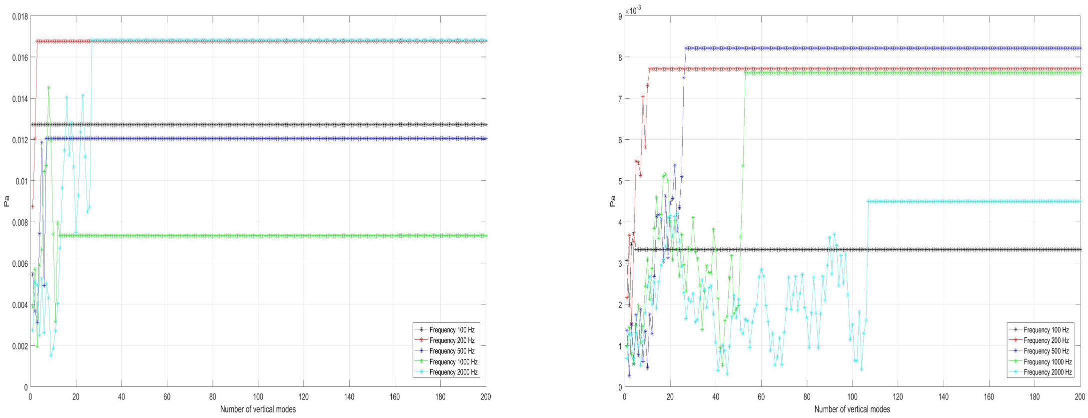

(a) **(b)**

Figure 5.8: Absolute pressure corresponding to the number of the vertical modes: (a) Point (r,z)=(1 km,5 m) in 10 m water-depth waveguide, (b) Point (r,z)=(1 km,20 m) in 40 m water-depth waveguide

environment. Therefore, we decide to use **50** modes in the computation of the pressure field in the present model. The mesh size itself won't influence the convergence of the results but will affect the grid resolution of the pressure distribution figures.

Chapter 6

3-D noise reduction prediction model

Now we can develop the 3-D acoustically coupled model containing both the resonator system and noise source. The noise source can be substituted by the point source or line source as mentioned in Chapter 5. The behaviour of the resonator will be described by the frequency response function given by the finite element model of the open-ended resonator in this case.

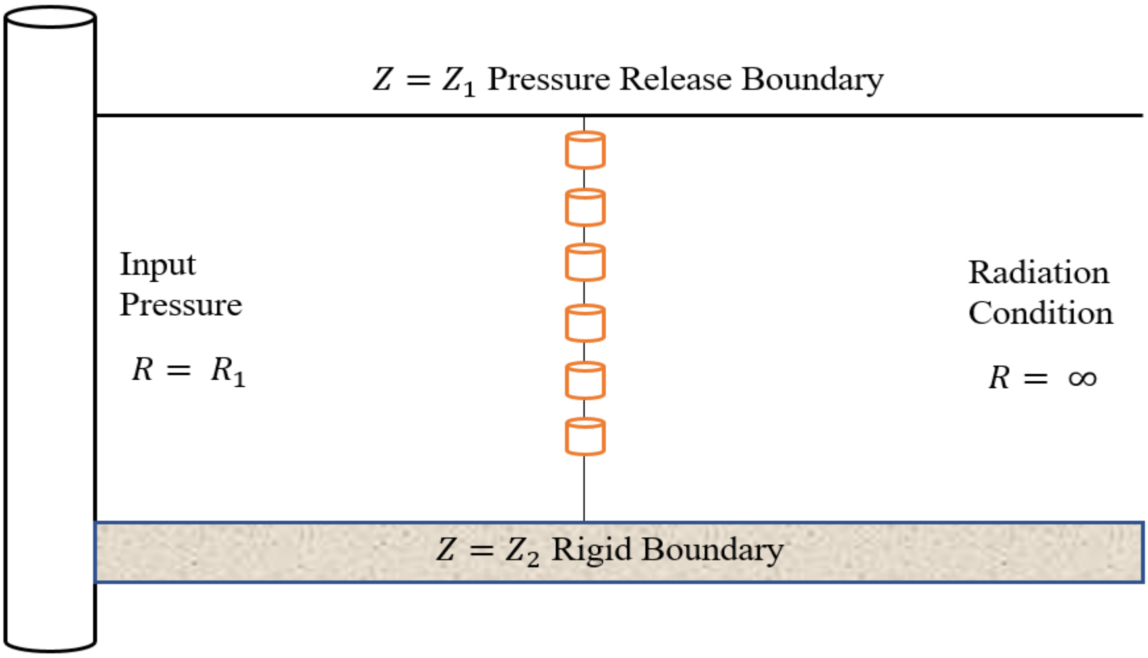

Figure 6.1: The resonator-based noise mitigation system

The boundary element method is used for simulation purposes. The pressure field can be obtained through the boundary integral equation, which consists of the contribution to the pressure field from the opening-end of the resonator and the contribution from the noise source or point source in this case. The waveguide for this model is schematically depicted in the Figure 6.1.

Based on these governing equation, the Green's function is constructed in 3-D. Then, the boundary integral equation can be decomposed into the sum of all the resonators in the domain. Since the resonator and the sound source are coupled, and the individual resonator also coupled with other resonators, a matrix equation is formed to find the pressure at the site of the resonator first. By substituting the pressure and the normal derivative of the pressure back into the boundary integral equation, we finally could obtain the pressure field anywhere in the acoustic domain.

6.1 Green's function for 3-D cylindrical coordinate

In 3D cylindrical coordinate, the Laplacian operator ∇^2 is defined as:

$$\nabla^2 = \frac{\partial^2}{\partial r^2} + \frac{1}{r}\frac{\partial}{\partial r} + \frac{1}{r^2}\frac{\partial}{\partial \phi^2} + \frac{\partial^2}{\partial z^2} \tag{6.1}$$

The homogeneous Helmholtz equation in terms of homogeneous solution $H_\omega(\vec{r})$ of the Green's function is given as:

$$\frac{1}{r}\frac{\partial}{\partial r}\left(r\frac{\partial H_\omega(\vec{r})}{\partial r}\right)+\frac{1}{r^2}\frac{\partial^2 H_\omega(\vec{r})}{\partial \phi^2} + \frac{\partial^2 H_\omega(\vec{r})}{\partial z^2} + k^2 H_\omega(\vec{r}) = 0 \tag{6.2}$$

where $\vec{r}$ represent (r, ϕ, z). We could solve this equation by using the method of **separation of variables**:

$$H_\omega(\vec{r}) = R(r)\Phi(\phi)Z(z) \tag{6.3}$$

Substituting and dividing the above equation, we could find:

$$\frac{1}{rR}\frac{\partial}{\partial r}\left(r\frac{\partial R}{\partial r}\right)+\frac{1}{r^2\Phi}\frac{\partial^2 \Phi}{\partial \phi^2} + \frac{1}{Z}\frac{\partial^2 Z}{\partial z^2} + k^2 = 0 \tag{6.4}$$

The third term is independent of r and ϕ, thus we could denote this term equal to a separation constant as k_{rm}^2,

$$\frac{d^2 Z(z)}{dlz^2} + (k^2 - k_{rm}^2)Z(z) = 0 \tag{6.5}$$

$$\frac{d^2 Z(z)}{dz^2} + k_{zm}^2 Z(z) = 0 \tag{6.6}$$

where the vertical wavenumber $k_{zm} = \sqrt{k^2 - k_{rm}^2} = \sqrt{(\omega^2/c^2) - k_{rm}^2}$. Thus, we obtain the same modal equation when we solve the two dimensional coordinate wave equation as:

$$k_{zm} = \frac{(m - \frac{1}{2})\pi}{D}, \quad m = 1, 2, ... \tag{6.7}$$

where D is water depth. The solution for the modal equation is given in the same form when we solve the two dimensional wave equation as:

$$Z_m(z) = \sqrt{\frac{2\rho}{D}} \sin(k_{zm}(z - z_1)), z_1 = 0 \tag{6.8}$$

The function satisfy both boundary conditions. This leaves:

$$\frac{1}{rR}\frac{d}{dlr}\left(r\frac{dR}{dlr}\right)+\frac{1}{r^2\Phi}\frac{d^2\Phi}{d\phi^2} + k^2 - k_z^2 = 0 \tag{6.9}$$

Now, we could define the radial wave number as:

$$k_r^2 = k^2 - k_z^2 \tag{6.10}$$

Multiplying the resulting equation by r^2 to find:

$$\frac{r}{R}\frac{d}{dr}\left(r\frac{dR}{dr}\right)+\frac{1}{\Phi}\frac{d^2\Phi}{d\phi^2} + k_r^2 r^2 = 0 \tag{6.11}$$

In the above equation, we find the second term is independent of r and z, so we could denote it as:

$$\frac{1}{\Phi}\frac{d^2\Phi}{d\phi^2} = -n^2 \tag{6.12}$$

Since there is no limit in ϕ direction, the periodic boundary condition and initial condition is imposed as:

$$\Phi(\phi) = \Phi(\phi + 2\pi) \tag{6.13}$$

$$\Phi(0) = 1 \tag{6.14}$$

The solution for $\Phi(\phi)$ can be given as the circumferential eigenfunction,

$$\Phi(\phi) = e_n cos(n\phi) \tag{6.15}$$

where e_n is defined as follows:

$$e_n = \begin{cases} \frac{1}{\sqrt{2\pi}}, & n = 0 \\ \frac{1}{\sqrt{\pi}}, & n \neq 0 \end{cases} \tag{6.16}$$

By applying the method of separation of variables, now we have an ordinary differential equation in r direction only,

$$\frac{r}{R}\frac{d}{dr}\left(r\frac{dR}{dr}\right)+[(k_r r)^2 - n^2]R = 0 \tag{6.17}$$

The remaining equation is a Bessel's Equation of order n. We could rewrite the equation as:

$$\xi\frac{\partial}{\partial\xi}\left(\xi\frac{\partial R}{\partial\xi}\right)+(\xi^2 - n^2)R = 0 \tag{6.18}$$

The solution is given in terms of the Hankel function of order n and of the second kind to represent the outgoing traveling wave (when we factor out the time dependence through Fourier transform by $e^{i\omega t}$):

$$H_n^{(2)}(k_r r) = J_n(k_r r) - iY_n(k_r r) \tag{6.19}$$

where J_n and Y_n are the Bessel's function of the first kind and the second kind respectively. Theoretically, the solutions to the Bessel equation can be expressed as any linear combination of J_n, Y_n, $H_n^{(1)}$ and $H_n^{(2)}$ [19]. However, it is worth to mention that only the linear independent pair of functions need to be chosen in order to avoid the numerical instability of the solution. For the case of short ranges and high circumferential order, the normalization of the Hankel and Bessel functions need to be applied to avoid the loss of distinctions between two functions we choose [20].

Now, the in-homogeneous three dimensional Helmholtz equation for a point source can be represented as:

$$\begin{aligned}\frac{1}{r}\frac{\partial}{\partial r}\left(r\frac{\partial G_\omega(\vec{r},\vec{r}_0)}{\partial r}\right)+\frac{1}{r^2}\frac{\partial^2 G_\omega(\vec{r},\vec{r}_0)}{\partial \phi^2}+\frac{\partial^2 G_\omega(\vec{r},\vec{r}_0)}{\partial z^2}+k^2G_\omega(\vec{r},\vec{r}_0)\\ =-\frac{\delta(r-r_0)\delta(z-z_0)\delta(\phi-\phi_0)}{r}\end{aligned} \tag{6.20}$$

Using the normal mode method,the solution is given in the form of radial and depth eigenfunction:

$$G_\omega(\vec{r},\vec{r}_0)=\sum_{n=0}^{\infty}\sum_{m=1}^{\infty}R_{mn}(r,r_0)\Phi_n(\phi,\phi_0)Z_m(z,z_0) \tag{6.21}$$

By substituting Eq. (6.21) to Eq. (6.20), and applying the modal equation,

$$\frac{d^2Z}{dz^2}+k_{zm}^2Z=0,\quad m=1,2,... \tag{6.22}$$

and the equation in terms of the azimuth,

$$\frac{d^2\Phi}{d\phi^2}+n^2\Phi=0,\quad n=0,1,2,... \tag{6.23}$$

This yields the modal form of the Helmholtz equation,

$$\begin{aligned}\sum_{n=0}^{\infty}\sum_{m=1}^{\infty}\left[\frac{1}{r}\frac{d}{dr}\left(r\frac{dR_{mn}(r,r_0)}{dr}\right)+\left(k_{rn}^2-\frac{n^2}{r^2}\right)R_{mn}(r,r_0)\right]\Phi_n(\phi,\phi_0)Z_m(z,z_0)\\ =-\frac{\delta(r-r_0)\delta(z-z_0)\delta(\phi-\phi_0)}{r}\end{aligned} \tag{6.24}$$

Next, by applying the operator

$$\int_0^D(\cdot)\frac{Z_\nu(z)}{\rho}dz \tag{6.25}$$

and the operator

$$\int_{-\pi}^{\pi}(\cdot)\Phi_\mu(\phi)d\phi \tag{6.26}$$

to Eq. (6.20), because the orthogonality property for the modes and the assumption of the normalized modes, we obtain the radial equation as follows:

$$\begin{aligned}\frac{1}{r}\frac{d}{dr}\left(r\frac{dR_{mn}(r-r_0)}{dr}\right)+\left(k_{rn}^2-\frac{n^2}{r^2}\right)R_{mn}(r,r_0)\\ =-\frac{\delta(r-r_0)\Phi_n(\phi_0)Z_m(z_0)}{r\rho}\end{aligned} \tag{6.27}$$

Now, we need to solve the above equation for $R_{mn}(r, r_0)$, which is the Bessel's Equation of order n as we discussed above. The solution is expressed in the form of Hankel function as:

$$R_{mn}(r, r_0) = A_{mn} \frac{\Phi_n(\phi_0) Z_m(z_0)}{\rho} H_n^2(k_{rm}(r - r_0)) \tag{6.28}$$

This solution is numerically unstable for $n > k_{rm} r$, because the Hankel functions approach infinity very quickly for high circumferential orders.

For a point source, the pressure is 3-D cylindrically symmetric solution. which is only related to the depth modes. Because the incident field produced by the point source needs not be summed up with respect to the azimuthal index n, the solution is simplified by,

$$R_m(r, r_0) = A_m \frac{Z_m(z_0)}{\rho} H_0^2(w_m) \tag{6.29}$$

where

$$w_m = k_{rm} r' \tag{6.30}$$

and r' is the range of a point in the field with respect to the source,

$$r' = \sqrt{r_0^2 + r^2 - 2 r_0 r \cos(\phi_0 - \phi)} \tag{6.31}$$

Hence, a solution to the inhomogeneous Helmholtz equation can be expressed in the following form:

$$G_\omega(\vec{r}, \vec{r}_0) = \sum_{m=1}^{\infty} \left[\frac{i}{2D} \sin(k_{zm} z_0) \sin(k_{zm} z) H_0^{(2)}(k_{rm} r') \right] \tag{6.32}$$

6.2 Point source and line source field

In the previous section, we already obtained the Green's function satisfying the in-homogeneous 3D Helmholtz equation. Hence the pressure field for a point source can be expressed as:

$$\tilde{p}(r, \omega) = -\int_V \tilde{f}(\vec{r}_0) G_\omega(\vec{r}, \vec{r}_0) dV_0 \tag{6.33}$$

$$= -S_\omega G_\omega(\vec{r}, \vec{r}_s) \tag{6.34}$$

Similarly, the pressure filed for a line source is given by:

$$\tilde{p}((\vec{r}, \omega) = -\int_V \tilde{f}(\vec{r}_0) G_\omega(\vec{r}, \vec{r}_0) dV_0 \tag{6.35}$$

$$= -\int_{z_2}^{z_1} S_\omega G_\omega(\vec{r}, \vec{r}_s) dz_0 \tag{6.36}$$

6.3 3-D acoustic coupling model for a resonator-based noise mitigation system

The new designed resonator-based system can be seen as multi-array of Helmholtz resonators. Although the coupling between a Helmholtz resonator and the underwater environment is lacking enough investigations. The various transmission mediums do not change the absorption mechanism of the resonators. Thus, the present model is based on the acoustically coupled interaction between the underwater Helmholtz resonators and the noise source.

Analytical solutions of the underwater pressure field and source strength out of the resonator are derived without other hypotheses but just using mathematical manipulation. As we already mentioned in the previous chapter, we could use the single-degree-of-freedom mass-spring-dashpot system to describe the behaviour of resonators provided that the geometric dimensions of the resonator are very small compared to the targeted sound wavelength. For different tuned and shaped resonators, we only need to adjust the parameters to fit the noise control performance.

As for the description of the waveguide, the noise source and the resonator have been obtained in the previous sections. Now we could formulate the pressure field for the whole field with arrays of resonators. The Boundary Element Method will be exploited, the formulation of the matrix equation will be discussed in the section below.

6.3.1 Governing equation

Using the Boundary Element Method, the pressure field can be expressed by a superposition of noise source and resonators through integrals. Boundary Element Method uses a discretisation of Green's theorem showing the field in a volume regarding an integral of the field and its derivative on the boundary. Thus, a real boundary separating an interior region from an exterior region is defined in such a way that the boundary integral can be used. Only the boundary of the exterior domain needs to be discretised since the boundary integral formulation inherently satisfies the wave equation throughout the volume as well as the radiation conditions at infinity.

In this case, we could find a Green's function $G_\omega(\vec{r},\vec{r}_0)$ that satisfies the perfectly free surface condition, perfectly rigid boundary condition and radiation condition. The pressure field can be expressed by Green's theorem as:

$$\begin{aligned}\tilde{p}(\vec{r},\omega) = &\int_S \left[G_\omega(\vec{r},\vec{r}_0)\frac{\partial \tilde{p}(\vec{r}_0)}{\vec{n}_0} - \tilde{p}(\vec{r}_0)\frac{\partial G_\omega(\vec{r},\vec{r}_0)}{\vec{n}_0}\right] dS_0 \\ &- \int_V \tilde{f}(\vec{r}_{s0}) G_\omega(\vec{r},\vec{r}_{s0}) dV_{s0}\end{aligned} \tag{6.37}$$

In 3D cases, the normal derivative of the pressure and the Green's function is not necessarily to the positive z direction, but will depend on the position we deploy the resonator. In order to be compatible with different design purposes, we assume the normal vector to the opening end as $\vec{n}_0 = (\hat{e}_r, \hat{e}_z, \hat{e}_\phi)$. Next, the derivative of the Green's function can be formulated:

$$\frac{\partial G_\omega(\vec{r},\vec{r}_0)}{\partial z} = \sum_{m=1}^{\infty} \left[A_m \frac{\partial Z_m(z)}{\partial z} Z_m(z_0) H_0^{(2)}(k_{rm} r') \right] \tag{6.38}$$

$$\begin{aligned}\frac{\partial G_\omega(\vec{r},\vec{r}_0)}{\partial r} &= \sum_{m=1}^{\infty} \left[A_m Z_m(z) Z_m(z_0) \frac{\partial H_0^{(2)}(w_n)}{\partial w_n} \frac{\partial w_n}{\partial r} \right] \\ &= \sum_{m=1}^{\infty} \left[-A_m Z_m(z) Z_m(z_0) \frac{\partial w_n}{\partial r} H_1^{(2)}(w_n) \right]\end{aligned} \tag{6.39}$$

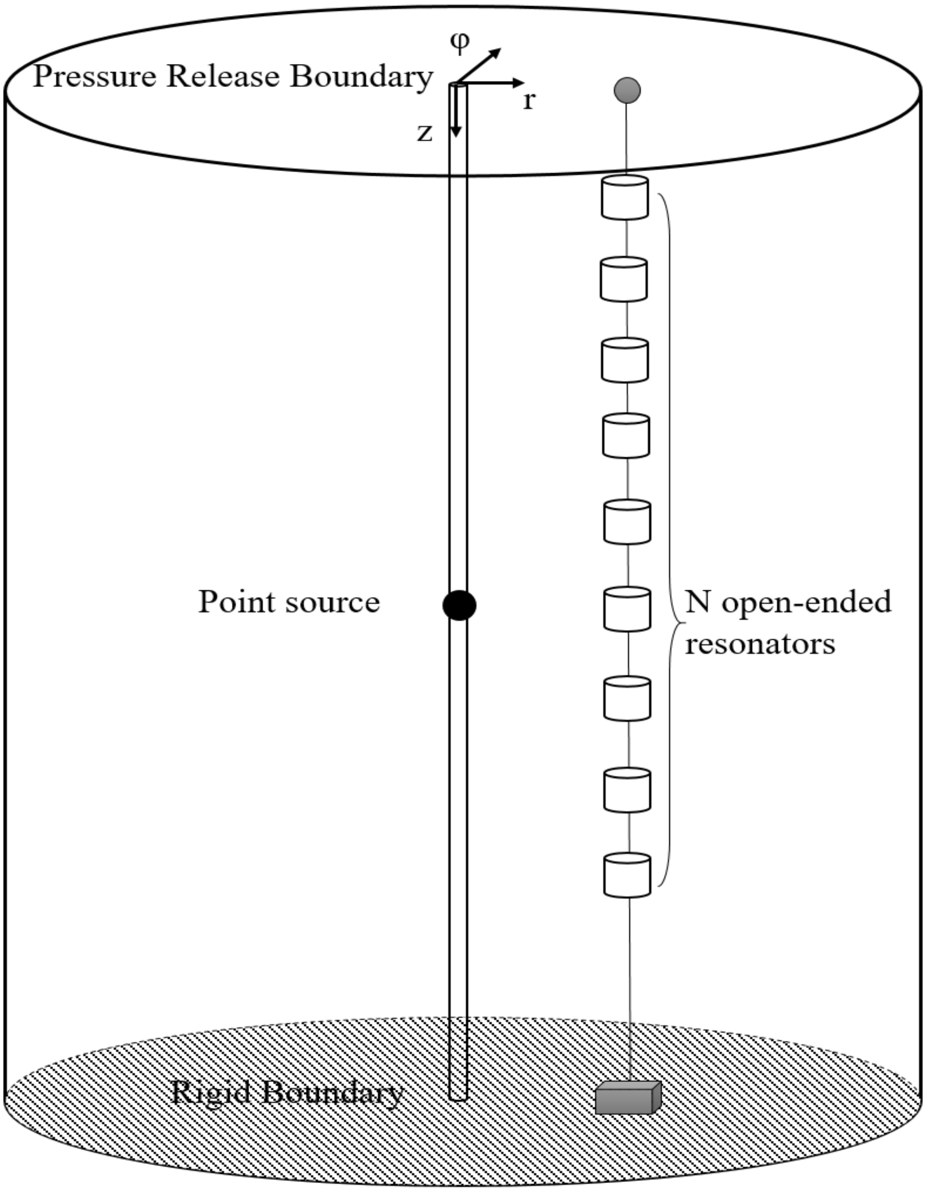

Figure 6.2: The waveguide containing an array of resonators

$$\begin{aligned}\frac{\partial G_\omega(\vec{r},\vec{r}_0)}{\partial \phi} &= \sum_{m=1}^{\infty}\left[A_m Z_m(z) Z_m(z_0)\frac{\partial H_0^{(2)}(w_n)}{\partial w_n}\frac{\partial w_n}{\partial \phi}\right] \\ &= \sum_{m=1}^{\infty}\left[-A_m Z_m(z) Z_m(z_0)\frac{\partial w_n}{\partial \phi} H_1^{(2)}(w_n)\right]\end{aligned} \tag{6.40}$$

where

$$\frac{\partial Z_m(z)}{\partial z} = k_{zm}\cos(k_{zm}(z-z_1)) \tag{6.41}$$

$$\frac{\partial H_0^{(2)}(w_n)}{\partial w_n} = -H_1^{(2)}(w_n) \tag{6.42}$$

$$\frac{\partial w_n}{\partial r} = \frac{1}{2}k_{rm}\cdot r'^{-1}(2r - 2r_s\cos(\phi_0-\phi)) \tag{6.43}$$

$$\frac{\partial w_n}{\partial \phi} = \frac{1}{2}k_{rm}\cdot r'^{-1}(-2rr_s\sin(\phi_0-\phi)) \tag{6.44}$$

Hence, the normal derivative of the Green's function can be expressed as:

$$\frac{\partial G_\omega(\vec{r},\vec{r}_0)}{\partial n} = \frac{\partial G_\omega(\vec{r},\vec{r}_0)}{\partial r}\hat{e}_r + \frac{\partial G_\omega(\vec{r},\vec{r}_0)}{\partial z}\hat{e}_z + \frac{\partial G_\omega(\vec{r},\vec{r}_0)}{\partial \phi}\hat{e}_\phi \tag{6.45}$$

For the sake of simplicity, we assume that the pressure on the surface of the opening end is equally distributed, thus we could take the first integral as the surface area multiply the pressure contribution at the center point. After substituting Eq. (6.38) to Eq. (6.45).

Next, we are able to search for the pressure at the center point of the open-end of the resonator. By substituting the location of the field point and the source point as $\vec{r} = \vec{r}_0 = \vec{r}^R = (r^R, z^R, \phi^R)$, the boundary integral equation becomes:

$$\begin{aligned}\tilde{p}(\vec{r}^R,\omega) \approx{}& \alpha S^R\Big[G_\omega(\vec{r}^R,\vec{r}^R)\rho\omega^2\tilde{x}^R(\omega) - \tilde{p}(\vec{r}^R)\frac{\partial G_\omega(\vec{r}^R,\vec{r}^R)}{\partial n}\Big] \\ &+ S_\omega G_\omega(\vec{r}^R,\vec{r}_S)\end{aligned} \tag{6.46}$$

Using the transfer function, we obtain:

$$\begin{aligned}\tilde{p}(\vec{r}^R,\omega) \approx{}& \alpha S^R(G_\omega(\vec{r}^R,\vec{r}^R)\rho\omega^2 H(\omega)\tilde{p}(\vec{r}^R) - \tilde{p}(\vec{r}^R)\frac{\partial G_\omega(\vec{r}^R,\vec{r}^R)}{\partial z}) \\ &+ S_\omega G_\omega(\vec{r}^R,\vec{r}_S)\end{aligned} \tag{6.47}$$

Now, we could obtain the pressure at $\vec{r}^R$,

$$\tilde{p}(\vec{r}^R,\omega) = \mathbf{q}^R[\mathcal{L}^R]^{-1} \tag{6.48}$$

Hence, back to the boundary integral equation, after substitution of the pressure at the location of the resonator, the pressure field containing a single resonator and a point source can be given by:

$$\begin{aligned}\tilde{p}(\vec{r},\omega) ={}& \sum_{n=1}^{M}\Big\{\int_{S_n^R}\Big[G_\omega(\vec{r},\vec{r}_{n0})\frac{\partial\tilde{p}(\vec{r}^R_{n0})}{\partial n_{n0}} - \tilde{p}(\vec{r}^R_{n0})\frac{\partial G_\omega(\vec{r},\vec{r}_{n0})}{\partial n_{n0}}\Big]dS_{n0}\Big\} \\ &- \int_V \tilde{f}(\vec{r}_{s0})G_\omega(\vec{r},\vec{r}_{s0})dV_{s0}\end{aligned} \tag{6.49}$$

6.3.2 An array of resonators

For applying an array of resonators, we need to consider the coupling between each resonator. First, we formulate the boundary integral equation for a number of resonators, each denoted by the index "m":

$$\begin{aligned}\tilde{p}(\vec{r}^R_m,\omega) = &\sum_{n=1}^{M}\Big\{\int_{S_n^R}\Big[G_\omega(\vec{r}^R_m,\vec{r}_{n0})\frac{\partial \tilde{p}(\vec{r}^R_{n0})}{\partial \vec{n}_0} - \tilde{p}(\vec{r}^R_{n0})\frac{\partial G_\omega(\vec{r}^R_m,\vec{r}_{n0})}{\partial \vec{n}_0}\Big] dS_0\Big\} \\ &- \int_V \tilde{f}(\vec{r}_S) G_\omega(\vec{r}^R_m,\vec{r}_S) dV_S\end{aligned} \tag{6.50}$$

where $\vec{r}^R_m$ is the location of the resonator number m, S_n^R represent the surface area of the resonator with index "n".

Then, we substitute the spatial derivative of the pressure by the equation we obtained above,

$$\begin{aligned}\tilde{p}(\vec{r}^R_m,\omega) \approx &\sum_{n=1}^{M}\alpha S_n^R\Big(G_\omega(\vec{r}^R_m,\vec{r}^R_n)\rho\omega^2 H(\omega)\tilde{p}(\vec{r}^R_n) - \tilde{p}(\vec{r}^R_n)\frac{\partial G_\omega(\vec{r}^R_m,\vec{r}^R_n)}{\partial z}\Big) \\ &+ S_\omega G_\omega(\vec{r}^R_m,\vec{r}_S)\end{aligned} \tag{6.51}$$

We could move the terms related to number m resonator to the left hand side of the equation,

$$\begin{aligned}&\Big(1 - \alpha S_m^R(G_\omega(\vec{r}^R_m,\vec{r}^R_m)\rho\omega^2 H(\omega) - \frac{\partial G_\omega(\vec{r}^R_m,\vec{r}^R_m)}{\partial z})\Big)\tilde{p}(\vec{r}^R_m,\omega) = \\ &\sum_{n=1}^{M}\alpha S_n^R\Big(G_\omega(\vec{r}^R_m,\vec{r}^R_n)\rho\omega^2 H(\omega)\tilde{p}(\vec{r}^R_n) - \tilde{p}(\vec{r}^R_n)\frac{\partial G_\omega(\vec{r}^R_m,\vec{r}^R_n)}{\partial z}\Big) \\ &+ S_\omega G_\omega(\vec{r}^R_m,\vec{r}_S)\end{aligned} \tag{6.52}$$

The above equation is valid for all the resonators in the array, thus we could formulate the similar linear algebraic equation as:

$$\mathcal{L}^R_M \cdot \tilde{p}(\vec{r}^R_M,\omega) = \mathbf{q}^R_M \tag{6.53}$$

$$\mathcal{A}^R_m = 1 \tag{6.54}$$

$$\mathcal{B}^R_{m,n} = -\alpha S_n^R G_\omega(\vec{r}^R_m,\vec{r}^R_n)\rho\omega^2 H(\omega) + \frac{\partial G_\omega(\vec{r}^R_m,\vec{r}^R_n)}{\partial z} \tag{6.55}$$

$$\mathbf{q}^R_m = S_\omega G_\omega(\vec{r}^R_m,\vec{r}_S) \tag{6.56}$$

Thus, the corresponding M algebraic equations is shown as:

$$\mathcal{L}^R \cdot \tilde{\mathbf{p}} = \mathbf{q}^R \tag{6.57}$$

$$\begin{bmatrix} \mathcal{L}^R_{1,1} & \mathcal{L}^R_{1,2} & \cdots & \mathcal{L}^R_{1,M} \\ \mathcal{L}^R_{2,1} & \mathcal{L}^R_{2,2} & \cdots & \mathcal{L}^R_{2,M} \\ \vdots & \ddots & \vdots & \vdots \\ \mathcal{L}^R_{M,1} & \mathcal{L}^R_{M,2} & \cdots & \mathcal{L}^R_{M,M} \end{bmatrix} \cdot \begin{bmatrix} \tilde{p}(\vec{r}^R_1,\omega) \\ \tilde{p}(\vec{r}^R_2,\omega) \\ \vdots \\ \tilde{p}(\vec{r}^R_M,\omega) \end{bmatrix} = \begin{bmatrix} \mathbf{q}(\vec{r}^R_1,\omega) \\ \mathbf{q}(\vec{r}^R_2,\omega) \\ \vdots \\ \mathbf{q}(\vec{r}^R_M,\omega) \end{bmatrix} \tag{6.58}$$

Where the operator $\mathcal{L}^R$ can be formulated as the sum of $\mathcal{A}^R$ and $\mathcal{B}^R$,

$$\mathcal{L}^R = \mathcal{A}^R + \mathcal{B}^R \tag{6.59}$$

$$\mathcal{A}^R = \begin{bmatrix} 1 & 0 & \cdots & 0 \\ 0 & 1 & \cdots & 0 \\ \vdots & \vdots & \ddots & 0 \\ 0 & 0 & \cdots & 1 \end{bmatrix} \tag{6.60}$$

$$\mathcal{B}^R = \begin{bmatrix} \mathcal{B}^R_{1,1} & \mathcal{B}^R_{1,2} & \cdots & \mathcal{B}^R_{1,M} \\ \mathcal{B}^R_{2,1} & \mathcal{B}^R_{2,2} & \cdots & \mathcal{B}^R_{2,M} \\ \vdots & \ddots & \vdots & \vdots \\ \mathcal{B}^R_{M,1} & \mathcal{B}^R_{M,2} & \cdots & \mathcal{B}^R_{M,M} \end{bmatrix} \tag{6.61}$$

Hence, the pressure amplitude for M resonators can be expressed by:

$$\tilde{\mathbf{p}} = [\mathcal{L}^R_M]^{-1} \cdot \mathbf{q}^R_M \tag{6.62}$$

Upon substitution of the pressure at the location of the resonator back into the boundary integral equation, the pressure field at any point in the field can be obtained:

$$\begin{aligned} \tilde{p}(\vec{r},\omega) = &\sum_{n=1}^{M} \left\{ \int_{S_n^R} \left[G_\omega(\vec{r},\vec{r}_0) \frac{\partial \tilde{p}(\vec{r}_n^R)}{\partial \vec{n}_0} - \tilde{p}(\vec{r}_n^R) \frac{\partial G_\omega(\vec{r},\vec{r}_0)}{\partial \vec{n}_0} \right] dS_0 \right\} \\ &- \int_V \tilde{f}(\vec{r}_0) G_\omega(\vec{r},\vec{r}_0) dV_0 \end{aligned} \tag{6.63}$$

6.4 Inverse fourier transform

To obtain the evolution of the pressure field with time, applying the inverse Fourier transform as:

$$p(\vec{r},t) = \frac{1}{2\pi} \int_{-\infty}^{\infty} \tilde{p}(\vec{r},\omega) e^{i\omega t} d\omega \tag{6.64}$$

For nearly conjugate symmetric vectors, we compute the inverse Fourier transform faster by specifying the 'symmetric' option in Fast Fourier Transform, which also ensures that the output is real.

6.5 Conclusion

In this section, a 3-D acoustically coupled noise reduction prediction model is proposed for the application of a resonator-based noise mitigation system. The emphasis is placed on the derivation of the pressure at the location of the individual resonator, which is coupled between resonators and the noise source. It is worth mentioning that the resonators also are acoustically coupled with each other. This can be obtained by solving the matrix equation.

The boundary element method could allow us to obtain the pressure field by using the integral of the Green's function. Compared with the finite element model, the analytical model could have a better performance for the large domain simulation by largely saving the computational effort. By building an analytical method, different parameters can be easily modified. In the next chapter, we will discuss a parametric study based on this model. The conclusions and recommendations will be drawn in order to help improve the existing noise mitigation techniques.

Chapter 7

Parametric Study of noise reduction

In this chapter, the theme of parametric study is treated. Based on the three-dimensional acoustically coupled model we developed in the last chapter, a series of properties of the single resonator and arrays of resonators is investigated. First, in order to validate the present analytical model, a finite element model was built in COMSOL Multiphysics. Both numerical results and analytical results are given for further comparison and discussion. In the next section, the influence of the damping coefficient, number of resonators and the mix combination of resonators with different resonance frequencies are investigated. Finally, the summary of the findings can be drawn in the conclusions.

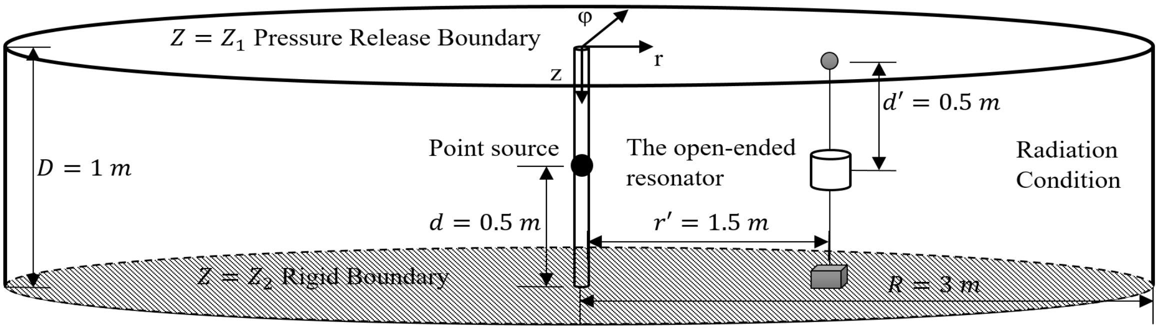

Figure 7.1: Schematic of the field 1

7.1 Validation of single resonator

In this section, the case for a single resonator in a point source field is discussed to check the validity of the theory and this 3-D model. The analytical solutions are compared with the results from the simulation in COMSOL Multiphysics. Considering the computational time for the model in COMSOL Multiphysics needed to achieve sufficient accuracy, the cylindrical-shaped waveguide with a relatively small dimension of z from 0 to $1m$, r from 0 to $3m$ and

ϕ from 0 to 2π was simulated. As shown in the Figure 7.1, the point source is placed at the middle of the domain axis, $(r, z, \phi) = (0m, 0.5m, 0°)$. The single resonator is at 1.5-meter horizontal distance from the domain axis and is at the same water depth with the point source. The boundary conditions for the waveguide are already discussed in Chapter 5.

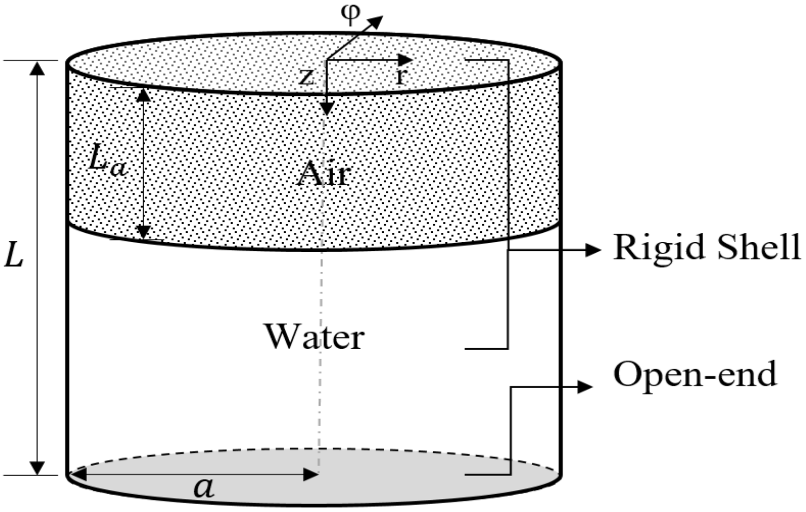

Figure 7.2: Configuration of the resonator

In this analytical model, the resonator was defined as a mass-spring-dashpot system at point r^R. Since the behaviour of the open-ended resonator is not fundamentally influenced by the shell and for the sake of simplification, the impact of the rigid shell is not taken into account in this analytical model, i.e. reflections and scatterring.

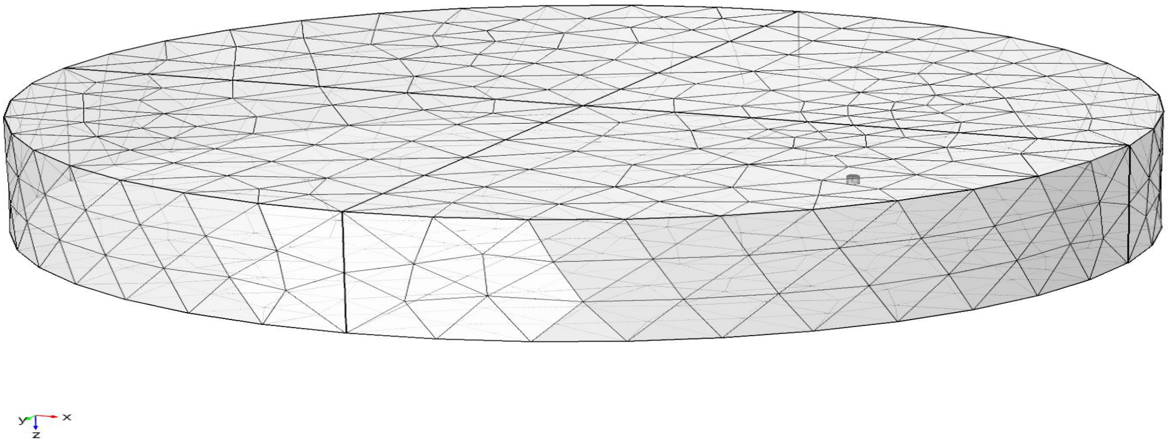

Figure 7.3: The meshed waveguide and resonator

Based on the same geometry and the boundary conditions, the open-ended resonator consists of a rigid shell, air column and water column in the finite element model in COMSOL. The shell of the resonator was selected to be rigid, which means the derivative of the pressure normal to the boundary is zero. The graph of the meshed waveguide and one resonator is shown in Figure 7.3. The resonator in this study has a resonance frequency at 117 Hz, with the dimension of $r = 3.17cm, L = 6.34cm, L_a = 1.3cm$. Because the total volume of the resonator is only $200cm^3$, we place it in a small-sized domain in order to be able to observe the behaviour of the resonator. The configuration of the resonator is shown in the Figure 7.2.

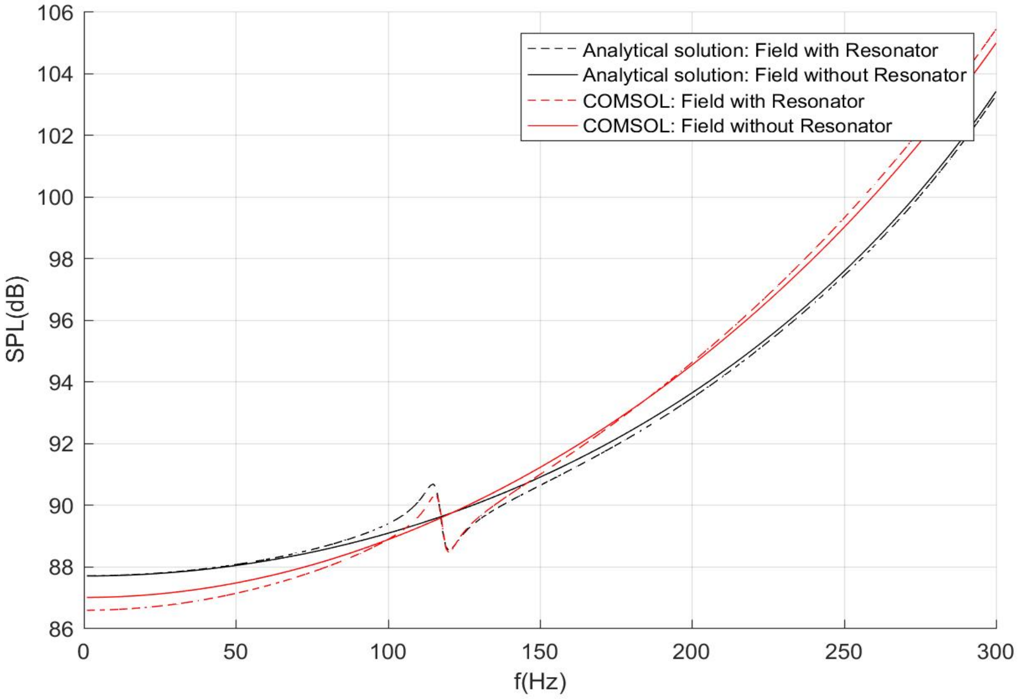

Figure 7.4: Sound pressure level (dB re $1\mu Pa$) at point $(r, z, \phi) = (2.5m, 5m, 0°)$ in the field containing a single resonator

By comparing the computational time for both semi-analytical model and finite element model, the first model could mostly save the CPU time in order to achieve a comparable accuracy. The black and red lines are the sound pressure level in dB at point $(r, z, \phi) = (2.5m, 5m, 0°)$. The solid lines are the sound pressure level in the field only containing a point source, while the dashed lines indicate the influence of the resonator. As shown in the Figure 7.4, the phase shift in two simulations took place both at around the resonant frequency of the single resonator, 117 Hz. However, the shape of the curves slightly deviates at around the resonance frequency.

The deviation between the numerical solution from COMSOL model and the analytical solution from the analytical model can be possibly attributed to the following reasons:

- In the COMSOL model, the open-ended resonator has an layer of rigid shell, while in the analytical model the resonator is simplified as an opening surface with equally distributed pressure generated by the internal motion of the resonator. Therefore, the frequency response function or transfer function obtained by the average pressure in the air domain. The derivation is based on the ideal gas law and the assumption that the pressure is equally distributed on the surface of the opening end;

- The radiation condition in the analytical model could allow the outgoing waves leave the domain without any reflection. Whereas in the COMSOL's model, the cylindrical radiation condition is used. Because the shell of the resonator and the seabed are defined as rigid boundary, the sound waves will be reflected, refracted and scattered. Therefore, the presure waves in the domain are no longer cylindrical waves. Some spurious reflections will take place at the radiation boundaries in COMSOL's model ;

- The accuracy of the fitting between the resonator in the COMSOL model and the ideal single-degree-of-freedom system will depend on the damping ratio of the resonator. For a resonator system with appropriate damping ratio, the fitting can be achieved with high accuracy;

In order to check whether the deviation is mainly caused by the simplifying the pressure P_n along the opening surface of the resonator, the distribution of the P_n and the vertical velocity v_z are obtained from COMSOL model to compare the solution from the analytical model.

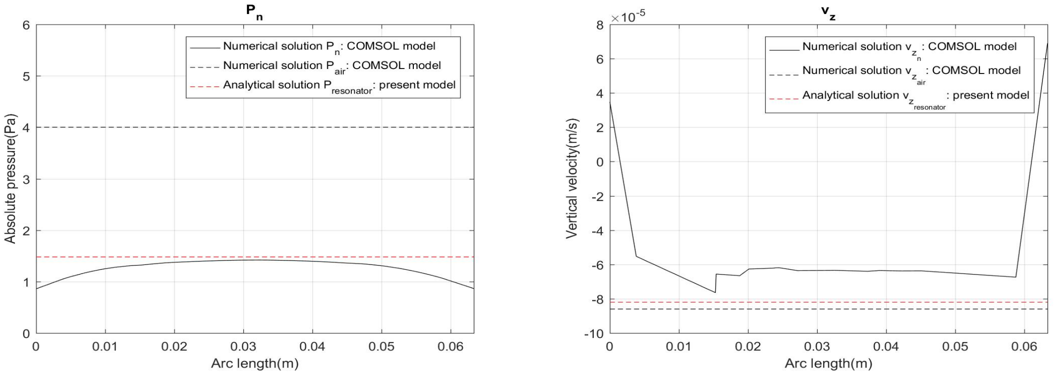

(a) **(b)**

Figure 7.5: Comparison between the results from COMSOL model and analytical model: (a) the pressure P_n; (b) the vertical velocity v_z, where the solid black line represents the results from the COMSOL model along the diameter of the opening end of the resonator, the dashed black line represents the results from COMSOL model along the interface between air and water column, the dashed red line indicate the results from the present analytical model at the middle point of the opening end of the resonator.

As shown in Figure 7.5, we found that the mismatch could come from the numerical results and analytical results in P_n and v_z, where in COMSOL model the pressure varies on the opening surface and in the analytical model the pressure remains constant on the opening surface. This will cause certain disagreement between the two models. From the Figure 7.5, the author found that the P_n derived at the first step of the model is between the pressure at the air-water interface of the resonator and the pressure at the opening end. However, to capture the behaviour of the resonator in a better way, it is recommended not to choose to average the pressure along the opening end but integrate the pressure over the whole surface.

7.2 Parametric study

In this section, we will discuss the potential factors that could influence the performance of the resonator curtain. The discussion will start with the individual resonator. The influence of the internal resistance of the resonator will be investigated through the comparison of using resonators with different damping coefficients. The performance of the single resonator can be quantified through Q factor and the noise reduction spectrum. The combination of the resonators with multiple resonance frequencies could also improve the performance of the resonator. To a large extent, the void fraction of the resonator system could also determine the intensity of the noise reduction, i.e. by changing the number of the resonators or the distance between the resonator curtain and the noise source. The direction of the resonator has nearly no influence on the noise reduction level as we know it's due to the relatively small dimension of the resonator compared with the wave lengths for low-frequency sound waves.

In this study, the waveguide with 10-meter water depth and 3-meter range contains a monopole point source in the middle of the domain. The source is monochromatic and equally strong in all directions. The source strength of the following cases is assumed to be $S = 4\pi$ with the unit N/m. The resonator array will be deployed at the target locations for different cases. To the author's knowledge, the presented model could be used to determine the optimal design of the resonator system and recommendations will be proposed for the future design. By choosing the proper parameters for the resonator curtain, one can optimise the design of a resonator-based noise mitigation system.

7.2.1 The influence of the internal resistance of the resonator

In this section, the influence of the internal resistance of the resonator will be investigated through comparing resonators with different damping coefficients. In the configuration examined hereafter, the resonator is placed at $(r, z, \phi) = (1.5m, 5m, 0°)$, while the point source is placed in the middle of the domain. First, the frequency response function for different resonators needs to be computed by the COMSOL model. Then by substituting the transfer function into the semi-analytical model, we could obtain the sound pressure level in the frequency domain at every point in the field.

COMSOL model

The finite element model in COMSOL Multiphysics needs to be built in order to find the frequency response function of the open-ended resonator. It is worth mentioning that the frequency response function for individual resonator varies in different water depths. Since the air column in the resonator can be compressed due to the varying static pressure, this could shift the resonance frequency to the higher range. In the following cases, we manually tuned the resonators to the same resonance frequencies by defining the proper slenderness. For the sake of simplicity, the same transfer function is used for the resonators at the same resonance frequency but at different water depth. This can cause some small deviations with the real situation due to the influence of the open area.

As shown in figure 7.8, the additional internal resistances of the resonators could be added by using the porous material on the internal top side of the open-ended resonator. The porous

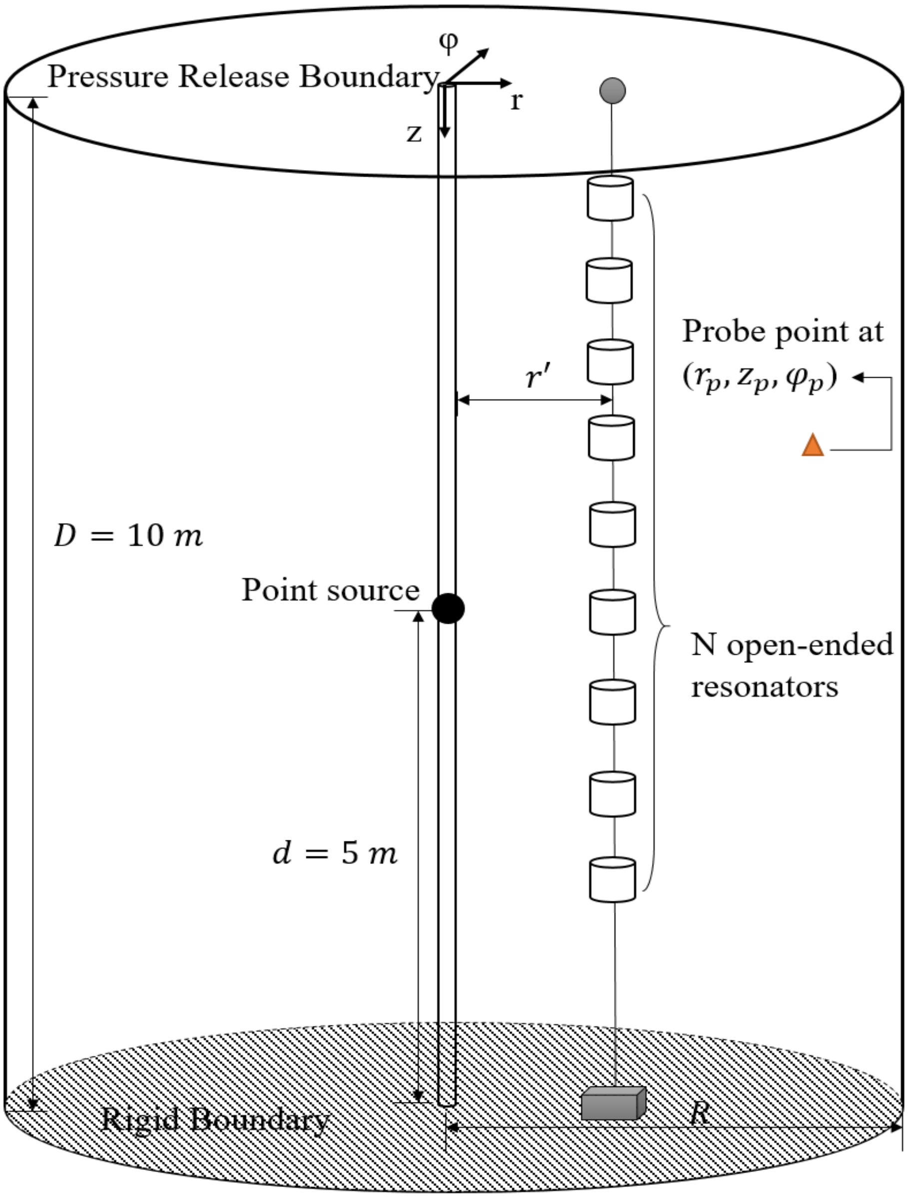

Figure 7.6: Schematic of the field 2

elastic material can be glass fiber, glass wool and rock wool fill. The empirical poroacoustic model we used is Delany-Bazley-Miki model. The flow resistance R_f normally ranges from $1 Pa \cdot s/m^2$ to $50 \times 10^3 Pa \cdot s/m^2$ for the above mentioned material. It is worth to mention that Delany-Bazley-Miki model is only applicable to the range $0.01 < X < 1$, with $X = \rho_f \cdot f/R_f$. The other models, i.e. Zwikker-Kosten model, wood model, could also be considered for further development of resonators.

In this study, the flow resistivities are defined as 1, 10, 100, 1000, 5000 $Pa \cdot s/m^2$ for five cases, respectively. The other properties for the resonators remain same for each case. We could read from Figure 7.9 that when we add the material with a higher flow resistivity, more energy is damped by the resonator. In the Figure 7.9, the average sound pressure level in the air

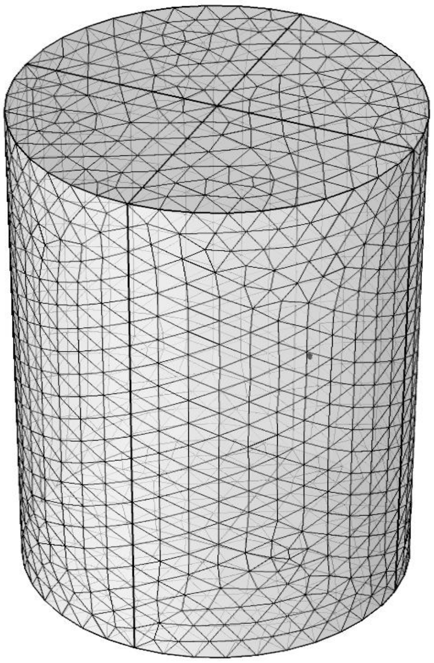

Figure 7.7

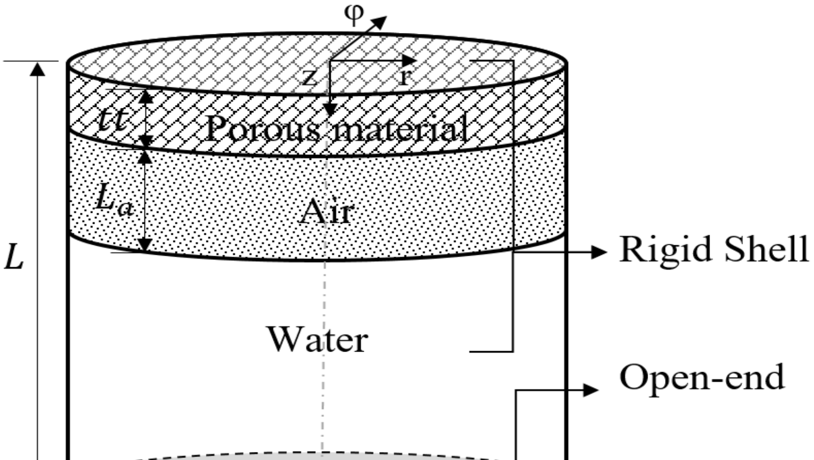

Figure 7.8: Configuration of the damped resonator

domain is shown in the frequency domain. With a higher flow resistivity, the peak of the curve dropped down, and the resonance frequency shifted to the lower range. The performances of this series of resonators agree with the behaviour of a single-degree-of-freedom system.

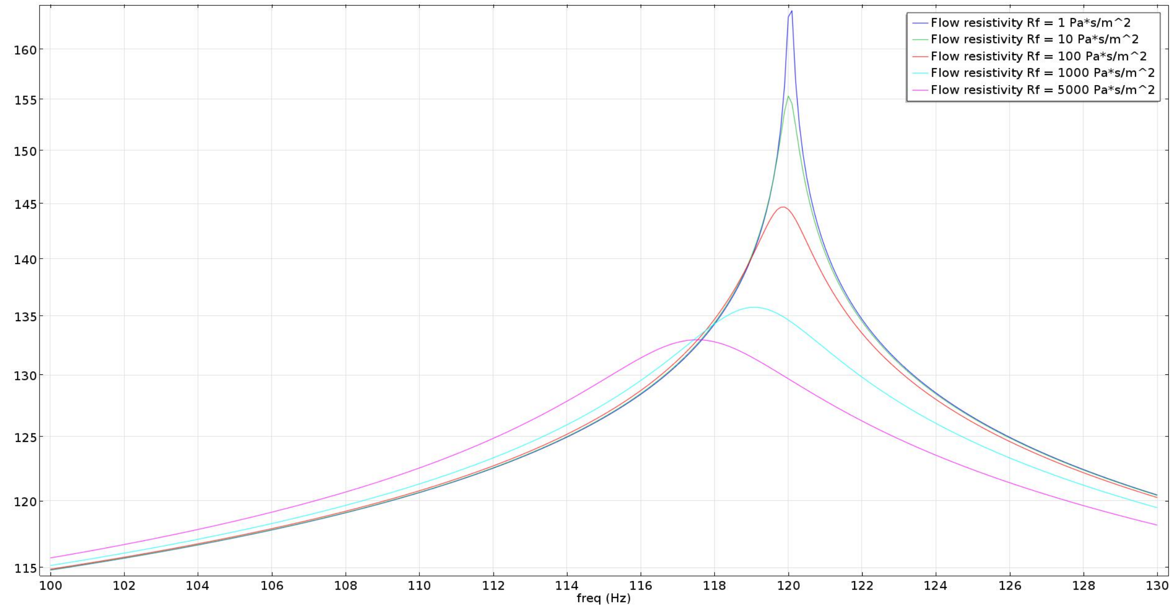

Figure 7.9: COMSOL: The average sound pressure level (dB re $1 \mu Pa$) in the air domain of the resonator with different flow resistivities

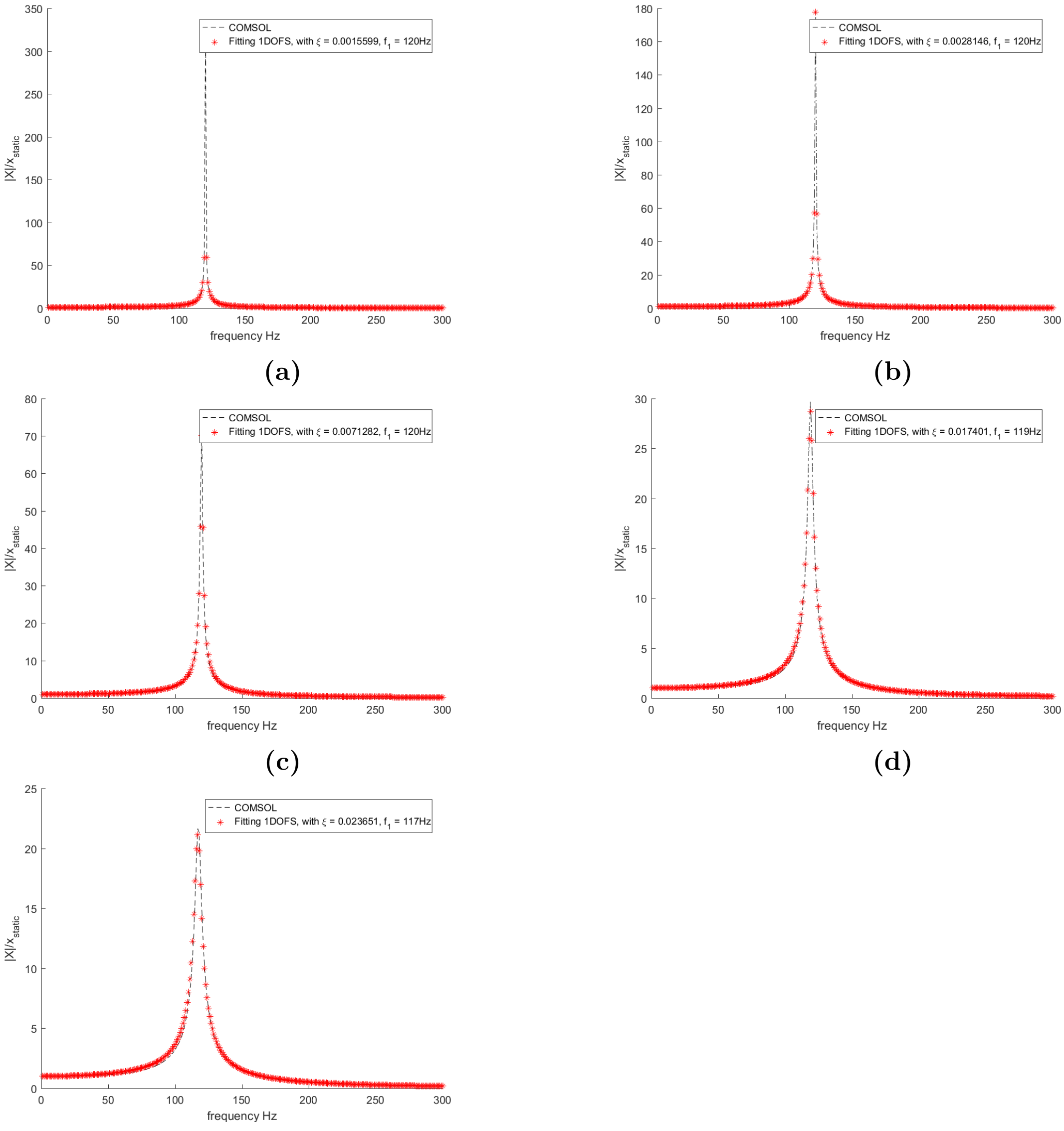

(a) (b) (c) (d) (e)

Figure 7.10: Fitting magnification factors for the open-end resonators with different flow resistivities: (a) $R_f = 1Pa{\cdot}s/m^2$; (b) $R_f = 10Pa{\cdot}s/m^2$; (c)$R_f = 100Pa{\cdot}s/m^2$; (d)$R_f = 1000Pa{\cdot}s/m^2$; (e)$R_f = 5000Pa{\cdot}s/m^2$;

Frequency response function

Given the pressure in the air domain of the resonator, the equivalent coefficients m, ξ, k can be derived by fitting the curve of the magnification factor in frequency domain. The theory for the derivation of the transfer function has been discussed in the Chapter 3.

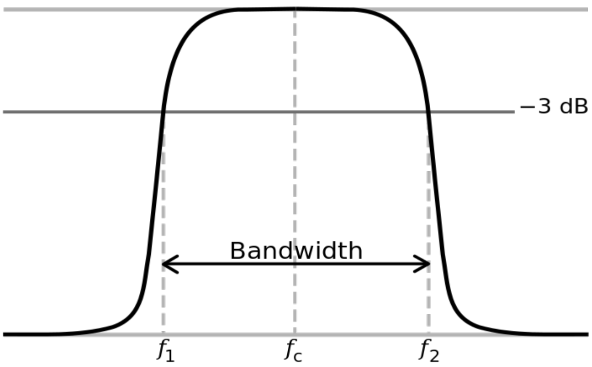

Figure 7.11: The definition of Q factor

Q factor

The Q factor of the open-ended resonator could be estimated as $f_c/\Delta f$, where the bandwidth Δf indicates $f_2 - f_1$, f_c is the center frequency of the response. The quality factor Q represents the rate of the stored energy in the resonator to the energy loss. As a general rule of the thumb, when the quality factor is less than $\frac{1}{2}$, the system does not oscillate and is said to be overdamped. Similarly, a system with Q factor larger than $\frac{1}{2}$ is considered as the underdamped system. The intermediate quality factor represents that a system is critically damped.

Table 7.1: Acoustic behaviour for open-ended resonators with various porous materials

Index	$R_f (Pa{\cdot}s/m^2)$	Resonance frequency(Hz)	Q factor	Damping coefficient
1	1	120	240	1.56×10^{-3}
2	10	120	200	2.81×10^{-3}
3	10^2	120	60	7.13×10^{-3}
4	10^3	119	30	1.74×10^{-2}
5	5×10^3	117	24	2.37×10^{-2}

The higher flow resistivity the porous material we use, the lower Q factor the resonator will have. This physically means that more energy is damped by the resonator with a higher R_f material inside. For the resonator with minimal damping coefficient, although there are large part of the energy is stored in the resonator. The energy in the sound wave shifts into the higher frequencies, and the motion of the resonator raises up to very high amplitude. Although the energy would be trapped by the resonator, it also causes destructive interference for the sound waves around the resonance frequency as shown in the figure 7.12 (a) and (b). In contrast, when we increase the internal resistivity of the resonator, the amplitude of

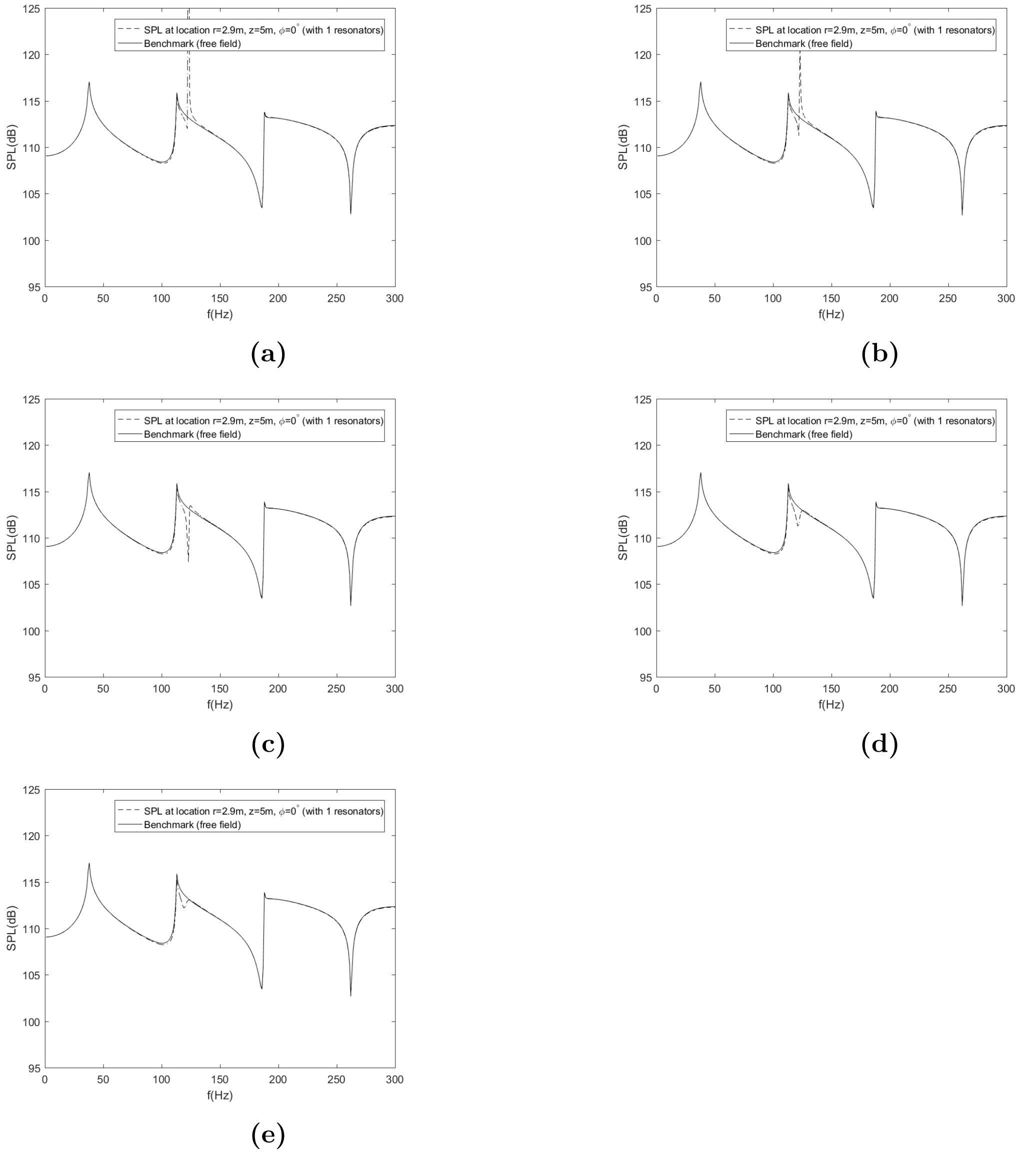

(a) **(b)** **(c)** **(d)** **(e)**

Figure 7.12: Sound pressure level (dB re $1\mu Pa$) at point $(r, z, \phi) = (2.9m, 5m, 0°)$ in the field containing one resonator with different flow resistivities: (a) $R_f = 1Pa{\cdot}s/m^2$; (b) $R_f = 10Pa{\cdot}s/m^2$; (c)$R_f = 100Pa{\cdot}s/m^2$; (d)$R_f = 1000Pa{\cdot}s/m^2$; (e)$R_f = 5000Pa{\cdot}s/m^2$;

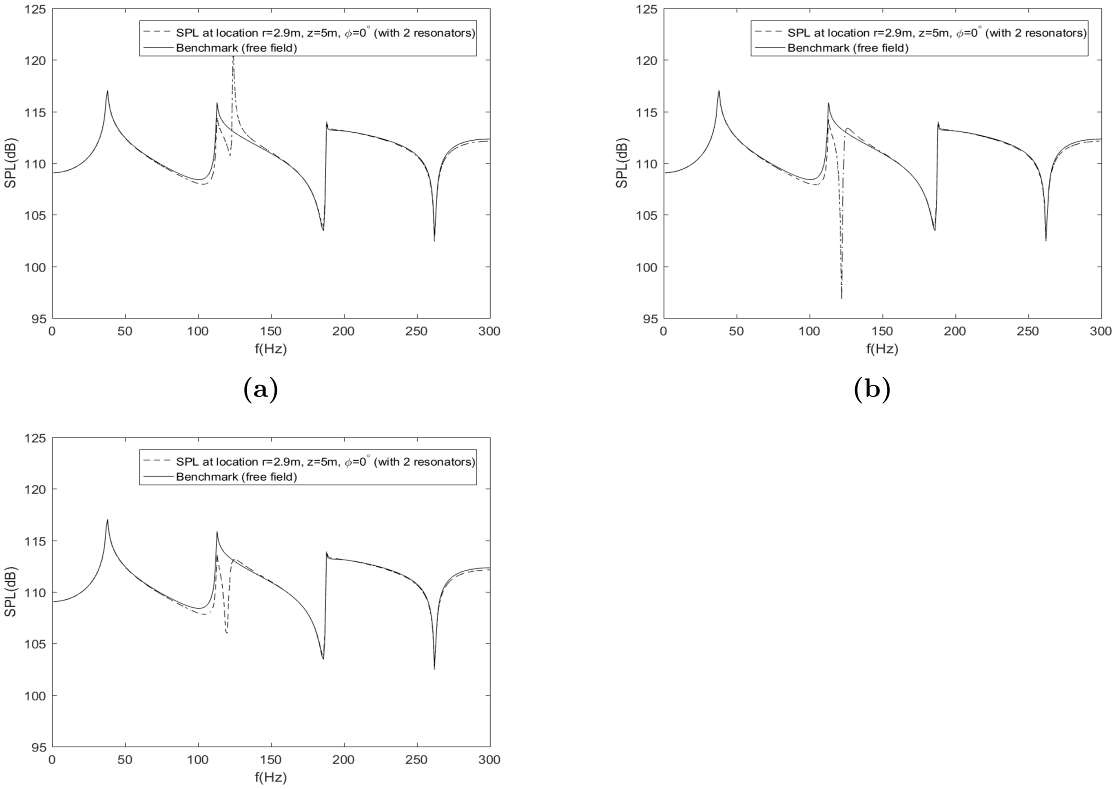

(a)

(b)

(c)

Figure 7.13: Sound pressure level (dB re $1\mu Pa$) at point $(r, z, \phi) = (2.9m, 5m, 0°)$ in the field containing two resonators with different flow resistivities: (a)$R_f = 100 Pa{\cdot}s/m^2$; (b)$R_f = 1000 Pa{\cdot}s/m^2$; (c)$R_f = 5000 Pa{\cdot}s/m^2$;

the destructive interference becomes lower, while the attenuation increases. Until the flow resistivity reaches a threshold, the peak of the noise reduction starts to reduce, and less energy is stored in the resonator.

When there are two resonators in the domain, the influence of the internal resistance is intensified compared to single resonators. In figure 7.13, the SPL in the field containing two resonators with three different flow resistivities are plotted. In the above experiments, we could see that the internal resistivity of the resonator is a critical parameter that determines the performance of the resonator. By balancing the noise reduction level and the destructive interference, we could find an *optimum* value for the damping coefficient to improve the performance of the resonator.

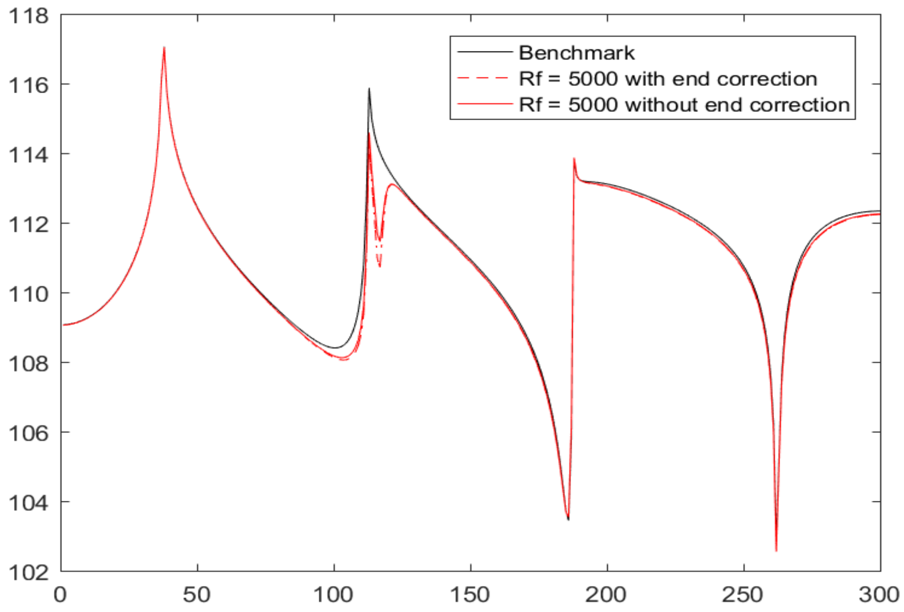

Figure 7.14: The influence of the end correction on the resonator

As shown in the figure 7.14, special attention needs to be given to the influence of the end correction of the open-ended resonator. We have discussed the physical reason of adding an end correction factor(Chapter 3).

7.2.2 The influence of number of resonators

Similarly as the air bubble curtain system, the void fraction could be one of the critical parameters that determine the performance of the resonator-system. However, we could approach this problem by first considering the number of resonators in an array. This section compares the use of a single resonator, two identical resonators, three identical resonators and two resonators with different resonance frequencies to reduce the sound level.

In the following cases, the flow resistivities of the resonators are all defined as $5000 Pa{\cdot}s/m^2$. The array of the resonators is put in the domain at $r' = 1m, \phi = 0°$, when there is more than

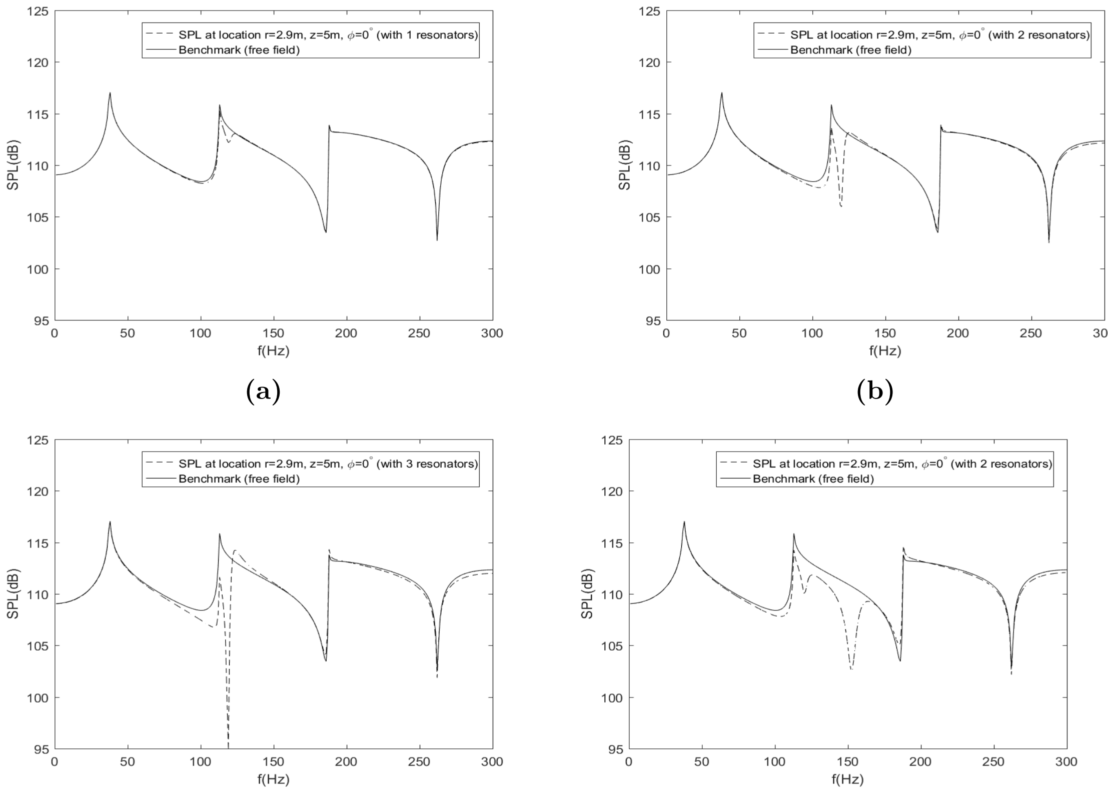

(a) **(b)**

(c) **(d)**

Figure 7.15: Sound pressure level (dB re 1μ Pa) at point $(r, z, \phi) = (2.9m, 5m, 0°)$ in the field containing different number of resonators with $R_f = 5000 Pa{\cdot}s/m^2$: (a) Single resonator; (b) Two resonators; (c) Three resonators; (d) Combined two resonators with different resonance frequency.

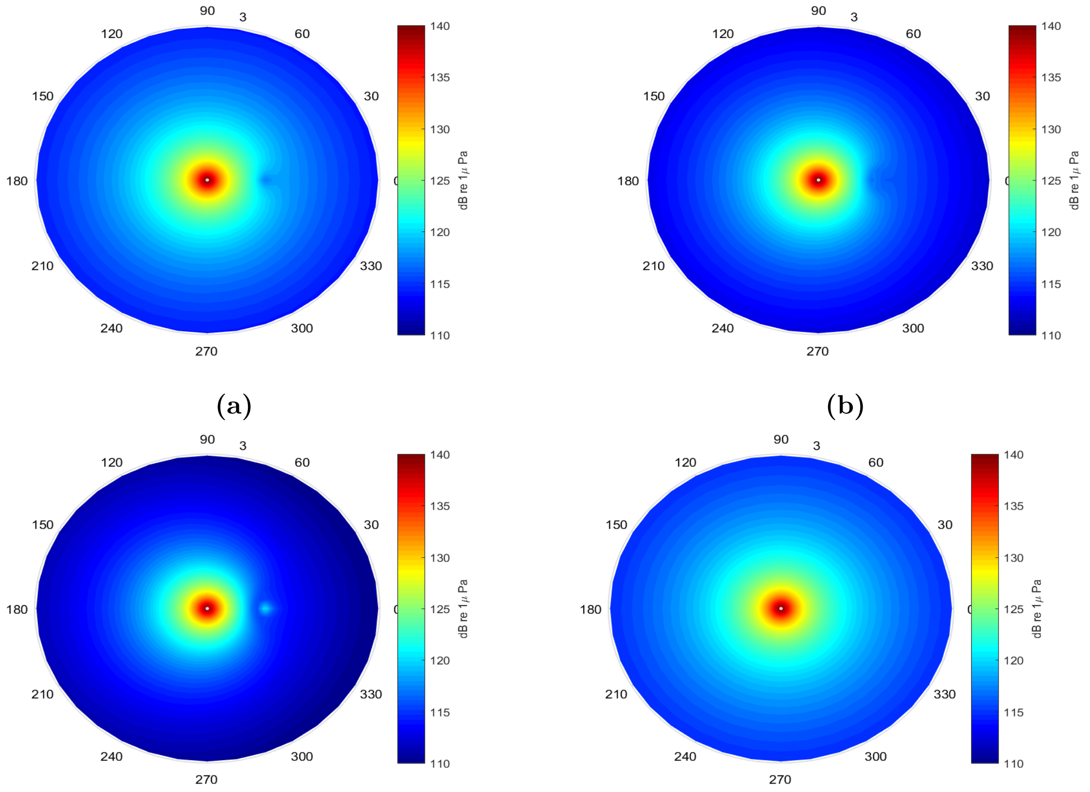

(a) (b) (c) (d)

Figure 7.16: Sound pressure level (dB re 1μPa) distribution at cross section z=5 m at resonance frequency 117 Hz in the field containing different number of resonators: (a) Single resonator; (b) Two resonators; (c) Three resonators; (d) Free field.

one resonator. We keep the distance between individual resonators as 1 meter and keep the centre of the array at 5-meter water depth. Apparently, with more resonators in the array, the peak of the noise reduction increases and more energy is trapped by the resonators. The sound pressure distribution at the cross section at 5-meter water depth is shown in the figure 7.16. It's also worth to mention that the resonator array could not only influence the pressure field on the side of the resonator but also the whole field. To the author's knowledge, the dimension of the resonator is much smaller than the wave length. Thus, the direction of the opening-end has nearly no influence on the pressure wave. The resonator itself works as a secondary sound source. Thus the influence of the resonator is equal in all directions and propagates radially.

7.2.3 The influence of different combination of resonators

As shown in figure 7.15 (c) and (d), the use of two different types of resonators to reduce the sound level could lead to a wider attenuation spectrum than two identical resonators. Also, the destructive interference can be eliminated by adding another resonator in the vicinity of the *non-target* frequency. The behaviour of multiple resonance frequencies gives us insight in potential improvement of the performance of the system through an optimal combination of a series of resonators with proper damping coefficient and resonance frequency.

In order to discuss this problem from a holistic perspective, the two cases for two and six mixed resonators are shown below in the figure 7.18.

The sound pressure level distribution at the cross section of 5 meter water-depth is also plotted for the case with two mixed resonators and six mixed resonators, respectively.

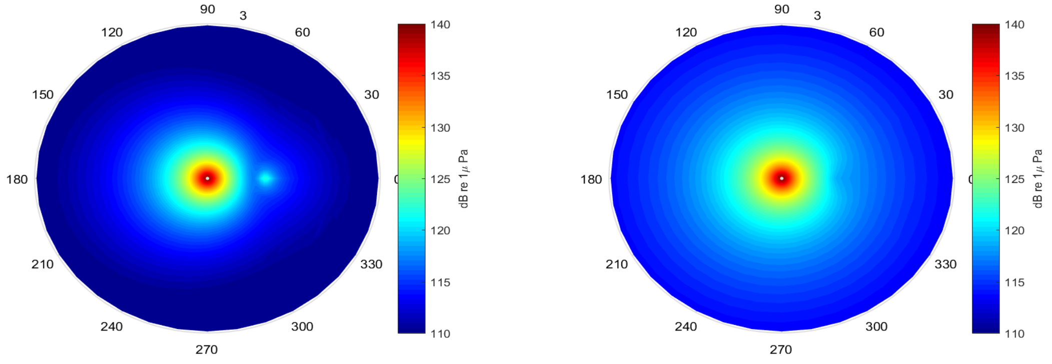

(a) (b)

Figure 7.17: Sound pressure level (dB re $1\mu Pa$) distribution at cross section z=5 m at resonance frequency 117 Hz:(a) Six mixed resonators; (b) Two mixed resonators;

7.2.4 The influence of the inclined angle

As we already discussed in Chapter 3 and 6, the behaviour of the open-ended resonator can be approximated by the theory of SDoF system. Using BEM, the contribution of the open-ended resonator to the pressure field is given by the surface integral over the opening end of

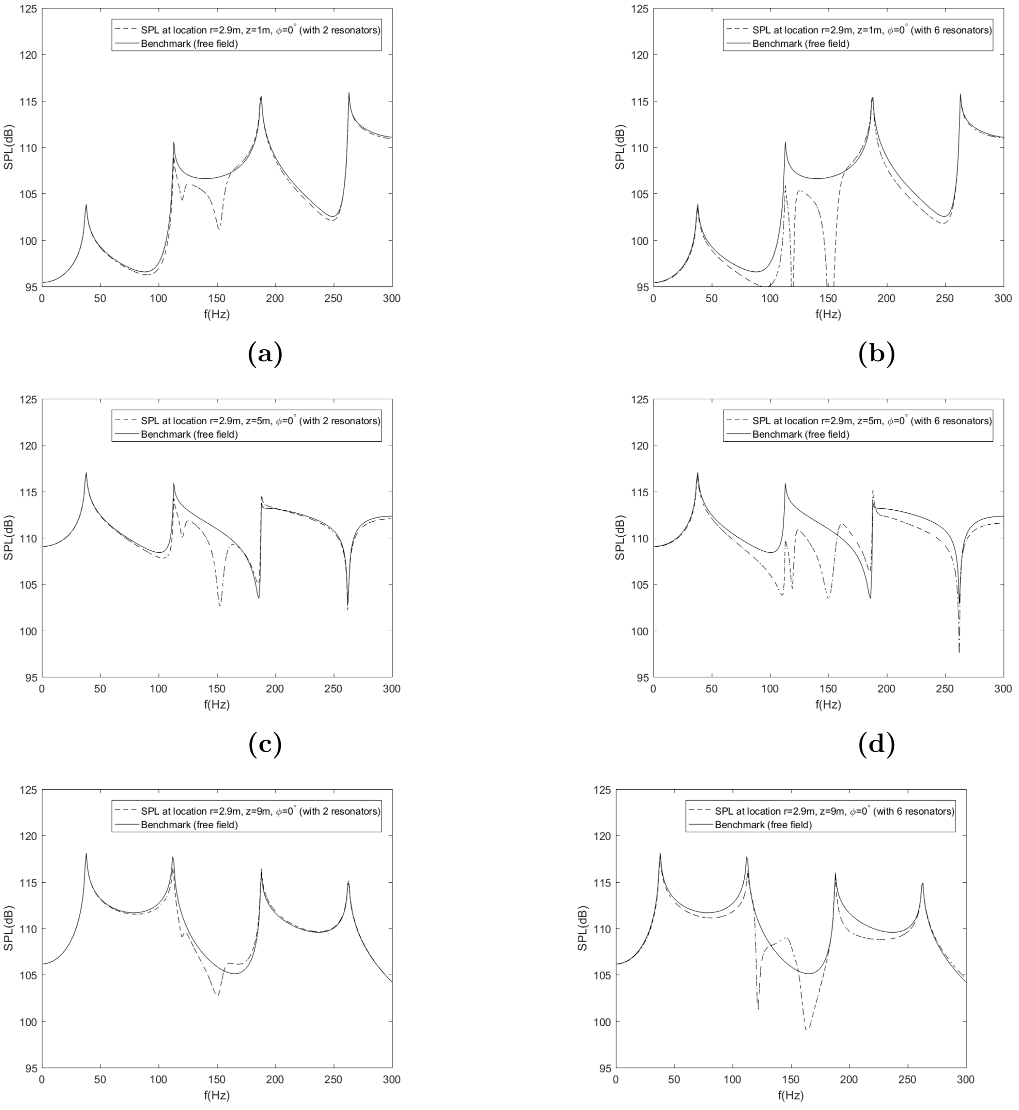

(a) **(b)**

(c) **(d)**

(e) **(f)**

Figure 7.18: Different number of resonators: (a) Two mixed resonators: SPL (dB re $1\mu Pa$) at point $(r, z, \phi) = (2.9m, 1m, 0°)$; (b) Six mixed resonators: SPL (dB re $1\mu Pa$) at point $(r, z, \phi) = (2.9m, 1m, 0°)$; (c) Two resonators: SPL (dB re $1\mu Pa$) at point $(r, z, \phi) = (2.9m, 5m, 0°)$; (b) Six resonators: SPL (dB re $1\mu Pa$) at point $(r, z, \phi) = (2.9m, 5m, 0°)$; (e) Two resonators: SPL (dB re $1\mu Pa$) at point $(r, z, \phi) = (2.9m, 9m, 0°)$; (f) Six resonators: SPL (dB re $1\mu Pa$) at point $(r, z, \phi) = (2.9m, 9m, 0°)$;

the resonator. In this surface integral, the normal derivative of the pressure and the Green's function both depend on the local position of the resonator, in other words, the inclined angle of the resonator.

For the sake of simplification, the surface integral in the boundary integral equation is simplified by the surface area times the contribution from the central point of the opening end. Therefore, in the present model, the first term in surface integral could not take into account the influence of the inclined angle without modifying the FRF. Although the obtained normal derivative of the Green's function is position-dependent, the second term in the surface integral accounts only for a relatively small amount of the contribution from the resonator. Therefore, in order to investigate the influence of the inclined angle, one will need to derive the frequency response function based on the every new position of the resonator.

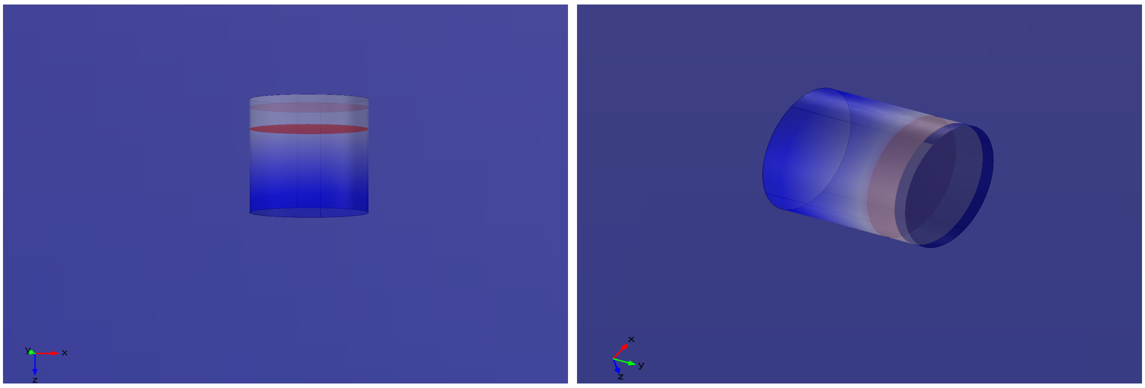

(a) **(b)**

Figure 7.19: Two positions of resonators in the acoustic domain:(a) opening end facing the positive z direction; (b) opening end facing the negative r direction.

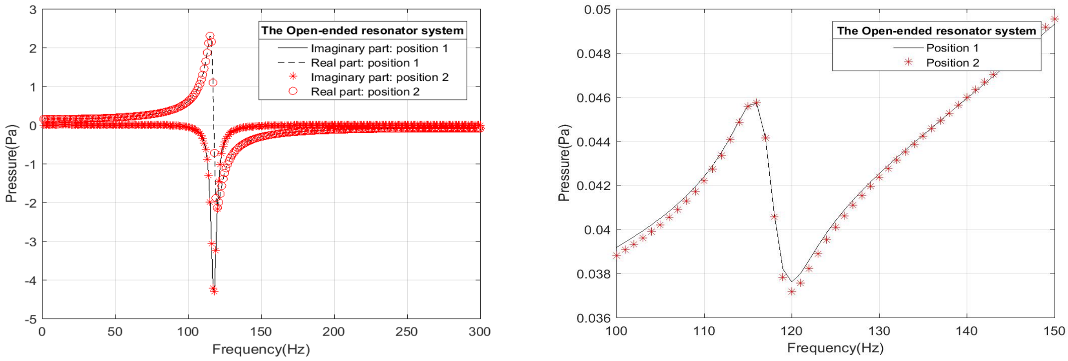

(a) **(b)**

Figure 7.20: Two positions of resonators in the acoustic domain:(a) Position 1: opening end facing the positive z direction; (b) Position 2: opening end facing the negative r direction.

As shown in Figure 7.19, the two finite element models are developed in COMSOL in order to investigate the acoustic behaviour of resonators in different inclined angles. The resonator is placed at the location $(r, z, \phi) = (0m, 0.5m, 0°)$ in the cylindrical-shaped domain with the dimension of z from 0 to $1m$, r from 0 to $3m$ and ϕ from 0 to 2π. The waveguide has the same configuration, boundary and radiation conditions with the validation case.

The result from this study shows that the position of the resonator has a slight influence on the pressure field for a single point source field for this specific case. In this case, the configuration of the resonator is relatively small compared with the long wavelength given the low-frequency sound waves. However, in practical case, the influence of the inclined angle still needs further investigation for the sound radiation from pile driving. The sound waves generated by offshore piling are in the form of *Mach cone* or *pressure cone*, which is formed with a cone angle ϕ around 17° to 18°. Therefore, the resonator is likely to have an optimal inclined angle, which could achieve largest noise reduction level against the *Mach cone*. However, it still requires further study for the field with the use of a complete resonator system.

7.2.5 Conclusion

In this chapter, the theme of three-dimensional noise reduction prediction model with the use of resonator arrays is treated. The influence of the internal resistance of the resonator, number of the resonators and different combination of resonators have been discussed.

Based on the results from this chapter, we find the critical parameters that could determine the behaviour of the resonator system. By adding the additional internal damping in the resonator, one could widen the frequency range of the noise reduction and eliminate the destructive interference in the vicinity of the target frequency. By choosing a proper combination of different resonators, one can absorb more energy by the internal vibration of the resonator and dissipate more energy by the porous material. The void fraction is another measure index of the performance of the resonator, which is determined by both the number of the resonators we use and the distance between the resonator system and the noise source. Obviously, the more resonators applied, the more noise reduction one can achieve. Whereas, the void fraction is also related to the ballast mass that is used to compensate for the buoyancy of the air. Therefore, it is advisable to find the optimal structure and proper location of the resonator-based system in order to achieve our target noise reduction level.

The present model describes solely the resonator as an ideal SDoF system. In this study we focus on the resonance effect, which is considered as the primary mechanism of the noise reduction. But in reality, multiple reflections, refraction, and scattering effects could also affect the pressure field. This part would need further investigation.

Chapter 8

Model Application

In this chapter, we will focus on several cases of the model application. The first section will focus on finding the optimal damping ratio for a single resonator, by using the damping ratio varying from two percent to twenty percent. This provide a case of parameter optimization for a resonator with better performance. The second section presents a field simulation with the use of 15 resonators in three arrays. The configuration of the field is chosen based on the upcoming lake test. The results given in the pressure field show an effective noise reduction at the target frequency. In the third part, the sound radiation from pile driving is represented by using an array of the phased point sources. The obtained results of this model are found to be in a good qualitative agreement compared to a literature example. The arrays of resonators are used in the field to mitigate the pressure waves generated from the phased point source signals, which could show us the process of how the resonators interfere with the propagation of the pressure waves.

8.1 Parameter optimization

As we already discussed in the last chapter, the damping coefficient has a large influence on the acoustic performance of the resonator. To find the appropriate damping, we compare the behaviour of the resonators with different damping ratios. The first step is to obtain the frequency response functions for various damping ratios. In this case, we assume that the resonators behave like a mass-spring-dashpot system. Therefore, by changing the damping ratio in the ideal single-degree-of-freedom system, we could directly obtain the corresponding transfer functions as shown in Figure 8.1.

To have an overview of the behaviour of the individual resonator, we put each resonator in the domain with the dimension of $(r \times z \times \phi) = (5m \times 10m \times 360°)$. From Figure 8.4, we read that due to the relatively small size of the resonator, the influence of the resonator to the field is quite small, especially when the damping ratio reaches 15 pertent. Therefore, we increase the number of the resonator to five, and compare the resonators with a damping ratio of 0.1, 0.05, 0.02, respectively. The sound pressure levels at two points $(r, z, \phi) = (2.9m, 5m, 0°)$

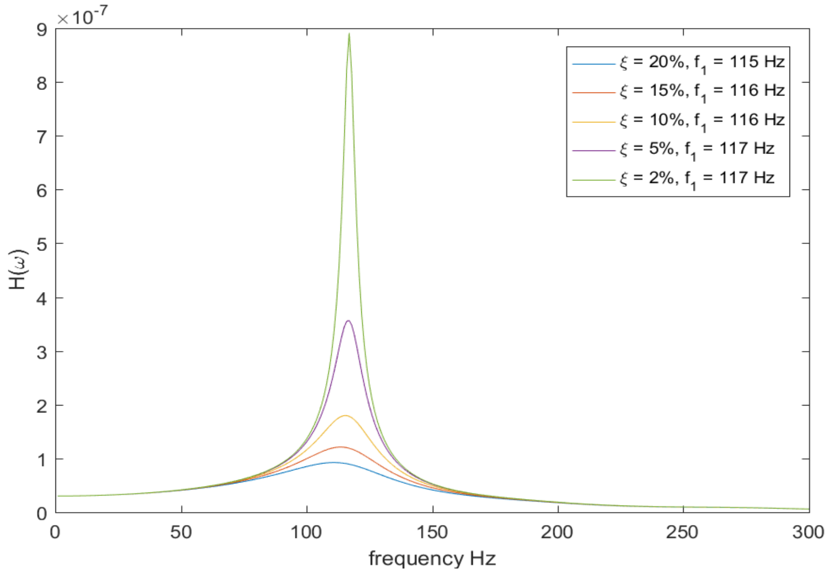

Figure 8.1: The frequency response functions for various resonators with different damping coefficients

and $(r, z, \phi) = (2.9m, 9m, 0°)$ are shown in Figure 8.4, one point is close to the sea surface, the other one is close to the seabed. We could read from the graph that, the resonator with a damping coefficient higher than 0.05 will cause no clear destructive interference, although the less the damping the more noise reduction level at the target frequency can be achieved. Therefore, the resonators with five percentage damping would be recommended to be used. However, we know that in reality the damping coefficient is relatively difficult to measure but still we could increase proper damping through adding porous material as we discussed in the last chapter or other foam material to achieve a better performance.

8.2 Field simulation

In this section, a field simulation for an upcoming lake test is conducted in order to estimate the ideal noise reduction level and the proper number of resonators needed. The test will take place in the lake with 20 meter water depth. The underwater sound waves for this test will be generated by a marine speaker, which will be placed in the middle of the steel frame. Several arrays of resonators will be installed on the steel frame, where is about 0.55 meter distance from the noise source. We assume that the noise source can generate sound waves from 1 Hz up to 300 Hz. The sound pressure level distribution at one cross section of the field is shown in frequency domain.

By using three arrays of resonators, each array containing five resonators, at one of the target frequencies, 153 Hz, the noise reeduction level can be achieved to more than 10 dB. From Figure 8.2, we found that the resonator system effectively reduce the pressure level in the field at the coherent frequency. To verify this simulation, the results from the experiment will be needed for the further study.

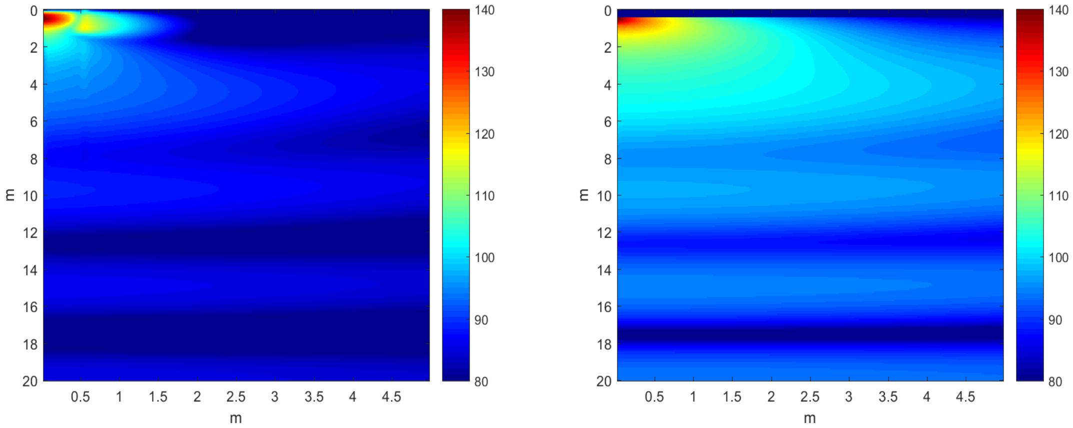

(a) **(b)**

Figure 8.2: Pressure field at 153 Hz (dB re $1\mu Pa$): (a) with 15 resonators; (b) without 15 resonators;

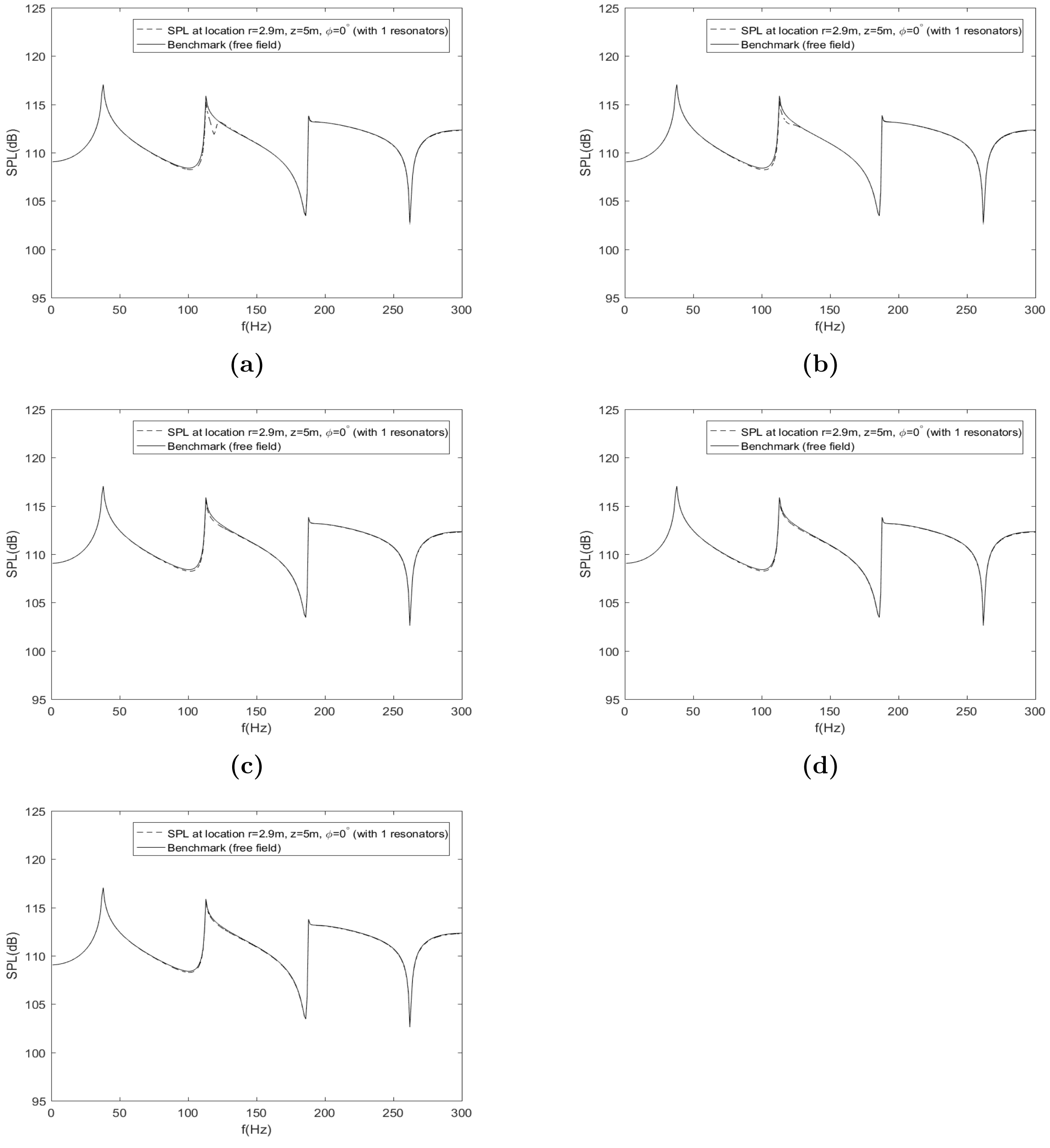

(a) **(b)** **(c)** **(d)** **(e)**

Figure 8.3: Comparison of the analytical solutions of SPL (dB re $1\mu Pa$) at point $(r, z, \phi) = (2.9m, 5m, 0°)$: (a) Single resonator with $\xi = 0.02$; (b) Single resonator with $\xi = 0.05$; (c)Single resonator with $\xi = 0.1$; (d)Single resonator with $\xi = 0.15$; (e)Single resonator with $\xi = 0.2$;

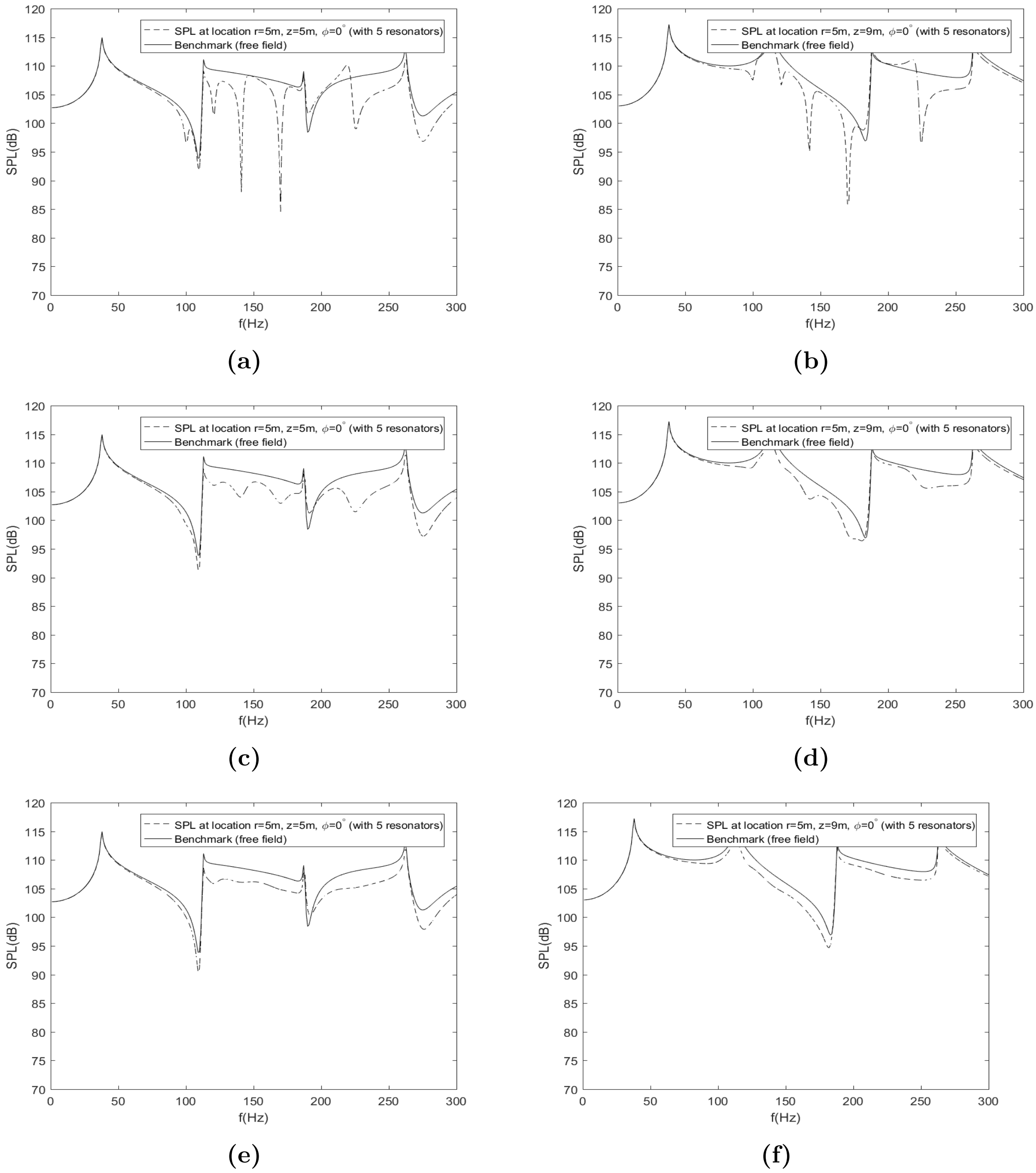

(a) (b) (c) (d) (e) (f)

Figure 8.4: Comparison of the analytical solutions of SPL (dB re $1\mu Pa$) at point 1 $(r, z, \phi) = (2.9m, 5m, 0°)$ and point 2 $(r, z, \phi) = (2.9m, 9m, 0°)$: (a) Five resonators with $\xi = 0.02$ at point 1; (b) Five resonators with $\xi = 0.02$ at point 2; (c) Five resonators with $\xi = 0.05$ at point 1; (d) Five resonators with $\xi = 0.05$ at point 2; (e) Five resonators with $\xi = 0.1$ at point 1; (f) Five resonators with $\xi = 0.1$ at point 2;

8.3 The prediction of the noise reduction with the use of a resonator-based noise mitigation system

8.3.1 The representation of the sound radiation from pile driving

In this section, in order to represent the sound radiation from pile driving, a method of using an array of phased point sources is used, which is introduced by Reinhall and Dahal [1]. The pulse delay in the point source is in order to account for the waves travelling down along the pile at the supersonic speed, $c_p = 5048m/s$. The results from this method have shown a qualitative agreement with results from the wavenumber integration simulation [21].

For ith point source in the array, the source in frequency domain can be expressed by[1],

$$s_i(\vec{r}, f) = G(\vec{r}, \vec{r_i}, f)A(f)e^{i2\pi f\tau_i} \tag{8.1}$$

where τ_i represent the time delay for each point source i, which is equal to source depth z_i divided by the supersonic speed c_p. $A(f)$ is the empirical amplitude weighing spectrum, which is used to estimate the sound radiation from pile driving.

The superposition of the array of point sources can be used to represent the sound source as,

$$S_1(\vec{r}, f) = \sum_{i=1}^{N} s_i(\vec{r}, f) \tag{8.2}$$

It gives the complex amplitude spectrum of the first arrival of the sound generated from the phased point sources, which represents the form of the pressure cone or Mach cone. For the sake of simplicity, the other subsequent arrivals are not taken into account in this study.

In this case, we choose 39 phased point sources along the pile axis with the spacing 1 meter, the water depth for the field is 40 meter. Before the inverse Fourier transform, the pressure field in frequency domain is zero-padded in order to achieve a fine time-step interpolation in time domain. As shown in Figure 8.5, the pressure field is obtained in time series. The results show that no signal can be emitted before $t = \tau_i$ for each point source $i = 1...N$. The signal in this case is determined as a single wave with a frequency of 300Hz. Figure 8.5 shows that the longitudinal impulse waves travel down the pile with a supersonic speed c_p, which forming the inclined *Mach cone* in the water column. It can be seen that the inclination of the wavefront has been qualitatively reproduced, compared with the FE-model [1] and WI-model [21]. Therefore, based on the comparison of the results, we can conclude that this method is able to represent the main characteristics of the sound radiation from pile drving. It also allows us to predict the sound pressure level at large distance from the pile axis.

8.3.2 The noise reduction prediction by using the open-ended resonator system

Based on the representation of the sound radiation from pile driving, the wave field is investigated further with the implementation of the resonator-system for the predictions of the noise reduction level. The domain contains an open-ended resonator-system in 10-meter water depth, with 19 point sources spacing 0.5 meters. Various positions and configurations of

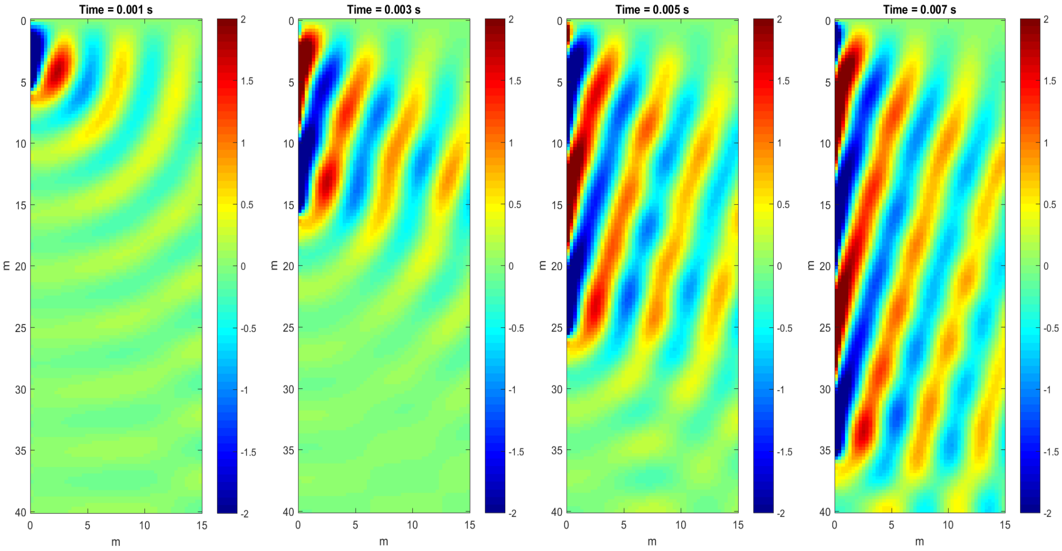

(a) t = 1 ms **(b)** t = 3 ms **(c)** t = 5 ms **(d)** t = 7 ms

Figure 8.5: Pressure field in time domain with an array of 39 phased point sources

the resonator-system are used in this study in order to find the critical parameters that have large influences on the noise reduction. The position of the resonator system has a large influence on the performance of noise reduction. In this case, the resonator-arrays are placed at $\Delta r = 1.5m$ and $\Delta r = 10m$, respectively. Each resonator-system consists of 20 arrays equally distributed around the source axis as a resonator curtain, in which 20 resonators are placed on each array. For the sake of simplification, there are 10 types of resonators are used in total. However, in the practical case, the acoustic behaviour of the open-ended resonator will depend on the water depth and the configuration. In other words, the number of the types of resonators can be estimated as $N_{depth} \cdot N_{resonator}$, in which $N_{resonator}$ indicates the number of different configurations of resonators, and N_{depth} represents the number of different water depths for one resonator with a certain configuration.

As shown in Figure 8.6, the black line with asterisk indicates that the level of noise reduction is higher when the resonator system is placed near the source axis ($\Delta r = 1.5m$), compared with the red line when the system is placed at the far position ($\Delta r = 10m$). The number of the resonators for two cases is identical, when the system is placed at a longer horizontal distance from the source axis, the interval between every two arrays of resonators is increased. Therefore, the acoustic waves can pass through the resonator curtain with less influence.

Following the discussion on the position of the resonator system, the different number of resonators used in the system is investigated further in this case. In chapter 7, we already discussed the influence of the number of resonators in a parametric study, in which 2, 3, 4, 6 resonators are used in the domain containing a single point source solely. In order to have a more generic description of the field, the moving point source and the complete resonator system are used in this case. Each system is placed in the vicinity of the source axis, at $\Delta r = 1.5m$. As shown in Figure 8.7, the more resonators are used in the system, the higher noise reduction level can be achieved. The blue line indicates the baseline spectrum with the

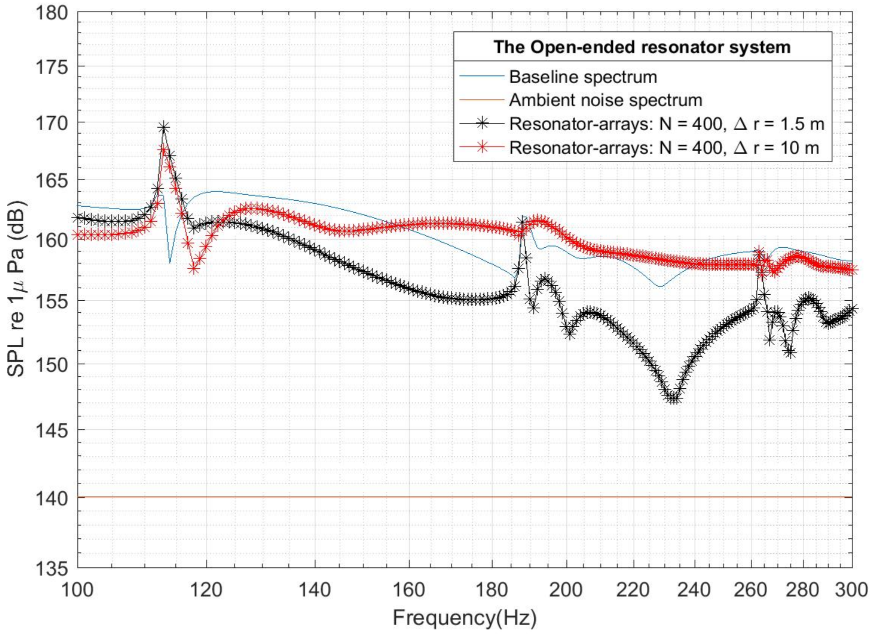

Figure 8.6: Different positions of the resonator system: average sound pressure level (dB re $1 \mu Pa$) at $r = 25 meter, \phi = 180°$, along 10-meter water depth.

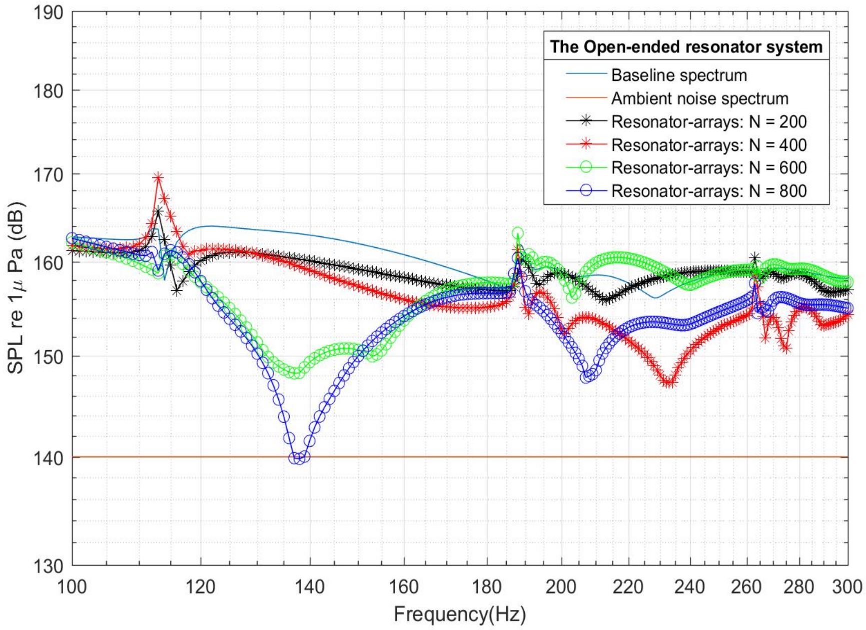

Figure 8.7: Different numbers of the resonators applied in the system: average sound pressure level (dB re $1 \mu Pa$) at $r = 25 meter, \phi = 180°$, along 10-meter water depth.

moving point sources solely. The orange line represents the ambient noise spectrum without both point sources and resonator system. The blue line with circles shows that a resonator-system containing 800 resonators can achieve a noise reduction level more than 20 dB around 140 Hz.

Based on the discussion above, we can conclude that the one of the primary parameters that dominating the performance of noise reduction is the void fraction of the resonator-system, in other words, the position of the system and the number of the resonators used in the system. The void fraction for any resonator-based noise mitigation system can be expressed as:

$$\beta = \frac{\sum_{i=1}^{M} V_{air,i} \cdot N_{resonator,i}}{V_{system}} \tag{8.3}$$

in which V_{system} indicates the volume of the field which enclosed by the resonator curtain, $V_{air,i}$ represents the volume of the air for the resonator with index i, $N_{resonator}$ is the number of each type of the resonator with index i. The results from this study show that the resonator-system placed in the vicinity of the pile is preferable. The increase of the number of the resonator element can improve the acoustic performance of the resonator-system.

Chapter 9

Conclusion and Recommendations

9.1 Conclusion

This thesis aims to answer the research question, "how to mitigate the noise from pile driving by using a resonator-based noise mitigation system". The reasoning of the research question was discussed in the introduction (Chapter 1). To have a better understanding of the physical mechanism of different existing noise mitigation techniques, the advantages and disadvantages of various systems is discussed (Chapter 2). Special attention to open-ended resonators was given due to its promising acoustic behaviour. The comparison to Hydro-Sound Damper was investigated by finite element model in COMSOL Multiphysics. The frequency response function also was derived based on the numerical results, which is used to describe the acoustic behaviour of resonators in a more generic basis (Chapter 3). Chapter 4 presents Qiu resonator, which is proposed by the author. The design is implemented in COMSOL Multiphysics, and a parametric study was made to find the dominating parameters. A three-dimensional acoustically coupled noise reduction prediction model was developed by the author. This model requires the accurate description of the noise source, the acoustic behaviour of the resonators and the waveguide. The pressure field for the point source and the line source has been discussed in Chapter 5. The governing equations and the corresponding matrix equations are formulated in Chapter 6. Several parametric study cases are shown in Chapter 7. Several applications of the model are discussed in Chapter 8. In this chapter, the important conclusions and recommendations for both offshore industry and future development of the theoretical model are discussed.

Based on the study of the existing noise mitigation techniques in Chapter 2, it shows that the resonator-based system is a promising way to mitigate the underwater noise. The resonator-based noise mitigation systems have the following strengths:

- Based on the offshore demonstration tests, the technique could reach relatively high noise reduction level;
- The resonator-based system can be tuned to certain target frequencies. Therefore, this technique especially has better performance at low-frequency underwater noise;

- The system usually consists of arrays of resonators, which does not require a complicated method. Therefore, the deployment system can be only simple and convenient;
- The resonator-based system is flexible enough to work with different sized piles and also can work together with other noise mitigation systems to provide multi-barriers;
- It's convenient to modify the structure of the resonators to block various noise paths, so it also provides a promising option to mitigate the Scholte waves along the seabed interface;

The existing resonator-based noise mitigation techniques also have some disadvantages, which are worth mentioning (in the case of the HSD system and the open-ended resonator system) :

- The present resonator-based systems all lack commercial experience;
- The study on underwater resonators used for noise reduction is rather limited. The noise reduction level has not been predicted by any theoretical model or numerical model yet;

Therefore, this study aims to build a three-dimensional noise reduction prediction model for the application of a resonator-based noise mitigation system.

Chapter 3 focus on the theory of underwater Helmholtz resonator (in the case of the open-ended resonator) and verify it by the finite element model in COMSOL Multiphysics. The numerical model for hydro-sound damper was also built in order to compare with the acoustic behaviour of the open-ended resonator and is verified through the well-known theoretical model, Church model and Commander and Prosperetti model. The results from this section show that the open-ended resonator ideally behaves as a single-degree-of-freedom system, the theoretical model has good agreement with the numerical model.

The frequency response function was also derived in chapter 3. The section shows that the ideal mass in a mass-spring-dashpot system is close to the real weight of water column, which can also be seen as acoustic mass. The fitting between the response from the resonator with the response of the analogous single-degree-of-freedom mass-spring-dashpot system could provide us the parameters correspondingly. Different coefficients can be modified by changing the dimensions of the resonator or adding porous material with various flow resistivities.

Based on the study on the existing noise mitigation systems, a new resonator was developed in Chapter 4, named *Qiu* resonator. By using a layer of hyperelastic membrane to encapsulate the air in the resonator, the deployment system for this new resonator can be simple and convenient. It shows that the water depth could increase the radius of the inner elastic ball for up to 0.8 cm. However, the air density could increase 5 times as much as the initial one. The opening radius could influence the noise reduction level by changing the contact area with the incoming waves. While the reason for the change of resonance frequency due to the opening radius still needs further investigation. The thickness of membrane also influences the resonance frequency. By using a thicker membrane, the resonance frequency can shift to a higher range. Because the stiffness of membrane can physically determine the stiffness of the analogous SDoF system. Thus, as shown in $\omega = \sqrt{k/m}$, by increasing the stiffness coefficient, the resonance frequency increases correspondingly.

To improve the existing resonator-based noise mitigation systems, a three-dimensional noise reduction prediction model is developed. The derivation of the governing equation and the construction of Green's function are discussed in Chapter 5 and Chapter 6. The pressure field can be decomposed into the contribution from a point source and the contribution from the resonator arrays. The pressure waves at the site of the resonator are determined by both the noise source and the other resonators. Therefore, this is an acoustically coupled problem. The first step is to obtain the pressure at the site of each resonantor by solving the matrix equations. By using the Boundary Element Method, the formulation of the pressure field can be solved by the boundary integral equation consisting of the surface integral of the opening surface of the resonator and the volume integral of the point source. The advantage of this method is that the Green's function we derive could inherently satisfy the wave equation, boundary conditions and the radiation conditions, except the conditions on the opening-end of the resonators. It is worth to mention that the scattering effect is not included in this model. Therefore, the other surface of resonator is not considered in the integral. In the present model, we focus on the description of the acoustic behaviour of the resonator.

Chapter 7 deals with the investigation of the dominating factors, which could influence the acoustic performance of the resonator-based noise mitigation system. A single resonator in the waveguide is validated by using a finite element model in COMSOL Multiphysics. The influence of the internal resistance, the number of the resonator and the combination of the resonators with different resonance frequencies is investigated. The result from this study shows that choosing a resonator with proper internal resistance could improve the efficiency of the noise reduction. The increase in the number of resonators in the system indeed could intensify the noise reduction level. The destructive interference is also found in this study. It shows that although the mitigation of the sound takes place at our target frequency, the resonator could shift part of the energy to higher frequency. This can be mitigated by using resonators at the various resonance frequency. By doing this, a wider band of noise reduction can be achieved and the destructive interference can be thoroughly mitigated.

Chapter 8 presents several modal applications. The damping coefficient is investigated further in order to find the optimal value of the individual resonator. However, to achieve better acoustic performance, other parameters still need to be further investigated and determined. A field simulation is conducted for a upcoming lake test, which could estimate the proper number of resonators needed to achieve a certain level of noise reduction. The sound radiation from pile driving is represented by an array of phased point sources along the pile axis. The Mach cone formed in this model shows a qualitative agreement with the results from FE simulation or WI simulation in the past research. Based on the better description of the noise source, the noise reduction levels with the use of the complete resonator system with different positions and configurations can be predicted.

Besides, the present model potentially could achieve the following targets:

- Estimation of the required amount of resonators in order to achieve certain level of noise reduction;
- Evaluate the "optimal" properties for an underwater resonator;
- Determine the "optimal" combination of different target frequencies in order to improve the efficiency of the system;

- The model can be compatible with the different resonator-based systems;

9.2 Recommandetions

9.2.1 Recommandetions for the development of noise mitigation system

Some recommendations for the future development of noise mitigation systems are listed below:

1. The proper use of porous material could improve the acoustic performance of the resonators;
2. Combine resonators with various resonant frequencies, which could potentially achieve a broad band noise reduction;
3. Combine of two noise mitigation systems with different working mechanism to provide multi-barriers, i.e. using air bubble curtain in the vicinity of the pile and resonator-based noise mitigation system at relatively large distance;
4. By using resonators along the seabed interface to mitigate the Scholte waves, this also needs further study on the acoustic behaviour of resonators on the seabed surface environment;

9.2.2 Recommandetions for the improvement of the current model

Some recommendations for the further improvement of the current models are listed below:

1. A more realistic model can be developed by including:
   - The seabed can be modelled as a dissipative impedance boundary;
   - The noise source could use a downward moving point source to model the process of pile driving and the propagation of the sound waves;
   - Incorporate the scattering, multiple reflections and refraction effect into the model;
2. Different piling methods to control the noise at the source can be incorporated into the model in the future.

Appendix A

Sound attenuation in seawater

The sound attenuation can be attributed to many effects, such as absorption and scattering [18]. A part of energy can be absorbed due to viscous loss and being transformed into heat when the sound propagate in seawater. Moreover, the inhomogeneities in seawater can result in a decay of sound intensity by scattering effect. The different dominant process of sound attenuation in seawater is shown in Figure A.1 [22]. The frequency dependence of attenuation is discussed in many previous study [22, 23, 24].

The expression to describe this frequency dependence of attenuation can be formed as[22]:

$$\alpha' \approx 3.3 \times 10^{-3} + \frac{0.11f^2}{1+f^2} + \frac{44f^2}{4100+f^2} + 3.0 \times 10^{-4} f^2 (dB/km) \tag{A.1}$$

We can read out from the above expression that the attenuation can increase with frequency. Thus, low-frequency sound is relatively small in seawater[11].

Attenuation can be included by adding an imaginary part to the sound speed so that:

$$c = c_r - ic_i \tag{A.2}$$

The imaginary part of the sound speed is related to the attenuation α in nepers/m as:

$$c_i \simeq \frac{\alpha}{\omega} c_r^2 \tag{A.3}$$

From the defination of the attenuation α' in units dB/km, we have the ratio of the intensity between two points 1 km apart given as:

$$\begin{aligned} \alpha' &= -10log\frac{I(x+1km)}{x} = -20log\frac{\exp(-\alpha(x+1km))}{\exp(-\alpha x)} \\ &= 1000 \times 20loge \times \alpha = 8686\alpha \end{aligned} \tag{A.4}$$

Then substituting the above equation into the Eq. (A.2) and Eq. (A.3), this gives us:

$$c = c_r - i\frac{\alpha}{\omega}c_r^2 = c_r - i\frac{\alpha'}{8686\omega}c_r^2 \tag{A.5}$$

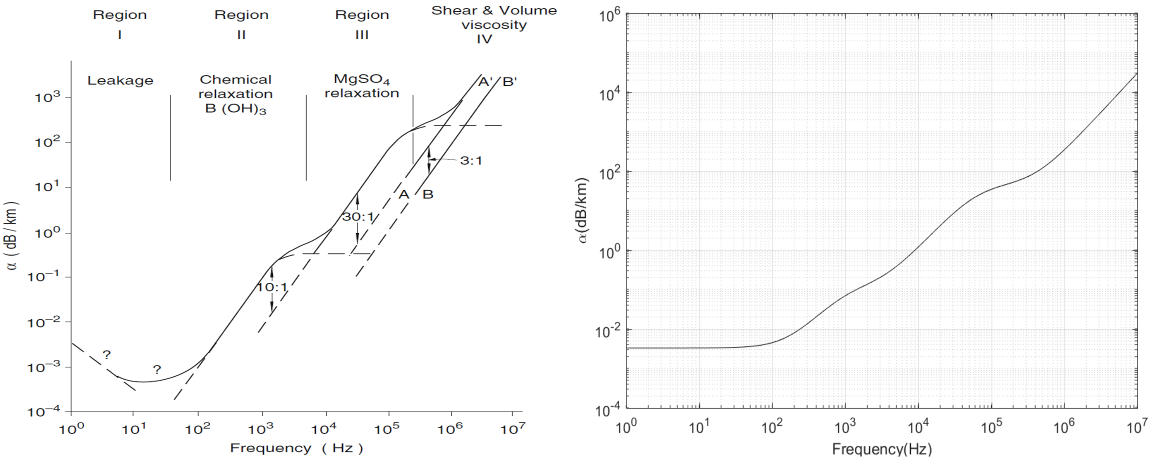

(a) **(b)**

Figure A.1: Sound attenuation in seawater: (a) different dominat process; (b) simplified expression for frequency dependent attenuation

Hence, the wavenumber become a complex number as [25]:

$$k = \frac{\omega}{c_r - i\frac{\alpha}{\omega}c_r^2} = k_0 + ik_1 \tag{A.6}$$

where k_0 represents the real part of the wavenumber and k_1 represents the imaginary part of the wavenumber. The introduction of the complex wavenumber will affect the radial wavenumber as well, which could result in a decrease along the radial direction for the solution of the Bessel's function. This physically means that the sound wave could attenuate over long-range.

Bibliography

[1] P. G. Reinhall and P. H. Dahl, "Underwater mach wave radiation from impact pile driving theory and observation," *The Journal of the Acoustical Society of America*, vol. 130, no. 3, pp. 1209–16, 2011.

[2] A. Tsouvalas and A. V. Metrikine, "A three-dimensional vibroacoustic model for the prediction of underwater noise from offshore pile driving," *Journal of Sound and Vibration*, vol. 333, no. 8, pp. 2283–2311, 2014.

[3] A. Tsouvalas, *Underwater noise generated by offshore pile driving.* Thesis, Delft University of Technology, 2015.

[4] OSPAR, "Ospar inventory of measures to mitigate the emission and environmental impact of underwater noise," tech. rep., OSPAR Commission, 2014. Technical report.

[5] K. Elmer, J. Gattermann, C. Kuhn, B. Bruns, and J. Stahlmann, "Mitigation of underwater piling noise using balloons and foam elements as hydro sound dampers," *Proceedings of the 11th European Conference on Underwater Acoustics*, vol. 2012-July, pp. 1142–1149, 2012.

[6] K. M. Lee, A. R. McNeese, P. S. Wilson, and M. S. Wochner, "Using arrays of air-filled resonators to attenuate low frequency underwater sound," *The Journal of the Acoustical Society of America*, vol. 136, no. 4, p. 2207, 2014.

[7] A. Technologies, "Adbm demonstration at butendiek offshore wind farm with ballast nedam," tech. rep., AdBm Technologies, 2014. AdBm Butendiek Demonstration Report.

[8] M. Alster, "Improved calculation of resonant frequencies of helmholtz resonators," *Journal of Sound and Vibration*, vol. 24, no. 1, pp. 63–85, 1972.

[9] H. Bailey, B. Senior, D. Simmons, J. Rusin, G. Picken, and P. M. Thompson, "Assessing underwater noise levels during pile-driving at an offshore windfarm and its potential effects on marine mammals," *Marine Pollution Bulletin*, vol. 60, no. 6, pp. 888–897, 2010.

[10] S. T. Viada, R. M. Hammer, R. Racca, D. Hannay, and M. J. Thompson, "Review of potential impacts to sea turtles from underwater explosive removal of offshore structures," *Environmental Impact Assessment Review*, vol. 28, no. 4, pp. 267–285, 2008.

[11] A. Tsouvalas and A. V. Metrikine, "Noise reduction by the application of an air-bubble curtain in offshore pile driving," *Journal of Sound and Vibration*, vol. 371, pp. 150–170, 2016.

[12] K. W. Commander and A. Prosperetti, "Linear pressure waves in bubbly liquids: Comparison between theory and experiments," *The Journal of the Acoustical Society of America*, vol. 85, no. 2, pp. 732–746, 1989.

[13] C. C. Church, "The effects of an elastic solid surface layer on the radial pulsations of gas bubbles," *The Journal of the Acoustical Society of America*, vol. 97, no. 3, pp. 1510–1521, 1995.

[14] K. H. Elmer, J. Gattermann, C. Kuhn, and B. Bruns, "Mitigation of underwater piling noise by air filled balloons and pe-foam elements as hydro sound dampers," *The Journal of the Acoustical Society of America*, vol. 132, no. 3, p. 2056, 2012.

[15] A. Tsouvalas and A. V. Metrikine, "A semi-analytical model for the prediction of underwater noise from offshore pile driving," *Journal of Sound and Vibration*, vol. 332, no. 13, pp. 3232–3257, 2013.

[16] A. Tsouvalas and A. V. Metrikine, "Wave radiation from vibratory and impact pile driving in a layered acousto-elastic medium," *Proceedings of the 9th International Conference on Structural Dynamic , EURODYN*, vol. 2014-January, pp. 3137–3144, 2014.

[17] A. Hirschberg and S. Rienstra, *An Introduction to Acoustics.* Eindhoven University of Technology, 2015.

[18] F. Jensen, W. Kuperman, M. Porter, and H. Schmidt, *Computational Ocean Acoustics.* Springer New York, 2011.

[19] F. W. J. Olver, *NIST handbook of mathematical functions.* [S.l.] : Cambridge :: NIST, National Institute of Standards and Technology, U.S. Department of Commerce; Cambridge University Press, 2010.

[20] D. C. Ricks, *Elastodynamic modeling of fluid-loaded cylindrical shells with multiple layers and internal attachments.* Thesis, 1994.

[21] T. Loppert and S. Lippert, "Modeling of pile driving noise by means of wavenumber integration," *Acoustic Australia*, vol. 40, no. 3, pp. 178–182, 2012.

[22] R. J. Urick, *Sound propagation in the sea.* Los Altos, Calif. :: Peninsula, [rev. ed.]. ed., 1982.

[23] F. H. Fisher and V. P. Simmons, "Sound absorption in sea water," *The Journal of the Acoustical Society of America*, vol. 62, no. 3, pp. 558–564, 1977.

[24] W. H. Thorp, "Analytic description of the low-frequency attenuation coefficient," *The Journal of the Acoustical Society of America*, vol. 42, no. 1, p. 270, 1967.

[25] J. Eskenazi, *A computer model for sound propagation around conical seamounts*. Thesis, Massachusetts Institute of Technology. Department of Ocean, Engineering, 2001.

Glossary

List of Acronyms

ABC	Air Bubble Curtain
BBC	Big Bubble Curtain
NMS	Noise Mitigation Screen
HSD	Hydro-Sound Damper
1DOFS	One Degree of Freedom System
OWF	Offshore Wind Farm

Index